IEEE Access
Multidisciplinary ⋮ Rapid Review ⋮ Open Access Journal

Received 5 March 2024, accepted 26 March 2024, date of publication 28 March 2024, date of current version 5 April 2024.

Digital Object Identifier 10.1109/ACCESS.2024.3382939

TOPICAL REVIEW

Advances in Electrical Impedance Tomography Inverse Problem Solution Methods: From Traditional Regularization to Deep Learning

CHRISTOS DIMAS, (Member, IEEE), VASSILIS ALIMISIS, (Student Member, IEEE), NIKOLAOS UZUNOGLU, (Fellow, IEEE), AND PAUL P. SOTIRIADIS, (Fellow, IEEE)
Department of Electrical and Computer Engineering, National Technical University of Athens, 157 72 Zografou, Greece

Corresponding author: Christos Dimas (chdim@central.ntua.gr)

The publication of the article in OA mode was financially supported by the Hellenic Academic Libraries Link (HEAL–Link).

ABSTRACT Electrical Impedance Tomography (EIT) has emerged as a valuable medical imaging modality, which visualizes the conductivity distribution of a subject by performing multi-electrode impedance measurements. EIT finds applications in monitoring lung and cardiac function, brain imaging and the detection of malignant tissues. Its mobility, outstanding temporal resolution and the absence of ionizing radiation make it particularly suitable for repetitive real-time monitoring and diagnostics, especially in radiation-sensitive populations, such as neonates. This paper presents a methodological review of EIT image reconstruction approaches spanning from traditional linear regularization and back-projection to more recent techniques, including deep learning, sparse Bayesian learning and non-linear shape-driven reconstruction. Linear and non-linear reconstruction approaches are distinguished, as well as time, frequency difference and absolute reconstruction ones. The exposition includes a concise elaboration of the methodologies' mathematical foundations and algorithmic deployment, with particular attention to recent advancements. For each approach, an assessment of its merits and drawbacks is given, providing implementation considerations, imaging performance and relevant applications.

INDEX TERMS Electrical impedance tomography, inverse problem, regularization, Ill-posedness, Bayesianism, deep learning.

I. INTRODUCTION

Electrical Impedance Tomography (EIT) performs imaging of the conductivity distribution within a two-dimensional slice or three-dimensional volume of a subject by injecting a periodic current signal through an array of surface-attached electrodes [1]. During this process, the differential electrode potentials are measured and processed to obtain a measurement vector, which serves as the input data for image reconstruction. EIT appears compelling advantages over X-Ray, CT and MRI, since it is characterized by lack of ionizing radiation, mobility, relatively low hardware equipment cost and high temporal resolution. The latter provides EIT with the potential for use in real-time medical applications, such as lung and cardiac function monitoring and brain imaging, to observe vital signs and conditions such as tidal volume [2], acute respiratory distress syndrome (ARDS) [3] and brain ischemic hemorrhage [4], [5]. Additionally, EIT has proven useful for malignant tissues' detection and classification. Some representative examples can be found in prostate imaging and breast tomography [6], [7], [8]. Furthermore, EIT finds space in a variety of other medical or industrial applications, such as gastric-emptying monitoring [9], bladder monitoring [10] and non-destructive evaluation [11].

However, EIT's poor spatial resolution as well as sensitivity to noise and modeling errors remain two major drawbacks that hinder its widespread adoption in the field

The associate editor coordinating the review of this manuscript and approving it for publication was Carmelo Militello.

of medical diagnostics. In contrast to CT and MRI, where ionizing X-rays and strong EM fields respectively propagate as waves within the subject under test (SUT), in EIT, the current diffuses between the stimulating electrode pairs. This results in a voltage distribution that adheres to a Laplace equation. In qualitative terms, this means reduced sensitivity of the boundary (electrode) potentials to any contuctivity perturbations, especially when the latter take effect far from the current stimulation electrodes. The above *soft field* effect leads to an ill-conditioned inverse problem of recovering the conductivity distribution from boundary potential data.

Since the introduction of the first experimental EIT system in 1978 [12], the corresponding inverse problem has remained an active research field and many approaches have been proposed and evaluated to address it. The earlier EIT systems used the Sheffield (adjacent) current stimulation protocol to inject the current through a rotating single pair of neighboring electrodes, while image reconstruction was achieved using the linear back-projection algorithm [13]. During the early 90s, inversion techniques that incorporate prior knowledge regarding the conductivity distribution's behavior, based on Tikhonov regularization (l^2-norm prior) [14], were introduced and widely adopted [15], [16], [17], [18]. Initially, such techniques were applied as single-step (direct) conductivity estimations, assuming minor conductivity changes and a linear relationship between the conductivity distribution and the boundary electrode voltages. With the evolution of computer hardware, iterative Gauss-Newton-based approaches and generalized Tikhonov regularization [17], [19], [20] that could tackle the non-linear nature of the inverse problem began to gain popularity. Three-dimensional imaging [21], [22] and the l^1-norm prior total variation regularization [23], [24], [25], which assumes steep spatial changes in conductivity, were also adopted in various EIT applications.

However, the linear methods still remained popular in time-difference EIT imaging, where conductivity changes between different states (e.g. inspiration and expiration ends during breathing) are reconstructed with sufficient temporal resolution and can be assumed small enough to approximate a linear behavior. At the same time, the D-Bar reconstruction method, based on a non-linear inverse scattering Fourier transform was developed along with the trigonometrical current injection protocol [26], [27], [28], [29]. The D-Bar applies low-pass filtering which serves as regularization to smoothen anomalies in conductivity changes, while the trigonometric pattern was proven to be very efficient for providing valuable information for the conductivity distribution within a smaller number of measurements [30]. Finally, the Graz consensus reconstruction algorithm for EIT (GREIT) was developed in 2009 as an alternative single-step approach that utilizes a figure-of-merit (FoM) framework for simultaneous optimization of both parameters and performance [31].

From the mid-2010s, more advanced, at most non-linear, EIT inverse problem approaches were proposed to enhance the produced images. These included the alternating direction method of multiplier (ADMM) [32] and the Bregman-distance [33], [34], [35] techniques that were incorporated in total variation regularization and hybrid (l^2-norm combined with l^1-norm) regularization. Although the techniques mentioned above improved the spatial resolution of EIT images, their applicability to real medical imaging is still limited by a few important obstacles. The large number of hyperparameters, combined with the lack of systematic methods for their proper selection, make the optimization process difficult and time-consuming. Moreover, the requirement of numerical re-computations of electric fields significantly slows down the reconstruction process, adding to the challenges. Addressing them is crucial for the practical application of EIT in medical imaging, especially in real-time monitoring scenarios.

In the late 2010s, a novel category of EIT reconstruction algorithms emerged, referred to as shape-driven methods [36], [37], [38]. These algorithms offer an individual approach to tackle the ill-posed nature of the inverse problem by focusing on approximating the exact shapes of conductivity inclusions rather than estimating the subject's conductivity distribution. To achieve this, dimensionality reduction techniques are used to deal with complex geometries commonly encountered in medical applications [37], [39]. While these methods are considered effective, their implementation still requires careful consideration of hyperparameters and conductivities' initial values and convergence can be slow due to the considerable number of parameters involved. Additionally, to the shape-driven methods, meta-heuristic population-based approaches were also applied in EIT, such as the genetic algorithm [40], [41] and the particle swarm optimization (PSO) [42].

To address the issue of proper hyperparameter selection as well as the robustness of EIT images to noise, sparse Bayesian learning (SBL) has been recently applied in EIT [43], [44], [45], [46]. SBL is an unsupervised machine learning technique, where a prior probability distribution of the subject's conductivity map and a likelihood function describing the probability of obtaining the measured voltage data given the conductivity map are defined. Through a self-trained hyperparameter optimization process, the above probability distributions are used to estimate the posterior probability distribution of the conductivity map, which is assumed to be sparse. SBL approaches have demonstrated superior spatial performance at the cost of extremely high complexity, especially in fine discretization domains and 3D structures [44].

Supervised neural networks (NNs) have been widely used in recent EIT image reconstruction research, leveraging their ability to handle the problem's non-linearity and ill-conditioning. By training NNs on large sets of EIT data, they can learn the underlying relationship between information regarding the boundary voltage measurements, the stimulation pattern, as well as the electrode-subject geometry and the conductivity distribution. The first popular

NN-based learning applications in EIT employed simple artificial NNs (ANNs) that were trained to predict the conductivity map directly through the measurement data [47], [48], [49], [50], [51], [52], [53], [54], [55], [56]. However, this approach suffers from training divergence issues [57] and necessitates extensive datasets, limiting its ability to generalize to different setups. To improve these issues, as well as to enhance existing imaging methods performance, deep learning (DL) schemes were adopted. In 2018, the deep-D-Bar was introduced as a U-net based image post-processing technique to significantly improve the quality of D-Bar EIT reconstructed images in terms of both accuracy and robustness [58]. A deep-D-Bar modification is the domain-independent Betrami-net, exploited in absolute EIT imaging [59]. Furthermore, iterative model-based techniques such as the dominant current deep learning scheme (DC-DLS) [60], induced-current learning method (ICLM) [61], NN approach for multiphase-flow shape reconstruction [62] and a multiple measurement vector based NN (MMV-net) [63] for multifrequency EIT (Mf-EIT), were used to combine the EIT inverse problem's physical background with the capabilities of DL. More recently, graph NNs were introduced in the field of inverse scattering problems [64], including cell culture imaging mf-EIT [63], to bridge the divide between the finite-element nature of the EIT model structures and the necessity of pixelized images for CNNs. Furthermore, a novel category of DL schemes applied in EIT is based on the deep image prior [65], [66], where the images are produced through the internal NN architecture without the usage of training data.

The brief historical overview presented above highlights the significant developments that have taken place in addressing the EIT inverse problem. A number of approaches have been developed, many of which remain popular in medical applications today. The literature contains several reviews that discuss past progress in traditional EIT imaging techniques [67], [68], [69] and those based on ML [56], [70], [71], [72], [73], [74], [75]. This paper presents a unified and comprehensive overview of the inverse problem solution approaches for EIT, spanning from conventional linear to the latest DL trends. Its objective is to offer a clear and intuitive explanation of the essential concepts underlying the various approaches, highlighting their evolution and continuity, in order to facilitate understanding and bridge the gap between traditional and contemporary ones. Emphasis is given to the latest advancements and their associated applications. In addition, to provide a holistic understanding of EIT imaging, a brief explanatory review of the current stimulation patterns, the absolute and difference EIT measurement methods and the forward problem is also included.

In summary, this paper focuses on the following aspects:

- The paper provides an extensive overview of image reconstruction methods used in EIT. It spans from conventional regularization techniques to cutting-edge DL schemes.
- The approaches are systematically categorized based on their mathematical and theoretical foundations.
- The core principles within each category are explained in detail, highlighting their respective advantages and challenges.
- Recent advancements, based on the aforementioned principles are critically examined, highlighting their specific contributions in addressing the identified challenges and capturing the state-of-the-art methodologies.
- The paper engages in comparative discussions both within and between different categories of approaches, focusing on the evolutionary aspects of the methodologies.
- The presented approaches are selected and structured to comprehensively address the domain of EIT image reconstruction research. Their inclusion is based on their widespread applicability, popularity and their significant contributions to current imaging trends.

The rest of this paper is organized as follows: In Section II, the basic principle of the EIT problem is explained, including static and difference EIT, along with the forward problem formulation. Section III reviews the conventional inverse problem approaches, encompassing generalized Tikhonov regularization, total variation, GREIT, D-Bar and subspace optimization. Additionally, Section IV elucidates and revises the shape EIT reconstruction techniques. In Section V, the application of population-based algorithms for EIT image reconstruction is presented, while Section VI provides a brief description of the concept and application of the sparse Bayesian learning method. Moreover, in Section VII, both earlier and recent DL approaches applied in EIT are presented, compared and discussed. An overall discussion regarding the feasibility and limitations of the reconstruction approaches on contemporary application trends is written in Section VIII. Finally, Section IX concludes this paper.

II. EIT PRINCIPLE

EIT is a current diffusion process, where one or more electrode pairs, attached to the subject's surface, are utilized to inject a single or multi-frequency current into the subject's volume. This stimulation results in an electric field, in which the potential obeys the Laplace equation:

$$\nabla\big(\sigma(\boldsymbol{r})\nabla u(\boldsymbol{r})\big) = 0, \quad \boldsymbol{r} \in \Omega \tag{1}$$

where Ω denotes the SUT 2D or 3D domain, $u(\boldsymbol{r})$ is the potential and $\sigma(\boldsymbol{r})$ is the relative conductivity distribution. Assuming the popular complete electrode model (CEM), where both electrode dimensions, contact impedances and shunting effect are considered, the corresponding boundary conditions are described as follows:

$$u(\boldsymbol{r}) + z_\ell \sigma(\boldsymbol{r}) \frac{\partial u(\boldsymbol{r})}{\partial \boldsymbol{n}} = U_\ell, \quad \boldsymbol{r} \in e_\ell, \ \ell = 1, \ldots, N \tag{2}$$

$$\int_{e_\ell} \sigma(\boldsymbol{r}) \frac{\partial u(\boldsymbol{r})}{\partial \boldsymbol{n}} dS = I_\ell, \quad \ell = 1, \ldots, N \tag{3}$$

$$\sigma(\boldsymbol{r})\frac{\partial u(\boldsymbol{r})}{\partial \boldsymbol{n}} = 0, \quad \boldsymbol{r} \in \partial\Omega \setminus \bigcup_{\ell=1}^{N} e_\ell. \tag{4}$$

In the expressions above, z_ℓ denotes the ℓ-th electrode's contact impedance, U_ℓ the ℓ-th electrode's potential, e_ℓ the ℓ-th electrode's domain, I_ℓ the current amplitude sourced or sunk from the ℓ-th electrode and $\boldsymbol{n}$ the unity outward-pointing vector. Other EIT electrode model definitions include the point electrode model (PEM) [76], the continuum or gap electrode model, the discretization effect and the perfectly conducting (zero-impedance) models [77].

The EIT reconstruction problem entails the estimation of the conductivity distribution $\sigma(\boldsymbol{r})$ based on the domain's geometry, the boundary electrodes' voltages U_ℓ and the electrodes' currents I_ℓ (inverse problem). However, an essential step to solve the inverse problem involves predicting the potential distribution $u(\boldsymbol{r})$, given an initial (usually homogeneous) guess of $\sigma(\boldsymbol{r})$ (forward problem). The EIT forward problem can be solved through (1)-(4), typically using the finite element method (FEM) (see also subsection II-E). Other numerical methods employed for estimating the potential distribution include the method-of-moments (MoM) [78], [79] and the boundary element method (BEM) [80]. These methods are frequently combined with the FEM to obtain more accurate solutions, particularly in cases with complex geometries that exhibit sharp edges.

A. CURRENT/VOLTAGE PATTERNS

To obtain an EIT voltage measurement set, a predefined current injection pattern (protocol) is applied to a sequence of electrode pairs while voltage measurements are recorded from the remaining electrodes in the setup. The process is repeated for a specific number of current electrode pairs, resulting in a large set of tetrapolar impedance measurements. Tetrapolar measurements are preferred over bipolar ones, as the latter often introduce significant measurement errors due to the electrode contact impedances and the shunt effect [81], [82], [83], [84], [85]. The EIT current stimulation protocols can be classified into two main categories: A) The pairwise patterns and B) The trigonometrical "optimal" current patterns. In pairwise patterns, the current is usually injected from a single electrode pair at a time, while in trigonometric patterns, all the electrodes are stimulated simultaneously [86].

The most commonly used current stimulation pattern is the pairwise adjacent (or Sheffield) one, where the current is injected through two neighboring electrodes, while the voltages are measured between the rest of the neighboring electrode pairs [87]. The adjacent protocol remains popular in medical applications since it can be applied using less-complex hardware EIT systems, can better tolerate modeling errors and provides the largest number of independent measurements ($N \cdot (N-3)/2$ for an N-electrode system) [88]. However, when the adjacent current stimulation is applied, most of the voltage measurements have significantly low sensitivity to conductivity perturbations that are far from the current electrodes [87], [89], [90]. This reduced sensitivity exacerbates the soft-field effect and worsens the conditioning of the reconstruction problem. In general, the pairwise current patterns are also called skip-m, where m is the number of electrodes between the current source and the current sink electrode [91]. For example, the adjacent pattern is also considered as skip-0. The skip-n notation is also used for the voltage measurement patterns, where n is the number of electrodes between the differential measurement electrodes. Voltage measurement patterns with low or zero skip (such as adjacent) require less complex hardware, but they may suffer from lower signal-to-noise ratio (SNR) due to their low voltage amplitudes. On the other hand, high skip voltage patterns may have higher SNR levels, but they may lead to mirroring artifacts in the reconstructed images, in addition to requiring more complex measurement systems. Fig. 1 presents an explanatory schematic of the pairwise current and voltage patterns.

The trigonometric current patterns apply current to all the electrodes simultaneously to create a more evenly distributed current density and minimize the soft field effect [30], [87], [89]. Such patterns also provide a high number of independent measurements and are usually used along with the D-Bar reconstruction algorithm (see subsection III-H). Nevertheless, they require multiple well-matched current sources leading to high hardware complexity. In any case, the choice of the current and voltage stimulation patterns depends on the specific application and the trade-off between hardware complexity, SNR and image quality.

B. ABSOLUTE EIT

In absolute (static) EIT (a-EIT), the image is reconstructed using a single measurement vector of the following form:

$$\boldsymbol{V} = [V^1\ V^2\ \dots\ V^{Nh}]^T \in \mathbb{R}^{Nh\times 1} \tag{5}$$

where h is the number of differential voltage measurements collected per current electrode stimulation pair. For the current skip-m, voltage skip-n (pairwise) patterns it is $h = N-3$ when $m = n$, or $h = N-4$ otherwise. At the same time, we define the corresponding computed boundary voltages that are computed through the forward problem:

$$\boldsymbol{U} = [U^1\ U^2\ \dots\ U^{Nh}]^T \in \mathbb{R}^{Nh\times 1} \tag{6}$$

The purpose is to obtain an estimation of the SUT conductivity distribution by minimizing the norm between $\boldsymbol{V}$ and $\boldsymbol{U}$ (fidelity term). Although a-EIT is expected to derive real conductivity values (in (S/m)), in practice, it is very sensitive to modeling errors, such as inaccuracies in geometry and the electrodes' contact impedances, often resulting in misleading images. Therefore, it is hardly used in medical applications, especially if motion artifacts are present.

C. TIME-DIFFERENCE EIT

In time-difference EIT (td-EIT), the measurement vectors obtained from two or more consecutive states are utilized to

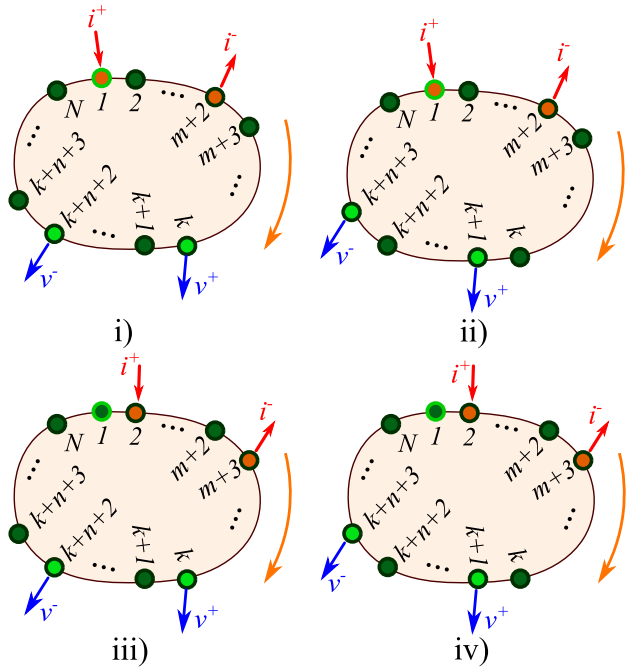

FIGURE 1. Brief schematic of a current skip-m, voltage skip-n pairwise pattern. i) Current stimulation at the 1st and the $(m+2)$-th electrodes, voltage measurement between the k-th and $(k+n+2)$-th electrodes. ii) Same current stimulation electrodes as in i), voltage measurement between the $(k+1)$-th and $(k+n+3)$-th electrodes. iii) Current stimulation at the 2nd and the $(m+3)$-th electrodes, voltage measurement between the k-th and $(k+n+2)$-th electrodes. iv) Same current stimulation electrodes as in iii), voltage measurement between the $(k+1)$-th and $(k+n+3)$-th electrodes.

reconstruct an image that demonstrates changes in conductivity distribution over time. By subtracting the measurement frames $\boldsymbol{V}^{(t_1)} \in \mathbb{R}^{Nh\times 1}$ and $\boldsymbol{V}^{(t_2)} \in \mathbb{R}^{Nh\times 1}$ obtained from two consecutive time points t_1 and t_2 ($t_2 > t_1$), td-EIT provides a differential measurement vector $\boldsymbol{\delta V} = \boldsymbol{V}^{(t_2)} - \boldsymbol{V}^{(t_1)}$ that enhances the sensitivity of the EIT system to conductivity changes. Unlike a-EIT, td-EIT can suppress a large percentage of modeling errors and tolerate minor inaccuracies in the model. Therefore, td-EIT has proven particularly useful in applications such as lung, cardiac, or gastric monitoring, where changes in conductivity are important for estimating critical biomarkers like tidal volume. However, td-EIT is not effective in applications where the conductivity distribution remains temporally constant, such as tumor detection, as it requires a baseline (or reference frame) that is often assumed to be homogeneous [92], [93]. Additionally, td-EIT assumes that no motion or changes in the shape or conductivity of the subject under test (SUT) occur during each particular measurement to acquire a frame. Hence, it necessitates the use of a relatively fast EIT hardware system with a high frame rate that matches the application requirements.

D. FREQUENCY-DIFFERENCE EIT

Considering the case where the current excitation is sinusoidal of frequency f, the measured voltage is a function of f. In frequency-difference EIT (fd-EIT), two sets of measurements are obtained for two different excitation current frequencies [94], [95]. In particular, the measurement vector is estimated as follows:

$$\boldsymbol{\delta V} = \boldsymbol{V}^{f_2} - \alpha \boldsymbol{V}^{f_1} \in \mathbb{R}^{Nh\times 1} \tag{7}$$

where $\boldsymbol{V}^{f_1} \in \mathbb{R}^{Nh\times 1}$ and $\boldsymbol{V}^{f_2} \in \mathbb{R}^{Nh\times 1}$ are the measurement vectors corresponding to current frequencies f_1 and f_2 and $\alpha > 0$ is a weight factor estimated as follows:

$$\alpha = \frac{\boldsymbol{V}^{f_1\,T}\boldsymbol{V}^{f_2}}{\left\|\boldsymbol{V}^{f_1}\right\|_2} \tag{8}$$

Fd-EIT is popular for its ability to detect minor changes in conductivity, even in the presence of large baseline conductivity variations. It is commonly used in applications where little to no impedance changes occur, such as in the detection of tumors and stroke [92], [93], taking advantage of the fact that each tissue type is characterized by its own relative impedance frequency spectrum [95]. However, fd-EIT also has some limitations since it requires complex hardware systems capable of generating broadband current signals and measuring the resulting voltage signals with high accuracy. Additionally, it can be sensitive to noise and other sources of interference, which can result in image artifacts.

In the following sections, for the sake of simplicity, we will use the notations $\boldsymbol{V}$, $\boldsymbol{U}$ and $\boldsymbol{\sigma}$ when referring to either absolute or difference EIT.

E. FORWARD PROBLEM

The EIT forward problem involves calculating the voltage and current distribution within Ω for every stimulating electrode pair, assuming a known conductivity distribution. Although there are a few alternative numerical methods used in EIT, such as BEM and MoM, in this section, we will focus on a brief description of the popular FEM-based formulation. For more information about the applications of BEM and MoM in EIT, we refer the reader to [96], [97], and [98]. The FEM, widely applied in the analysis of solid and fluid dynamics and electromagnetic fields, discretizes the SUT model domain (Ω) into a number of N_e elements and N_u nodes (vertices). In 2D and 3D EIT, usually triangular and tetrahedral elements are utilized, respectively, although higher-order shapes can also be used. Both the Galerkin and the Riesz approaches can be used in FEM. The former involves constructing a weak formulation of the problem, which is then discretized using a finite element basis [99], [100]. The Riesz method, on the other hand, involves using a Riesz basis, constructed using a set of orthogonal functions that satisfy certain mathematical properties. It is capable of solving the forward problem more efficiently than the Galerkin method [101]. However, the Galerkin method, whose application in EIT is described below, is more popular due to its easier implementation and its adaptability to complex geometries.

Assuming a weak solution $u_h(\boldsymbol{r})$ of the forward problem and expanding it at an orthonormal basis we define:

$$u_h(\boldsymbol{r}) = \Sigma_{i=1}^{N_u} u_i \phi_i(\boldsymbol{r}) \tag{9}$$

where $\phi_i : \Omega \rightarrow [0,1]$ describes polynomial basis functions (usually piecewise linear [102], [103]) that satisfy the following condition:

$$\phi_i(\boldsymbol{r}) = \left\{ \begin{array}{ll} 1, & \text{if } \boldsymbol{r} \text{ is the } i\text{-th vertex} \\ 0, & \text{if } \boldsymbol{r} \text{ is any other vertex} \end{array} \right\}.$$

The conductivity (or admittance) weak solution is of the form:

$$\sigma_h(\boldsymbol{r}) = \Sigma_{e=1}^{N_e} \sigma_e \psi_e(\boldsymbol{r}) \tag{10}$$

while it is usually described by a piecewise constant basis function $\psi_e : \Omega \rightarrow \{0,1\}$ on each element e:

$$\psi_e(\boldsymbol{r}) = \left\{ \begin{array}{ll} 1, & \text{if } \boldsymbol{r} \text{ in } e\text{-th element} \\ 0, & \text{if } \boldsymbol{r} \text{ not in } e\text{-th element} \end{array} \right\}.$$

In the following expressions, the notations ϕ_i and ψ_e instead of $\phi_i(\boldsymbol{r})$ and $\psi_e(\boldsymbol{r})$ are adopted for convenience.

Calderon has shown that for small $\boldsymbol{\sigma}$ deviations (1) can be written in the following billinear integral form [103], [104]:

$$\begin{aligned} &\int\int_{\Omega} \sigma(\boldsymbol{r}) \nabla u(\boldsymbol{r}) \cdot \nabla v(\boldsymbol{r}) dA \\ &= \oint_{\partial\Omega} \left(u(\boldsymbol{r}) \sigma(\boldsymbol{r}) \frac{\partial v(\boldsymbol{r})}{\partial \boldsymbol{n}} \right) dS, \quad \text{in } \Omega, \end{aligned} \tag{11}$$

where $v(\boldsymbol{r})$ is a potential test function. By utilizing (9), (10), (11) and the Green's second identity along with the CEM boundary equations (2)-(4), the following equation for each particular element Ω_e is derived (2D case) [105]:

$$\begin{aligned} &\int\int_{\Omega_e} \sigma_e \left(u_j \frac{\partial \phi_i}{\partial x} \frac{\partial \phi_j}{\partial x} + u_j \frac{\partial \phi_i}{\partial y} \frac{\partial \phi_j}{\partial y} \right) dA \\ &= \oint_{\partial\Omega_e} \phi_i \frac{1}{z_l} \left(u_j \phi_j - U_l \right) dS. \end{aligned} \tag{12}$$

Likewise for the 3D case. For each element domain Ω_e having n_e vertices, the following local matrices are structured [105]:

$$A_m(i,j) = \int\int_{\Omega_e} \sigma_e \left(\frac{\partial \phi_i}{\partial x} \frac{\partial \phi_j}{\partial x} + \frac{\partial \phi_i}{\partial y} \frac{\partial \phi_j}{\partial y} \right) dA, \ \boldsymbol{A}_m \in \mathbb{R}^{n_e \times n_e}, \tag{13}$$

$$A_z(i,j) = \oint_{\partial\Omega_e} \frac{1}{z_\ell} \phi_i \phi_j dS, \quad \boldsymbol{A}_z \in \mathbb{R}^{n_e \times n_e}, \tag{14}$$

and

$$A_u(i,j) = -\oint_{\partial\Omega_e} \frac{1}{z_\ell} \phi_i dS, \quad \boldsymbol{A}_u \in \mathbb{R}^{n_e \times n_e}. \tag{15}$$

The following global matrix that demonstrates the inverse of each electrode's contact impedance per the electrode's surface is also written:

$$\boldsymbol{A}_D = \text{diag}\left(\left[|E_\ell| z_\ell^{-1} \right]_{\ell=1}^{N} \right), \quad \boldsymbol{A}_D \in \mathbb{R}^{N \times N}, \tag{16}$$

where $|E_\ell|$ denotes ℓ-th electrode's surface area. By assembling the vertices and elements into a global admittance matrix form and considering the current injection and voltage measurement pattern used, a linear system of equations is formulated [105]:

$$\begin{bmatrix} \boldsymbol{A}_M + \boldsymbol{A}_Z & \boldsymbol{A}_V \\ \boldsymbol{A}_V^* & \boldsymbol{A}_D \end{bmatrix} \begin{bmatrix} \boldsymbol{u} \\ \boldsymbol{U} \end{bmatrix} = \begin{bmatrix} \boldsymbol{0} \\ \boldsymbol{I} \end{bmatrix}, \tag{17}$$

where $\boldsymbol{A}_M \in \mathbb{R}^{N_u \times N_u}$, $\boldsymbol{A}_Z \in \mathbb{R}^{N_u \times N_u}$ and $\boldsymbol{A}_V \in \mathbb{R}^{N_u \times N}$ are the globally assembled matrices from the corresponding local $\boldsymbol{A}_m$, $\boldsymbol{A}_z$ and $\boldsymbol{A}_u$ ones. In addition, $\boldsymbol{u} = [u_i]_{i=1}^{N_u}$ denotes the nodes' potentials, $\boldsymbol{U} = [U_\ell]_{\ell=1}^{N}$ the electrodes' potentials and $\boldsymbol{I} \in \mathbb{R}^{N \times 1}$ denotes the amount of current sourced or sunk per electrode. The $(N_u+N) \times (N_u+N)$ system of equations in (17) is usually solved using the Cholesky or the conjugate-gradient methods [106].

A number of research works have demonstrated that $\boldsymbol{\sigma}$ can be uniquely determined by the knowledge of the Dirichlet-to-Neumann (DN) map on a bounded domain [103], [107], [108]. The relation between the conductivity $\boldsymbol{\sigma}$ and the boundary voltages $\boldsymbol{U}$ is non-linear. However, for relatively small conductivity changes $\delta\sigma(\boldsymbol{r})$ around a reference relative conductivity value σ_o, the following weak integral form can be used to estimate the differential voltage between two electrodes:

$$\delta U_{d,m} = -\int\int_{\Omega} \delta\sigma(\boldsymbol{r}) \nabla_r u(I^d, \boldsymbol{r}) \cdot \nabla_r u(I^m, \boldsymbol{r}) dA \tag{18}$$

where $u(I^d, \boldsymbol{r})$ and $u(I^m, \boldsymbol{r})$ are the electric fields due to the d-th current stimulation (lead, $d \in \{1, 2, \ldots N\}$) and the m-th voltage measurement electrode pairs respectively ($m \in \{1, 2, \ldots, h\}$), that can be estimated using FEM [105]. The following linear approximation can be derived:

$$\boldsymbol{\delta U} = \frac{\partial \boldsymbol{\delta U}}{\partial \boldsymbol{\delta\sigma}}\Big|_{\boldsymbol{\sigma_o}} \boldsymbol{\delta\sigma} + \mathcal{O}(\|\boldsymbol{\delta\sigma}\|^2) \simeq \boldsymbol{J}\boldsymbol{\delta\sigma} \tag{19}$$

where $\boldsymbol{J} \in \mathbb{R}^{Nh \times N_e}$ denotes the Jacobian matrix, calculated as follows:

$$J_{d,m}^i = \frac{\partial \delta U_{d,m}}{\partial \delta\sigma_i} = -\int\int_{\Omega_i} \nabla_r u(I^d, \boldsymbol{r}) \cdot \nabla_r u(I^m, \boldsymbol{r}) dA \tag{20}$$

for the i-th element (column) and the current-voltage pattern indices d, m (row). The Jacobian matrix $\boldsymbol{J}$ reflects the sensitivity of the electrode voltages to perturbations in the conductivity of each element and is typically computed using the adjoint method [109]. Due to the ill-conditioned nature of the inverse problem, $\boldsymbol{J}$ can exhibit singular behaviour, which poses significant challenges for accurately estimating the conductivity distribution.

Fig. 2 illustrates how the sensitivity of electrode voltages to conductivity perturbations decreases as the perturbations move away from the domain boundary. The finite element simulations were carried out using the EIDORS library in MATLAB [110]. Specifically, a 2D circular domain with a unity radius and 16 electrodes was considered.

The domain was discretized into $N_u = 5327$ nodes and $N_e = 10262$ triangular elements. A 1mA current was applied, using the adjacent current and voltage pattern to two inhomogeneous cases: one with a circular perturbation of radius 0.2 that presented a 10% increase in conductivity relative to the homogeneous background and was centered at $(0.1, 0.6)$ and another appearing the same change centered at $(0, -0.1)$. As shown in Fig. 2, the voltage changes resulting from the second case were at least 10 times lower than those from the first case, demonstrating that detecting interior conductivity changes is challenging and requires high SNR systems.

Throughout the rest of this paper, N denotes the number of electrodes as before, h denotes the number of voltage measurements per current injection pair, N_e is the number of FEM elements, d stands for current stimulation, m for the number of voltage measurements and $\boldsymbol{J}$ symbolizes the Jacobian matrix, unless otherwise indicated.

III. CLASSICAL APPROACHES

This section performs an explanatory review of primary EIT image reconstruction approaches, beginning from the back-projection method and proceeding with the regularization-based, the GREIT, the D-Bar and the subspace optimization methods. In each approach, core theoretical concepts are elucidated, delineating implementation steps and analyzing inherent advantages and disadvantages. These approaches were selected based on their broad applicability, popularity and their foundational role in various methods and recent research modifications. In addition, variants and recent advancements are discussed, providing insights into their contributions and areas of application. Prior to this presentation, the issue of *inverse crime* is explained, while a brief review of the hyperparameter selection methods is performed at the end of this section.

A. INVERSE CRIME

In EIT, it is a common practice to evaluate the performance of a reconstruction algorithm using simulated data prior to testing it on real data. The simulated electrode voltage data is usually generated numerically on a 2D or 3D structural model, employing the FEM (see the previous section). Gaussian noise should also be added to the simulated measurement data to assess the algorithm's robustness. The image reconstruction is then performed using an inverse reconstruction model structure based on the algorithm tested.

However, using the same discretization for both the simulation and the reconstruction model can lead to *inverse crime*, resulting in an inaccurate representation of the inverse model's actual performance when applied to real data [68]. This discrepancy arises due to the differences in the actual system being measured, such as noise and model errors, which were not present in the simulated data. To avoid the inverse crime, it is crucial to reconstruct the image using an independent grid from the simulation model. Typically, a fine grid is used in the simulation model to obtain accurate measurement estimates, whereas a coarse grid is utilized in the inverse model to ensure computational efficiency.

B. BACK-PROJECTION

The back-projection (BP) algorithm is a fundamental image reconstruction method in X-Ray and CT imaging. In the earlier EIT research steps, it was applied as linear BP (LBP) [111]. The main approach is described by the determination of the voltage equipotential lines sensing areas and measurement data projection onto these areas' pixels. Each element's or pixel's conductivity change $\Delta\sigma(j) = \sigma_m - \sigma_o$, $j \in \{1, 2, \ldots N_e\}$ is then estimated by overlaying the projected data:

$$\Delta\sigma(j) = \frac{1}{N}\sum_{i=1}^{N}\frac{U_m(i,j) - U_o(i,j)}{U_o(i,j)} \tag{21}$$

for a number of N current excitation electrode pairs. In the expression above, U_o and U_m refer to the projected voltage data before and after the change in conductivity. This approach is relatively simple; however, it exhibits limited spatial resolution, image blurring and does not take into account any non-linear effects. Some modified versions of the original LBP have appeared more recently [112], [113]. Finally, an iterative version of the BP algorithm for EIT has also been presented in [114].

C. TRUNCATED SINGULAR VALUE DECOMPOSITION

In truncated singular value decomposition (TSVD), singular value decomposition (SVD) is performed on the Jacobian matrix $\boldsymbol{J}$:

$$\boldsymbol{J} = \boldsymbol{U}_{TS}\boldsymbol{\Sigma}_{TS}\boldsymbol{V}_{TS}^{*}, \tag{22}$$

where $\boldsymbol{U}_{TS} \in \mathbb{R}^{Nh\times Nh}$ and $\boldsymbol{V}_{TS} \in \mathbb{R}^{N_e\times N_e}$ are orthogonal matrices and $\boldsymbol{\Sigma}_{TS} \in \mathbb{R}^{Nh\times N_e}$ is a diagonal matrix that contains the singular values of the Jacobian matrix. Then, the singular values below a selected threshold L are truncated to zero, with the conductivity distribution estimated as follows:

$$\boldsymbol{\sigma}_{*} = \boldsymbol{V}_{TS}\tilde{\boldsymbol{\Sigma}}_{TS}\boldsymbol{U}_{TS}^{*}, \tag{23}$$

where $\tilde{\boldsymbol{\Sigma}}_{TS} = \mathrm{diag}(\tilde{s}_i) \in \mathbb{R}^{Nh\times N_e}$, with

$$\tilde{s}_i = \left\{ \begin{array}{ll} 1/s_i, & \text{if } s_i \geq L \\ 0, & \text{otherwise} \end{array} \right\}, \tag{24}$$

where s_i denotes the i-th singular value of $\boldsymbol{J}$. This actually acts as regularization, since by an appropriate threshold selection, TSVD can effectively suppress noise and other artefacts in the reconstructed images [115], [116]. However, it lacks of sufficient spatial resolution and robustness to modelling errors.

D. TIKHONOV AND L^2-NORM REGULARIZATION

Regularization is a widespread approach to dealing with ill-posed inverse problems. The EIT reconstruction problem can be approached as the minimization task of a cost function, which includes a least-squares (fidelity) term between the

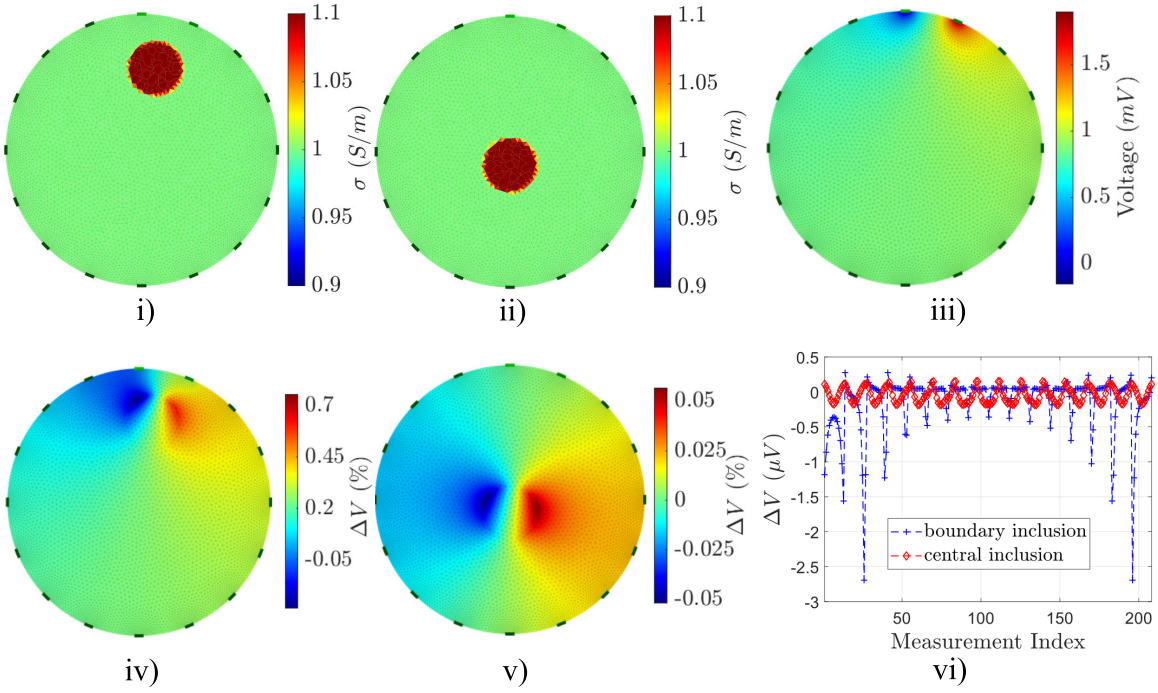

FIGURE 2. The soft field effect in a 2D circular EIT setup. i) With a conductive inclusion close to boundary. ii) With a conductive inclusion close to the center. iii) Homogeneous case voltage distribution when current is stimulated from the 1st and the 2nd electrodes. iv) Percentage of changes in voltage distribution due to the boundary inclusion. v) Percentage of changes in voltage distribution due to the central inclusion. vi) Changes in differential adjacent voltage measurements due to the conductive inclusions.

measurements $\boldsymbol{V}$ and the numerically estimated boundary voltages $\boldsymbol{U}(\boldsymbol{\sigma})$ and a regularization term $R(\boldsymbol{\sigma}) \in \mathbb{R}_+$ that prevents overfitting and offers stability to the solution:

$$F(\boldsymbol{\sigma}) = \|\boldsymbol{U}(\boldsymbol{\sigma}) - \boldsymbol{V}\|^2_{\boldsymbol{W}} + \lambda^2 R(\boldsymbol{\sigma}), \tag{25}$$

$$\boldsymbol{\sigma}_* = \underset{\boldsymbol{\sigma}\in\mathbb{R}^{N_e\times 1}}{\operatorname{argmin}} \Big\{F(\boldsymbol{\sigma})\Big\}. \tag{26}$$

where we consider the boundary voltage vector $\boldsymbol{U}$ as a function of $\boldsymbol{\sigma}$, $\boldsymbol{U} : \mathbb{R}^{N_e\times 1} \rightarrow \mathbb{R}^{Nh\times 1}$. In addition, $\boldsymbol{W} \in \mathbb{R}^{Nh\times Nh}$ is the noise positive definite inverse covariance matrix, $\|\boldsymbol{A}\|^2_{\boldsymbol{W}} = \boldsymbol{A}^T\boldsymbol{W}\boldsymbol{A}$ is a weighted vector norm of any vector $\boldsymbol{A}$ and $\lambda > 0$ is the regularization hyperparameter. By selecting λ, it is possible to control the trade-off between data fitting and regularization biasing. In practice, the hyperparameter λ is often chosen heuristically, although some techniques have been developed for its selection, such as the L-curve and the cross-validation [117] (see also subsection III-J). In standard Tikhonov regularization, the corresponding term is written as:

$$R(\boldsymbol{\sigma}) = \|\boldsymbol{\sigma}\|^2_2 \tag{27}$$

where $\|.\|_2$ denotes the Euclidean (l^2) norm. The l^2-norm optimization problem (25)-(27) is also called ridge regression. By using the linear approximation $\boldsymbol{U}(\boldsymbol{\sigma}) \simeq \boldsymbol{J}\boldsymbol{\sigma}$ (see also II-E and (19)), a single-step solution can be obtained as:

$$\boldsymbol{\sigma}_* = \boldsymbol{\sigma}_o + \Big(\boldsymbol{J}^T\boldsymbol{W}\boldsymbol{J} + \lambda^2\boldsymbol{I}\Big)^{-1}\boldsymbol{J}^T\boldsymbol{W}\boldsymbol{V} \tag{28}$$

where $\boldsymbol{I} \in \mathbb{R}^{N_e\times N_e}$ is the identity matrix. In the case of a-EIT, a homogeneous background conductivity estimation $\boldsymbol{\sigma_o}$ needs to be added. From a statistical point of view, the term (27) can be interpreted as a prior distribution over $\boldsymbol{\sigma}$. It is also assumed that $\boldsymbol{\sigma}$ is drawn from a Gaussian distribution with mean σ_o and an identity covariance matrix, while the noise signal has zero mean and covariance matrix $\boldsymbol{W}^{-1}$. Then, $\boldsymbol{\sigma}_*$ is the maximum a posteriori (MAP) estimation of the posterior distribution given the measured data $\boldsymbol{V}$ [16], [118]. In practise, Tikhonov regularization strengthens the diagonal terms of $\boldsymbol{J}^T\boldsymbol{J}$ to reduce its condition number.

In generalized Tikhonov regularization, (27) is replaced by (29) where the positive definite matrix $\boldsymbol{Q} \in \mathbb{R}^{N_e\times N_e}$, called prior filter matrix, is employed to enhance the conductivity distribution's prior knowledge:

$$R(\boldsymbol{\sigma}) = \|\boldsymbol{\sigma}\|^2_{\boldsymbol{Q}}. \tag{29}$$

The most popular approaches include the NOSER prior $\boldsymbol{Q} = \text{diag}(\boldsymbol{J}^T\boldsymbol{J})$ [15], the Laplace prior [17] and the Gaussian high pass filter [16], [17]. The single-step solution is obtained in a similar manner as in (28), where the $\boldsymbol{Q}$ matrix is used instead of the identity matrix.

When large conductivity contrasts occur, an iterative variant of Tikhonov regularization can be used to deal with the problem's non-linearity, based on the Gauss-Newton algorithm. Each update is performed as follows [1], [119]:

$$\boldsymbol{\sigma}^{\kappa+1} = \boldsymbol{\sigma}^{\kappa} + \alpha\Big((\boldsymbol{J}^{\kappa})^T\boldsymbol{W}\boldsymbol{J}^{\kappa} + \lambda^2\boldsymbol{Q}\Big)^{-1}.$$

$$\left((\boldsymbol{J}^{\kappa})^{T}\boldsymbol{W}\left(\boldsymbol{V}-\boldsymbol{U}(\boldsymbol{\sigma}^{\kappa})\right)+\lambda^{2}\boldsymbol{Q}(\boldsymbol{\sigma}_{o}-\boldsymbol{\sigma}^{\kappa})\right), \quad (30)$$

where κ is the previous iteration step and $\alpha > 0$ is a constant estimated through line search for the proper update. It is noted that in the conventional Gauss-Newton algorithm, the hyperparameter value λ remains constant. Otherwise, λ can be a decreasing function of index κ. If in addition, $\boldsymbol{Q} = \boldsymbol{I}$, iteration (30) becomes that of Levenberg-Marquardt [105], [120].

Another popular l^2-norm optimization variant is the Landweber reconstruction [121], which is based on the steepest descent algorithm [122]. The conventional iterative Landweber update rule is:

$$\boldsymbol{\sigma}^{\kappa+1} = \boldsymbol{\sigma}^{\kappa} + \alpha_1(\boldsymbol{J}^{\kappa})^{T}\left(\boldsymbol{V}-\boldsymbol{J}^{\kappa}\boldsymbol{\sigma}^{\kappa}\right)+\alpha_2\boldsymbol{Q}^{T}\boldsymbol{Q}\boldsymbol{\sigma}^{\kappa}, \quad (31)$$

where α_1 and α_2 are hyperparameters corresponding to the fidelity and the regularization term step respectively.

In td-EIT applications, the l^2-norm regularization scheme can be properly modified in order to be transformed to a state-space model and solved recursively according to an extensive Kalman-filter context. The first Kalman filter implementation that tracks fast conductivity changes in thoracic EIT was presented in [123]. Extended version of the Kalman filter were later used in circular phantom experiments in [124] and [125].

Although Tikhonov regularization has been around for nearly three decades, it remains the most widely used approach for EIT reconstruction due to its relative simplicity and the availability of open-source libraries for implementation. Additionally, recent progress has been made in developing variants of Tikhonov regularization. For example, in [126], an adaptive hyperparameter selection approach was introduced. In [127], the prior regularization filter was modified to incorporate a priori knowledge of lung structure for lung cancer monitoring. Furthermore, in [128], homotopic mapping was adopted in an iterative Tikhonov regularization scheme, along with a Krylov subspace-based projection to improve both spatial and temporal resolution. Finally, in [129], a direct Landweber approach is used for two-phase flow electrical resistivity imaging in a phantom with acrylic rods.

E. TOTAL VARIATION REGULARIZATION

The total variation (TV) regularization incorporates an l^1-norm regularization term into the optimization function (25). In the fields of medical imaging and data science it is also called fused lasso regression [130], [131]. TV allows steep conductivity changes to be reconstructed without the smoothing effect introduced by l^2-norm priors. The regularization term is written as follows:

$$R(\boldsymbol{\sigma}) = \sum_{i=1}^{N_{ed}} \sqrt{\|\boldsymbol{L}_i\boldsymbol{\sigma}\|_2^2+\beta}. \quad (32)$$

where the matrix $\boldsymbol{L} \in \mathbb{R}^{N_{ed}\times N_e}$ quantifies the relationship between the domain's N_{ed} edges and the corresponding N_e elements. $\boldsymbol{L}_i$ denotes the i-th row of the matrix $\boldsymbol{L}$ and the parameter $\beta > 0$ guarantees the term's differentiability at zero $\boldsymbol{\sigma}$ [24].

The TV optimization problem defined by (25) and (32) can be solved using several techniques, such as the primal-dual interior point method (PD-IPM) [23], [24], [25], the alternating direction method of multipliers (ADMM) [25], [32] and the split-Bregman distance method [33], [34], [35], [132], [133], [134]. Since the problem is non-linear, these techniques require iterative procedures without the existence of a closed-form solution. Careful hyperparameter tuning can enable TV to preserve sharp edges and small features in the reconstructed images, preventing the blurring effect. However, the application of TV is computationally expensive compared to l^2-norm regularization techniques and involves the non-trivial and time-consuming process of hyperparameter selection. Additionally, the TV regularization may introduce significant artefacts in homogeneous conductivity regions due to the inclusion of high-frequency components. A recent effort to address the latter is the introduction of a fractional-order TV regularization prior scheme, applied in capacitively coupled EIT [135]. Finally, an improved convergence rate l^1-norm optimization method is the fast iterative shrinkage/thresholding algorithm (FISTA). FISTA is based on gradient descent and implies regularization through a proximal shrinkage/soft threshold operator and Nesterov acceleration [136]. In the field of EIT, the FISTA is applied in brain injury monitoring [137], while a regularization solver guided FISTA is proposed in [138], introducing an adaptive weight coefficient selection approach to reduce the image artefacts.

F. HYBRID REGULARIZATION APPROACHES

The definition of hybrid regularization (also called elastic-net regularization) includes a set of approaches that combine l^2-norm and l^1-norm weighted regularization terms in the optimization function. Its general optimization function formula is written as:

$$F(\boldsymbol{\sigma}) = \|\boldsymbol{U}(\boldsymbol{\sigma})-\boldsymbol{V}\|_{\boldsymbol{W}}^2+\lambda_1^2\|\boldsymbol{\sigma}\|_{\boldsymbol{Q}}^2+\lambda_2^2\|\boldsymbol{\sigma}\|_1. \quad (33)$$

Such approaches take advantage of both the stabilization capabilities of the l^2-norm term and the sparsity and sharpness of the l^1-norm term. [139] gives an extensive description of the elastic-net method and its applicability in image processing. In [140] an adaptive weighted hyperparameter, defined as a function of conductivity gradients, is used to control the trade-off between the Tikhonov and TV priors. Additionally, [141] describes a non-linear difference EIT method which employs a smooth prior term for the absolute conductivity and a TV prior term for the conductivity change which is constrained in a particular region of interest (ROI). The method was extended in 3D structures demonstrating its robustness in shape mismatches [142]. In [143], a framework which formulates the optimization function with an l^1-norm measurement data term and l^p-norm regularization term for electromagnetic tomography is

introduced. The work presented in [144], which describes a regularized *orthogonal matching pursuit* approach for electrical resistance tomography, could be also classified in this category. Furthermore, [145] applies a non-linear and non-convex algorithm based on the homotopy method to perform electrical resistance tomography. Although hybrid regularization approaches combine the advantages of both Tikhonov and TV regularization, the selection of multiple hyperparameters' values is very challenging and the whole process computationally expensive.

G. GREIT

The Graz consensus reconstruction algorithm for EIT (GREIT) was introduced in 2009 [31] as a popular pixel-wise linear approach, where a reconstruction matrix based on the Wiener filter is formulated. The GREIT hyperparameters are automatically optimized using a series of figures of merit (FoM) in a training process. This process entails using a set of K simulated 3D fine-model conductive target cases along with their corresponding measurement vectors. The reconstruction process is performed on a coarse pixel model, while a mapping tensor between the fine and coarse structure model is calculated. In the case of 2.5D GREIT reconstruction, which is often exploited, the fine forward model is 3D and the coarse reconstruction model is 2D.

In GREIT, a target noise figure (NF) FoM is selected according to the desired spatial resolution and the following reconstruction matrix is formulated:

$$\boldsymbol{R} = \tilde{\boldsymbol{X}}_t \boldsymbol{Y}_t^T \left(\boldsymbol{J}\boldsymbol{\Sigma}_{\boldsymbol{x}}\boldsymbol{J}^T + \boldsymbol{\Sigma}_{\boldsymbol{n}}\right)^{-1}, \quad \boldsymbol{R} \in \mathbb{R}^{N_e \times Nh}, \tag{34}$$

where $\tilde{\boldsymbol{X}}_t \in \mathbb{R}^{N_e \times K}$ is the normalized matrix of the K training samples desired positions $(\tilde{\boldsymbol{x}}^{(1)}, \tilde{\boldsymbol{x}}^{(2)}, \ldots, \tilde{\boldsymbol{x}}^{(K)})$, $\tilde{\boldsymbol{Y}}_t \in \mathbb{R}^{Nh \times K}$ is the normalized matrix of the corresponding measurement vectors $(\tilde{\boldsymbol{y}}^{(1)}, \tilde{\boldsymbol{y}}^{(2)}, \ldots, \tilde{\boldsymbol{y}}^{(K)})$, $\boldsymbol{\Sigma}_{\boldsymbol{x}} \in \mathbb{R}^{N_e \times N_e}$ is the covariance matrix of the training targets set distribution and $\boldsymbol{\Sigma}_{\boldsymbol{n}} \in \mathbb{R}^{Nh \times Nh}$ is the covariance matrix of the measurements' signal noise distribution. The optimization function imposed is:

$$F(\boldsymbol{R}) = \sum_{k=1}^{K} \left\| \tilde{\boldsymbol{x}}^{(k)} - \boldsymbol{R}\boldsymbol{y}^{(k)} \right\|_{\boldsymbol{W}}^2 \tag{35}$$

By using the $\boldsymbol{R}$ matrix that minimizes (35), the conductivity distribution is estimated according to the following linear formula:

$$\boldsymbol{\sigma}_* = \boldsymbol{R}\boldsymbol{V}. \tag{36}$$

GREIT is widely used for both 2D and 3D lung imaging [146], [147], [148]. One of the key advantages of GREIT is its ability to provide high spatial resolution images of the internal structures of the lungs. In addition, GREIT has an automatic hyperparameter tuning mechanism that makes it easier to use compared to other EIT algorithms. This feature helps to optimize the algorithm's parameters without the need for manual intervention, which can be a time-consuming process. On the other hand, the necessity of a fine forward pixelwised model often makes GREIT computationally expensive, which is a hard drawback for real-time lung imaging applications.

H. D-BAR

The D-Bar EIT reconstruction method provides a direct EIT image using a non-linear inverse Fourier transformation. It approximates the Dirichlet-to-Neumann (DN or voltage-to-current) map on the SUT boundary $\partial\Omega$ [26], [27], [28], [29]. In D-Bar, the EIT governing equation (1) is transformed to Schrodinger's equation on the complex plane $z = z_1 + iz_2 \in \mathbb{C}$ through the following substitution $q(z) = \sigma^{-\frac{1}{2}}(z)\Delta\sigma^{\frac{1}{2}}(z)$ and $\tilde{u}(z) = \sigma^{\frac{1}{2}}(z)u(z)$. Then, the following equation is derived:

$$(-\Delta + q(z))\tilde{u}(z) = 0, \quad z \in \Omega \tag{37}$$

Assuming homogeneous $\sigma(z) = \sigma_o = 1$ near $\partial\Omega$ and extending the domain to the whole complex plane with $q(z) = 0$ in $\mathbb{C} \setminus \Omega$, (37) is satisfied by the Faddevv (complex geometrical optics-CGO) solutions $\psi(k, z)$, for any $z \in \mathbb{C}$ and $k = k_1 + ik_2 \in C \setminus \{0\}$ [26]. CGOs are special Schrodinger's equation solutions that have an asymptotic behaviour to e^{ikz} far from the plane origin.

Next, by defining the expressions:

$$\mu(z, k) \triangleq e^{-ikz}\psi(z, k), \tag{38}$$

$$k\,z \triangleq (k_1 + ik_2)(z_1 + iz_2) \tag{39}$$

and

$$e(z, k) \triangleq exp\{i(kz + \bar{k}\bar{z})\} \tag{40}$$

and by using the non-linear Fourier scattering transform:

$$\boldsymbol{t}(k) = \int_{\mathbb{C}} e(z, k)q(z)\mu(z, k)dz \tag{41}$$

and the Alessandrini's identity [149], the following transformation can be derived:

$$\boldsymbol{t}^{\boldsymbol{exp}}(k) = \left\{ \begin{array}{l} \int_{\partial\Omega} e^{i\bar{k}\bar{z}}(\Lambda_\sigma - \Lambda_1)e^{ikz}dS(z), \quad 0 < |k| \leq R \\ 0, \quad \text{otherwise} \end{array} \right\}. \tag{42}$$

In the expression above, R is a low pass-filter cut-off "regularization" hyperparameter, while Λ_σ and Λ_1 denote the DN maps for the non-homogeneous and the homogeneous conductivity distribution cases respectively. The DN map, which is approximated by the admittance matrix in (17), is defined as the inverse of the Neumann-to-Dirichlet (ND or current-to-voltage) map R_σ which satisfies the following expression:

$$R_\sigma j = u|_{\partial\Omega} \tag{43}$$

where j denotes the current density distribution on $\partial\Omega$. By defining the differentiation operator $\bar{\partial}_k = \frac{\partial}{\partial k_1} + i\frac{\partial}{\partial k_2}$, the D-Bar equation is formulated:

$$\bar{\partial}_k \mu(z, k) = \frac{1}{4\pi\bar{k}} \boldsymbol{t}(k)e(z, -k)\overline{\mu(z, k)} \tag{44}$$

A solution can be derived using the second kind Fredholm integral equation:

$$\mu^{exp}(z,\kappa) = 1 + \frac{1}{4\pi^2}\int_{\mathbb{C}} \frac{\boldsymbol{t}^{\boldsymbol{exp}}(k)e(z,-k)}{(\kappa-k)\bar{k}}\overline{\mu^{exp}(z,k)}d\kappa_1 d\kappa_2. \tag{45}$$

Finally, an estimation of the conductivity distribution σ^{exp} can be obtained from the square of μ^{exp} when k tends to zero:

$$\sqrt{\sigma^{exp}(z)} = \lim_{k\to 0}\mu^{exp}(z,k), \quad z\in\Omega. \tag{46}$$

The D-Bar method has been shown to be robust to modelling errors, signal noise and both isotropic and anisotropic conductivities. It has been applied to both a-EIT and td-EIT for either biomedical and industrial EIT imaging [150] and is associated with the trigonometric current pattern [151], [152]. Unlike linear and non-linear regularization techniques that assume systematic properties of the signal noise and conductivity distribution, the D-Bar initially assumes noise-free data, with filtering applied in the transformation step (42) [152]. The D-Bar method is extensively compared with GREIT and Laplace prior Tikhonov regularization in [152]. This study includes a variety of test-cases, evaluation with quantitative FoMs, while it analyses the impact of hyperparameter's selection. In addition, a recent work applies a-priori radar data information about the perturbation's position in the D-Bar algorithm in order to increase the images' spatial resolution [153].

Finally, the Calderon method constitutes a linearized direct inverse-scattering reconstruction approach, based on the D-Bar one [154]. Contrary to the D-Bar, the Calderon method permits complex impedance map reconstruction, at the cost of reduced spatial resolution [155], [156]. In [157], the measurement patterns are modified in order to optimize the approximation of the CGO functions in the SUT interior. In [158], the Calderon method is applied in human chest EIT, by using the adjacent stimulation pattern. Finally, in [159], a 3D cyclinder implementation of the method is presented under various electrode configurations.

I. SUBSPACE OPTIMIZATION

The subspace optimization method (SOM) was presented in [160] as an inverse scattering problem solution approach and was firstly applied in EIT in [161]. The SOM framework utilizes the MoM to express the electric field in an N_e-subspace discretized domain to formulate the following two vectorized-form equations:

$$\bar{\boldsymbol{E}}_d^t = \bar{\boldsymbol{E}}_d^0 + \bar{\bar{\boldsymbol{G}}}_D\bar{\bar{\boldsymbol{\xi}}}\bar{\boldsymbol{E}}_d^t \tag{47}$$

and

$$\bar{\boldsymbol{V}}_d = \bar{\bar{\boldsymbol{G}}}_\partial\bar{\bar{\boldsymbol{\xi}}}\bar{\boldsymbol{E}}_d^t. \tag{48}$$

In the expressions above, $\bar{\boldsymbol{E}}_d^0 \in \mathbb{R}^{2N_e\times 1}$ denotes the homogeneous electric field for the d-th current pair injection (2-dimensional case), $\bar{\boldsymbol{E}}_d^t \in \mathbb{R}^{2N_e\times 1}$ the corresponding inhomogeneous field and $\bar{\bar{\boldsymbol{G}}}_D \in \mathbb{R}^{2N_e\times 2N_e}$ the dipole-Green function matrix, computed as $\bar{\bar{\boldsymbol{G}}}_D(\boldsymbol{r},\boldsymbol{r'})\cdot\boldsymbol{p} = -\nabla_r\Big[\nabla_{r'}G(\boldsymbol{r},\boldsymbol{r'})\cdot\boldsymbol{p}\Big]$ ($\boldsymbol{p}$ is an arbitrary dipole). Furthermore, $\bar{\bar{\boldsymbol{\xi}}} \in \mathbb{R}^{2N_e\times 2N_e}$ expresses the polarization tensor, which is a block diagonal matrix, with each element-block $i = \{1,2,\ldots,N_e\}$ defined as follows:

$$\bar{\bar{\boldsymbol{\xi}}}_i = A_i\Big[\sigma_i - \sigma_o\Big]\boldsymbol{I}_{2\times 2}, \quad \bar{\bar{\boldsymbol{\xi}}}_i \in \mathbb{R}^{2\times 2}, \tag{49}$$

where $A_i \in \mathbb{R}_+$ is the area (or volume) of the i-th subspace and $\boldsymbol{I}_{2\times 2} \in \mathbb{R}^{2\times 2}$ the unity matrix. In addition, $\bar{\boldsymbol{V}}_d \in \mathbb{R}^{h\times 1}$ is the voltage measurement matrix corresponding to the d-th current excitation and $\bar{\bar{\boldsymbol{G}}}_\partial \in \mathbb{R}^{h\times 2N_e}$ a boundary Green function, expressing the boundary potential from the axis-oriented component sources.

The induced constrast current (ICC) vector is defined for the bases-expansion SOM (BE-SOM) as follows:

$$\bar{\boldsymbol{J}}_d = \bar{\bar{\boldsymbol{\xi}}}\bar{\boldsymbol{E}}_d^t, \quad \bar{\boldsymbol{J}}_d \in \mathbb{R}^{2N_e\times 1}. \tag{50}$$

The ICC splits into a deterministic term $\bar{\boldsymbol{J}}_d^{det}$ and an ambiguous term $\bar{\boldsymbol{J}}_d^a$:

$$\bar{\boldsymbol{J}}_d = \underbrace{\sum_{i=1}^{L}\frac{\bar{\boldsymbol{u}}_i^*\bar{\boldsymbol{V}}_d}{s_i}\bar{\boldsymbol{v}}_i}_{\bar{\boldsymbol{J}}_d^{det}} + \underbrace{\bar{\bar{\boldsymbol{F}}}\bar{\boldsymbol{\alpha}}_d^k}_{\bar{\boldsymbol{J}}_d^a}, \tag{51}$$

where $\bar{\boldsymbol{J}}_d^{det}$ is derived from (47),(49) and (50), by performing TSVD (see subsection III-C). Furthermore, in the $\bar{\boldsymbol{J}}_d^a$ term, $\bar{\bar{\boldsymbol{F}}} \in \mathbb{R}^{2N_e\times k}$ is the Fourier transform matrix and $\bar{\boldsymbol{\alpha}}_d^k \in \mathbb{R}^{k\times 1}$ a vector of the k first low frequency 2-dimensional Fourier coefficients, corresponding to the d-th current excitation. The following objective function is then defined [60], [161]:

$$F(\bar{\boldsymbol{\alpha}}_1^k,\bar{\boldsymbol{\alpha}}_2^k,\ldots,\bar{\boldsymbol{\alpha}}_N^k,\bar{\bar{\boldsymbol{\xi}}}) = \sum_{d=1}^{N}\left(\frac{\Delta_d^{fid}}{\left\|\bar{\boldsymbol{V}}_d\right\|_2^2} + \frac{\Delta_d^{sta}}{\left\|\bar{\boldsymbol{J}}_d^{det}\right\|_2^2}\right), \tag{52}$$

where Δ_d^{fid} is the residual of (48):

$$\Delta_d^{fid} = \left\|\bar{\bar{\boldsymbol{G}}}_\partial\bar{\boldsymbol{J}}_d^{det} + \bar{\bar{\boldsymbol{G}}}_\partial\bar{\bar{\boldsymbol{F}}}\bar{\boldsymbol{\alpha}}_d^k - \bar{\boldsymbol{V}}_d\right\|_2^2 \tag{53}$$

and Δ_d^{sta} is the residual of (50):

$$\Delta_d^{sta} = \left\|\bar{\bar{\boldsymbol{F}}} - \bar{\bar{\boldsymbol{\xi}}}(\bar{\bar{\boldsymbol{G}}}_D\bar{\bar{\boldsymbol{F}}}) - \bar{\bar{\boldsymbol{\xi}}}(\bar{\boldsymbol{E}}_d^0 + \bar{\bar{\boldsymbol{G}}}_D\bar{\boldsymbol{J}}_d^{det}) - \bar{\boldsymbol{J}}_d^{det}\right\|_2^2. \tag{54}$$

In the BE-SOM, a regularization (usually TV, see subsection III-E) term $R(\bar{\bar{\boldsymbol{\xi}}})$ is also added in (52) [60]. The iterative process followed to find $\bar{\bar{\boldsymbol{\xi}}}$ and $\bar{\boldsymbol{\alpha}}_d^k$ that minimize (52) can be briefly described as follows. Firstly, $\bar{\bar{\boldsymbol{\xi}}}$ and $\bar{\boldsymbol{\alpha}}_d^k$ are properly initialized. Secondly, $\bar{\boldsymbol{\alpha}}_d^k$ is updated, adding the Polak-Ribiere-Polyak (RBR) conjugate gradient $\bar{\boldsymbol{\rho}}_n^d$ [162] multiplied with the line-search length l_n^d (n-th iteration):

$$\bar{\boldsymbol{\alpha}}_{d,n}^k = \bar{\boldsymbol{\alpha}}_{d,n-1}^k + l_n^d\bar{\boldsymbol{\rho}}_n^d. \tag{55}$$

Furthermore, the ICC $\bar{\boldsymbol{J}}_d$ and the total electric field $\bar{\boldsymbol{E}}_d^t$ should be updated using (51) and (47)-(50) respectively.

Then, ignoring the regularization term and directly minimizing the quadratic-type objective function (52), the following initial solution is acquired for $\bar{\xi}$ within each subunit i:

$$\bar{\xi}_i^{n,0} = \left(\sum_{d=1}^{N} \frac{\bar{E}_{d,n,i}^{t*}}{\|\bar{J}_d^{det}\|_2} \frac{\bar{J}_{p,n,i}}{\|\bar{J}_d^{det}\|_2} \right) \cdot \left(\sum_{d=1}^{N} \frac{\|\bar{E}_{d,n,i}^{t}\|_2^2}{\|\bar{J}_d^{det}\|_2^2} \right)^{-1}. \tag{56}$$

The polarization tensor $\bar{\xi}$ is then updated within an inner loop as follows:

$$\bar{\xi}^{n,h} = \bar{\xi}^{n,h-1} + l_h \bar{\rho}_h, \tag{57}$$

until a defined maximum number of iterations is satisfied ($h = h_{max}$). The whole process is repeated until the outer loop iterations reach a defined maximum number ($n = n_{max}$).

The BE-SOM demonstrates improved spatial resolution and successfully treats the inverse problem's non-linearity. On the other hand, it has the drawbacks of increased complexity and slow convergence [60]. In [60] a TV regularization term is added in the optimization scheme, within a deep-learning context of dominant currents. In addition in [61] the BE-SOM framework is enhanced using induced-current deep learning (see also section VI). Finally, in [163], two adaptively regularized BE-SOM are proposed, including an l^1-norm TV and an adaptively multiplicative weighted l^2-norm regularization.

J. HYPERPARAMETER SELECTION METHODS

In the regularization-based inverse problem approaches, the selection of proper hyperparameter values is crucial for the images' quality. In practical terms, the corresponding values are often tuned until the qualitative and/or quantitative specifications of the produced image are satisfied. However, in many cases this method is non-straightforward and inefficient. In an effort to automate the hyperparameter selection process, a variety of algorithms have been developed.

The *L-curve* method, discussed in [164] and [165], is based on the curve which demonstrates the relation between the fidelity and the regularization norm terms. The optimal hyperparameter value is located at its maximum curvature (corner) point. Although the L-curve method is very popular, it does not apply in cases where a corner cannot be indicated [117].

In the *Generalized cross-validation* (GCV) [165], the hyperparameter is chosen as the minimization point of the following function:

$$GCV(\lambda) = \frac{\|\boldsymbol{J}\boldsymbol{\sigma}_* - \boldsymbol{V}\|_{\boldsymbol{W}}^2}{\left(tr\left(\boldsymbol{Q} - (\boldsymbol{J}^T\boldsymbol{W}\boldsymbol{J} + \lambda^2\boldsymbol{Q})^{-1}\boldsymbol{J}^T\boldsymbol{W}\boldsymbol{J}\right)\right)^2}, \tag{58}$$

where $\boldsymbol{\sigma}_*$ is an initial estimate of the conductivity distribution, usually derived through a heuristically chosen hyperparameter. GCV does not involve the penalty term $R(\boldsymbol{\sigma})$ in its estimation; however, it requires an initial estimation $\boldsymbol{\sigma}_*$ and is computationally expensive [166].

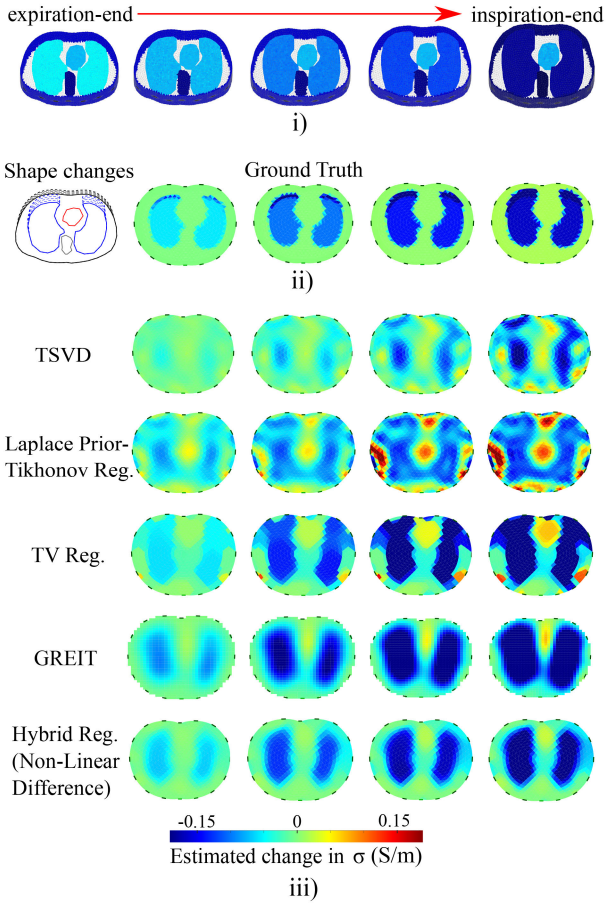

FIGURE 3. A td-EIT thoracic reconstruction simulation during the breathing process. i) The CT-based 3-dimensional fine models corresponding 5 discrete states between the expiration and the inspiration-ends. ii) A 2-dimensional sketch of the tissues' shape changes and the interpolated 2-dimensional inverse model ground truth. iii) Reconstructed images using TSVD, non-linear Laplace prior Tikhonov regularization, TV regularization with PD-IPM, GREIT and non-linear difference hybrid regularization [142].

In the *NF* method, which is introduced in [16], a target ratio of the measurements and image SNR is selected, while λ is derived through a line or logarithmic search method. Apart from GREIT, NF is also applied in common regularization techniques, with the drawback of high computational cost.

Finally, the *BestRes* method [117], is based on the optimal curvature point of a resolution curve that demonstrates the relation between log(λ) and the blur radius of a reconstructed conductivity inclusion. Despite the BestRes has shown interesting results, numerous EIT images are required to extract the resolution curve.

A comparison summary of the conventional EIT methods, including their basic concept, their advantages and disadvantages as well as relevant resources can be found in Table 1. In addition, Fig. 3 presents simulation results of dynamic thoracic image reconstruction using 5 conventional and popular techniques. To visually evaluate each method's robustness, this simulation includes shape and conductivity

changes of the tissues during the inhalation process. Mismatches between the 3-dimensional CT-based simulation models and the coarse 2-dimensional inverse model are also deliberately introduced. In particular, the simulation models are comprised of 130000 − 160000 tetrahedral elements and 27000 − 32000 nodes, depending on the breathing state (see Fig. 3 a), while the inverse model is comprised of 1024 triangular elements and 545 nodes. A Gaussian noise of −50dB SNR has also been added to the simulated measurements to evaluate each method's robustness (see also subsection III-A). In the regularization-based approaches, the hyperparameter was heuristically selected in order to maximize the Pearson correlation coefficient (PCC) of each image, while in the GREIT implementation, the target NF was set to 0.5. The MATLAB code used can be found in.[1]

IV. SHAPE RECONSTRUCTION APPROACHES

EIT conventional reconstruction approaches exhibit limited capability in accurately recovering the shapes of inclusions. This is crucial for medical applications, especially in lung and perfusion monitoring and the detection of malignant tissues, where organ and tissue shapes vary dynamically from patient to patient and over time. To address this challenge, shape reconstruction methods have been developed and applied in EIT. These methods transform the reconstruction problem of the conductivity map to a multi-phase flow problem, assuming a homogeneous reference background and piecewise constant conductivity inclusions. This approach significantly reduces the number of unknowns, thereby mitigating the ill-posed nature of the problem. The general optimization formula for shape-driven EIT reconstruction can be described as follows:

$$(\boldsymbol{\sigma_v}_*, \boldsymbol{\kappa}_*) = \underset{\boldsymbol{\kappa}\in\mathbb{R}^{N_b\times 1}, \boldsymbol{\sigma_v}\in\mathbb{R}^{(N_c+1)\times 1}}{\operatorname{argmin}} \Big\{ \|\boldsymbol{U}(\boldsymbol{\sigma_v}, \boldsymbol{\kappa}) - \boldsymbol{V}\|^2_{\boldsymbol{W}} + \lambda_1^2 \|\boldsymbol{\kappa} - \overline{\boldsymbol{\kappa}}\|^2_{\boldsymbol{Q}_1} + \lambda_2^2 \|\boldsymbol{\sigma_v} - \overline{\boldsymbol{\sigma_v}}\|^2_{\boldsymbol{Q}_2} \Big\}, \quad (59)$$

where N_b is the number of basis functions used, $\boldsymbol{\kappa} \in \mathbb{R}^{N_b\times 1}$ is a vector of properly defined basis functions' coefficients, N_c is the number of conductivity inclusions to be recovered, $\boldsymbol{\sigma_v} = [\sigma_o, \sigma_1, \ldots, \sigma_{N_c}]^T \in \mathbb{R}^{(N_c+1)\times 1}$ denotes the piecewise constant values of the homogeneous reference conductivity σ_o and the conductivity inclusions' values $\{\sigma_1, \sigma_2, \ldots, \sigma_{N_c}\}$. In addition, $\overline{\boldsymbol{\kappa}}$ and $\overline{\boldsymbol{\sigma_v}}$ denote the reference values for $\boldsymbol{\kappa}$ and $\boldsymbol{\sigma}$ respectively and $\boldsymbol{Q}_1 \in \mathbb{R}^{N_b\times N_b}$, $\boldsymbol{Q}_2 \in \mathbb{R}^{N_c\times N_c}$ the prior filter matrices used for the coefficients' and conductivities values' regularization terms respectively. A number of shape reconstruction approaches have been developed since the early 2010s and are briefly reviewed in this section.

A. PARAMETRIC LEVEL SET

The usage of level set functions is a common approach for shape reconstruction inverse problems [36]. At first, the traditional level set (TLS) was exploited [167], [168], [169] by expressing the conductivity distribution $\boldsymbol{\sigma}(\boldsymbol{r})$ as a mixture of piecewise constant conductivities in the domain Ω:

$$\boldsymbol{\sigma}(\boldsymbol{r}) = \sigma_o(1 - H_\epsilon(f(\boldsymbol{r}))) + \sum_{i=1}^{N_c} \sigma_i H_\epsilon(f(\boldsymbol{r})), \quad \boldsymbol{r} \in \Omega, \quad (60)$$

where H_ϵ is a smooth version of the Heaviside function to mantain differentiability of the optimization function [170] and $f(\boldsymbol{r}) = \sum_{i=1}^{N_b} \kappa_i p_i(\boldsymbol{r})$ is the level set function which is positive in the subdomains $D = D_1 \cup D_2 \cup \ldots \cup D_{N_c}$ that correspond to the N_c conductivity inclusions. In addition $[p_i(\boldsymbol{r})]_{i=1}^{N_b}$ denote the basis functions, with the radial basis functions (RBFs) to be a common choice. It is noted that in case the inclusions overlap, more level set functions should be used and $\boldsymbol{\sigma}(\boldsymbol{r})$ should also be properly defined [37].

The parametric level set (PLS) sets a threshold value $c > 0$ for the level set functions, maintaining more shape flexibility as well as reduced complexity and ill-posedness due to the dimensionality reduction [37], [39]. To express $\boldsymbol{\sigma}(\boldsymbol{r})$ in PLS, (60) is modified as:

$$\boldsymbol{\sigma}(\boldsymbol{r}) = \sigma_o(1 - H_\epsilon(f(\boldsymbol{r})) - c) + \sum_{i=1}^{N_c} \sigma_i(H_\epsilon(f(\boldsymbol{r})) - c). \quad (61)$$

The problem (59) can be solved using a non-linear minimization method, such as the Gauss-Newton one. The Jacobian matrix $\boldsymbol{J} \in \mathbb{R}^{(Nh)\times(N_c+N_b)}$ is computed by using the chain rule [39]:

$$\boldsymbol{J} = \frac{\partial \boldsymbol{U}(\boldsymbol{\sigma_v}, \boldsymbol{\kappa})}{\partial(\boldsymbol{\sigma_v}, \boldsymbol{\kappa})} = \begin{bmatrix} \boldsymbol{J}_{\sigma_0} \boldsymbol{J}_{\sigma_1} & \ldots \boldsymbol{J}_{\sigma_{N_c}} \boldsymbol{J}_{\kappa_1} & \ldots \boldsymbol{J}_{\kappa_{N_b}} \end{bmatrix}, \quad (62)$$

with

$$\boldsymbol{J}_{\sigma_i} = \frac{\partial \boldsymbol{U}(\boldsymbol{\sigma_v}, \boldsymbol{\kappa})}{\partial \sigma_i} = \frac{\partial \boldsymbol{U}(\boldsymbol{\sigma_v}, \boldsymbol{\kappa})}{\partial \boldsymbol{\sigma}} \cdot \frac{\partial \boldsymbol{\sigma}}{\partial \sigma_i}, \quad \boldsymbol{J}_{\sigma_i} \in \mathbb{R}^{Nh\times 1} \quad (63)$$

for $i = \{0, 1, \ldots, N_c\}$ and

$$\boldsymbol{J}_{\kappa_j} = \frac{\partial \boldsymbol{U}(\boldsymbol{\sigma_v}, \boldsymbol{\kappa})}{\partial \kappa_j} = \frac{\partial \boldsymbol{U}(\boldsymbol{\sigma_v}, \boldsymbol{\kappa})}{\partial \boldsymbol{\sigma}} \cdot \frac{\partial \boldsymbol{\sigma}}{\partial f} \cdot \frac{\partial f}{\partial \kappa_j}, \quad \boldsymbol{J}_{\kappa_j} \in \mathbb{R}^{Nh\times 1} \quad (64)$$

for $j = \{0, 1, \ldots, N_b\}$. For the computation of the conventional Jacobian matrix $\boldsymbol{J}_{\boldsymbol{\sigma}} = \frac{\partial \boldsymbol{U}(\boldsymbol{\sigma_v}, \boldsymbol{\kappa})}{\partial \boldsymbol{\sigma}}$ see subsection II-E.

Fig. 4 demonstrates the PLS concept in a simplified way: the inclusions are obtained by applying a threshold $c > 0$ on a linear combination of a PLS functions. Finally, the PLS was extended to td-EIT [171] (see also II-C).

B. MOVING MORPHABLE COMPONENTS

The moving morphable components (MMC) approach for shape reconstruction formulates the level set function $f(\boldsymbol{r})$ using analytical geometric features [172]. In particular, MMC assumes a number of n shape components that form an inclusion, a level set function $f = \max(f_1, f_2, \ldots, f_n)$ and applies the following function for each component i:

$$f_i(x, y) = 1 = \left(\frac{x'}{L_i}\right)^m - \left(\frac{y'}{g_i(x')}\right)^m \quad (65)$$

[1] https://github.com/chdim100/Thoracic-EIT-Imaging-Algorithms

TABLE 1. Comparison table of the classical EIT imaging approaches.

Method	Description	Advantages	Disadvantages	Resources
Back-Projection	Linear approach, based on measurement data projection in sensing areas	Simplicity	Low Spatial Resolution	[111]–[114]
TSVD	Linear approach, filters matrix singular values	Stability, simplicity, efficiency	Low Spatial Resolution	[115], [116]
Tikhonov Regularization	l^2-norm smooth prior. Linear or non-linear (Gauss-Newton)	Simple, fast, stabilizes ill-posed problem	Smoothens inclusion boundaries	[14]–[17], [126]–[128]
TV Regularization	l^1-norm sharp prior. Non-Linear.	Reconstructs sharp inclusion boundaries, prevents blurring	Hyperparameter selection, computationally expensive	[23]–[25], [32]–[35], [132]–[135], [137], [138]
Elastic-Net Regularization	Combined l^2-norm and l^1-norm priors	Stability, robustness, preserves boundaries, prevents blurring	Hyperparameters' selection, computationally expensive	[140]–[145]
GREIT	Wiener filter based pixel-wise linear approach	Optimized tuning, spatial resolution	Interpolation needed, computationally expensive	[31], [146]–[148]
D-Bar	Non-linear, based on scattering transformation	Robust to noise, modeling errors	Limited applicability, blurring effect	[26]–[29], [150], [152]
BE-SOM	Exploits ICC to reduce non-linarity and subspaces for stabilization	Spatial resolution, stability, robustness	Complexity, slow convergence	[60], [61], [161], [163]

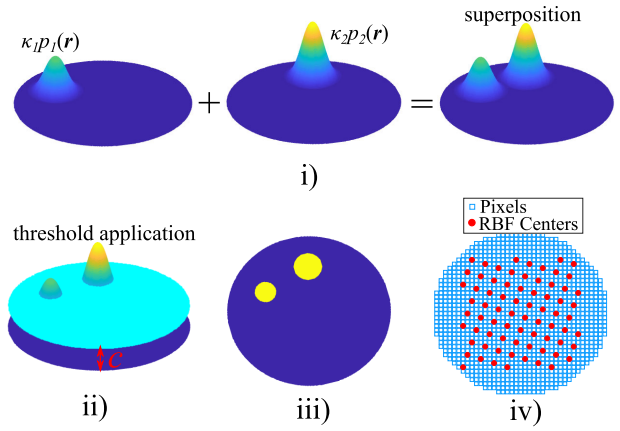

FIGURE 4. Visual representation of the PLS principle. i) Superposition of 2 RBFs. ii) Application of a threshold c. iii) Inclusions' shapes after the application of the threshold and the heaviside function H_ϵ. iv) Visual example of the distributed centers of a set of RBF functions that form $f(\boldsymbol{r})$.

where

$$\begin{bmatrix} x' \\ y' \end{bmatrix} = \begin{bmatrix} \cos(\theta_i) & \sin(\theta_i) \\ -\sin(\theta_i) & \cos(\theta_i) \end{bmatrix} \cdot \begin{bmatrix} x - x_o^i \\ y - y_o^i \end{bmatrix}, \tag{66}$$

$\boldsymbol{r} = (x, y)$, m is an even number, L_i the half length of the i-th component, θ_i is the corresponding component's tilted angle from the x-axis and (x_o^i, y_o^i) denotes the i-th component's geometric center. In addition, $g(x')$ describes the component's thickness which includes the parameters w_1^i, w_2^i and w_3^i [172]. Each component's vector $\boldsymbol{\kappa}^i \in \mathbb{R}^{1\times 7}$ in the optimization function (59) includes all the corresponding parameters:

$$\boldsymbol{\kappa}^i = [x_o^i,\ y_o^i,\ L_i,\ \theta_i,\ w_1^i,\ w_2^i,\ w_3^i]. \tag{67}$$

The problem can be solved similarly as in PLS, providing flexibility in the representation of the inclusions' geometries. However, the selection of $f(\boldsymbol{r})$ strongly affects the imaging performance [172], [173].

C. B-SPLINE LEVEL SET

The B-spline level set EIT shape reconstruction method makes use of a bivariate piecewise polynomial function of the following form:

$$f(x, y) = \sum_{i=0}^{m} \sum_{j=0}^{n} N_{i,k}(x) N_{j,l}(y) \kappa_{i,j} \tag{68}$$

which is in tensor product form between $N_{i,k}(x)$ and $N_{j,l}(y)$ that represent the i-th and j-th B-spline basis functions within a domain geometry that includes a total of $(m+1)\times(n+1)$ control points [174]. Furthermore, k and l denote the degrees of the corresponding basis functions and $\kappa_{i,j}$ denote the B-spline coefficients that are parametrized as unknowns.

The B-spline basis functions $N_{i,k}$ are derived through the following formulas:

$$N_{i,0}(x) = \begin{Bmatrix} 1, & x_i \le x \le x_i + 1 \\ 0, & \text{else} \end{Bmatrix} \tag{69}$$

and

$$N_{i,k}(x) = \frac{x - x_i}{x_{i+k} - x_i} N_{i,k-1}(x) + \frac{x_{i+k+1} - x}{x_{i+k+1} - x_{i+1}} N_{i+1,k-1}(x), \tag{70}$$

where

$$x_i = \begin{Bmatrix} 0, & i = 0, 1, \ldots, k \\ \frac{i-k}{m-k+1}, & i = k+1, k+2, \ldots, m \\ 1, & i = m+1, m+2, m+k+1 \end{Bmatrix}. \tag{71}$$

The sign of the level set function $f(x, y)$ is described as in TLS (positive within the inclusion D, zero on the inclusion's boundary ∂D or elsewhere) and an optimization problem (59) is formulated and solved for $(m+1)\times(n+1)+2$ unknowns (in the case of a single conductivity inclusion) [174]. Although the B-spline curve based shape reconstruction approach is capable to preserve the sharp inclusions' boundaries using low number of coefficients $\kappa_{i,j}$, it is necessary to know the number of inclusions prior to the reconstruction process.

D. BOOLEAN OPERATIONS FOR SHAPE RECONSTRUCTION

The Boolean operation-based shape reconstruction approach exploits Boolean operations between a number of N_l level set functions to model a number of N_c conductivity inclusions, with $N_l \geq N_c$. Each level set function corresponds to a specific shape primitive. For example, the union and the intersection of such primitives are obtained by estimating their maximum and minimum, respectively. In principle, each shape primitive is described by a closed curve $\boldsymbol{C}_i$ parameterized by a control point vector $\boldsymbol{P}^i$, with $i = \{1, 2, \ldots N_l\}$. The primitives are initialized and then updated through an optimization process similar to (59), where the control point vectors along with the conductivity level values are estimated. The process is described in detail in [173], where B-Spline curves are used to form the shape primitives. The Boolean operation method appears to have great capability in preserving sharp properties. On the other hand, some curves may intersect with themselves, causing irregular shape detection, while the corresponding Jacobian calculation is based on the perturbation method, which introduces numerical computation errors.

E. FOURIER REPRESENTATIONS

The Fourier shape reconstruction approach applies Fourier series to represent each shape's primitive curve (2D case):

$$\boldsymbol{C}_j = \begin{pmatrix} x_j(s) \\ y_j(s) \end{pmatrix} = \sum_{n=1}^{N_\theta} \begin{pmatrix} \gamma_n^{x_j} \theta_n^x(s) \\ \gamma_n^{y_j} \theta_n^y(s) \end{pmatrix}, \quad j = 1, 2, \ldots, N_l, \tag{72}$$

where N_l is the number of regions $D_j \subseteq \Omega$, $\theta_n(s)$ the periodic differential functions, $s \in [0, 1]$ the curve parameter and N_θ the order of the Fourier coefficients γ_n [38]. The basis functions are expressed as follows:

$$\theta_n^{x,y}(s) = \begin{cases} 1, & n = 1 \\ \sin\left(2\pi \frac{n}{2} s\right), & n = 2, 4, 6, \ldots N_\theta - 1 \\ \cos\left(2\pi \frac{n-1}{2} s\right), & n = 3, 5, 7, \ldots N_\theta \end{cases} \tag{73}$$

The Fourier coefficients γ_n form a vector $\boldsymbol{\Gamma} = [\boldsymbol{\gamma}_i]_{i=1}^{N_l} \in \mathbb{R}^{2N_\theta N_l \times 1}$, where $\boldsymbol{\gamma_i} = [\gamma_1^{x_i}, \ldots, \gamma_{N_\theta}^{x_i}, \gamma_1^{y_i}, \ldots, \gamma_{N_\theta}^{y_i}]^T \in \mathbb{R}^{2N_\theta \times 1}$. Additionally, signed distance functions are used to represent the level set functions:

$$f(\boldsymbol{r}, \boldsymbol{\gamma}_j) = \mu(\boldsymbol{r}) d(\boldsymbol{r}, \boldsymbol{C}_j(\boldsymbol{\gamma}_j)), \tag{74}$$

where $\boldsymbol{r} = (x, y)$ represents the finite element nodes' coordinates (2D), $\mu(\boldsymbol{r})$ is a sign function, which value is 1 within the corresponding region D_j, zero on $C_j = \partial D_j$ and -1 outside of it and $d(\boldsymbol{r}, \boldsymbol{C}_j(\boldsymbol{\gamma}_j))$ denotes the Euclidean distance between $\boldsymbol{r}$ and the region's boundary. Boolean union operations (see subsection IV-D) can be applied on a set of signed distance functions to acquire their maximum $\Phi(\boldsymbol{r}, \boldsymbol{\Gamma})$, which can be used as a heaviside function parameter to express the conductivity phase-flow map. A minimization problem, similar to (59) is considered, from which the $\boldsymbol{\gamma}_i$ coefficients are estimated.

F. FACTORIZATION METHOD

The factorization method (FM) is a non-iterative technique where the conductivity distribution is represented as follows:

$$\sigma(\boldsymbol{r}) = \sigma_o(\boldsymbol{r}) + \gamma(\boldsymbol{r}) \chi_D(\boldsymbol{r}), \tag{75}$$

where $\gamma(\boldsymbol{r})$ is a constant sign function that holds on $D \subseteq \Omega$ and $\chi_D(\boldsymbol{r})$ is an indicator (characteristic) function which is revealed from the inverse problem, using the knowledge of the DN map Λ_σ (see subsection III-H) [175]. Using the Neumann boundary conditions of the EIT governing equation (see also section II), the Green's function for the homogeneous conductivity case is defined [175], [176]. A free-space dipole potential function $\hat{\phi}_z^n(\boldsymbol{r}, \sigma_o(\boldsymbol{z}))$ is then computed (for a dipole between $\boldsymbol{r}$ and $\boldsymbol{z}$, $\boldsymbol{z} \in \Omega$), which holds for the homogeneous conductivity case and $\boldsymbol{n}$ is a dipole direction unity vector. In addition, by using a numerical method (FEM or BEM), the potential $V_z^n(\boldsymbol{r})$ which is related to the conductivity perturbations is estimated. The total potential in each case is defined as:

$$\phi_z^n(\boldsymbol{r}) = \hat{\phi}_z^n(\boldsymbol{r}, \sigma_o(\boldsymbol{z})) + V_z^n(\boldsymbol{r}) \tag{76}$$

The estimated potentials $\phi_z^n(\boldsymbol{r})$ are used to form a finite dimensional DN map approximation $\boldsymbol{\Sigma}_\sigma^N \in \mathbb{R}^{N_e \times Nh}$ of Λ_σ. At the same time, the following set of $L^2(\partial\Omega)$ functions is defined for each electrode's subdomain E_i:

$$f = \sum_{i=1}^{N} \chi_{E_i} f_i, \quad f_i \in \mathbb{R} \tag{77}$$

In addition, an orthogonal projector P^N which integrates the CEM boundary conditions [177] is defined as:

$$P^N f = \sum_{i=1}^{N} \chi_{E_i} \frac{1}{|E_i|} \left(\int_{E_i} f ds + \frac{1}{N} \int_{\mathcal{G}^N} f ds \right), \tag{78}$$

where $\mathcal{G}^N$ denotes the gap between the electrodes. By performing TSVD on $\boldsymbol{\Sigma}_\sigma^N \simeq \sum_{i=1}^{L} \sigma_i \boldsymbol{u}_i \boldsymbol{v}_i^T$ (see subsection III-C) for the first L singular values, we get the following approximation:

$$f^N(\boldsymbol{z}, \boldsymbol{n}) = \frac{1}{\sum_{i=1}^{L} (P^N \phi_z^n, \boldsymbol{u}_i)^2} \sum_{i=1}^{L} \frac{(P^N \phi_z^n, \boldsymbol{u}_i)^2}{\sigma_i}, \tag{79}$$

where $(.,.)$ denotes the inner product. Evaluation of the above formula for a specified number of dipoles gives the inverse of the indicator functions $\chi_D(\boldsymbol{r})$.

Overall, the FM can be applied for self-constrained piecewise analytic conductivity inclusions, providing a non-iterative shape estimation. However, prior knowledge of σ_o is needed, while the exact conductivity distribution values are not acquired [178], [179].

G. MONOTONICITY-BASED RECONSTRUCTION

Monotonicity-based EIT reconstruction is a non-iterative approach that utilizes the monotonicity property of the EIT measurements' behaviour to estimate the conductivity distribution within a subject under test (SUT). It exploits the observation that variations in the object's conductivity $\boldsymbol{\sigma}$ lead to predictable monotonic variations in the measured EIT data $\boldsymbol{V}$ [180], [181]. It has been applied in lung time-difference EIT imaging, assuming a linear approximation of the boundary voltages' time variation:

$$\frac{\partial U_{dm}(t)}{\partial t} = -\int_{\Omega} \frac{\partial \sigma(t,\boldsymbol{r})}{\partial t} \nabla_r u_o(I^d,\boldsymbol{r}) \cdot \nabla_r u_o(I^m,\boldsymbol{r}) dA \tag{80}$$

where $u_o(I^d,\boldsymbol{r})$ and $u_o(I^m,\boldsymbol{r})$ refer to the homogeneous case drive and lead potential distributions respectively [182]. The conductivity change rate in time is decomposed in two parts, related with the lung ventilation and cardiac perfusion respectively:

$$\frac{\partial \sigma(t,\boldsymbol{r})}{\partial t} = \frac{\partial \sigma_L(t,\boldsymbol{r})}{\partial t} + \frac{\partial \sigma_H(t,\boldsymbol{r})}{\partial t}, \tag{81}$$

while the ventilation related boundary voltages are numerically estimated as:

$$U_{dm,L}(t) = -\int_{\Omega} \sigma_L(t,\boldsymbol{r}) \nabla u_o(I^d,\boldsymbol{r}) \cdot \nabla u_o(I^m,\boldsymbol{r}) dA \tag{82}$$

and form a time-variant matrix $\boldsymbol{U}_L(t) \in \mathbb{R}^{N\times N}$. Furthermore, the constraints of increasing conductivity during exhalation and decreasing conductivity during inhalation are raised in Ω, while the boundary data is modified as follows:

$$\begin{aligned}\tilde{U}_{dm,L}(t) &= \frac{U_{dm,L}(t)}{\operatorname{sgn}\left(\int_{\Omega} \nabla_r u_o(I^d,\boldsymbol{r}) \cdot \nabla_r u_o(I^m,\boldsymbol{r}) dA\right)} \\ &+ \left(1 - \operatorname{sgn}\left(\int_{\Omega} \nabla u_o(I^d,\boldsymbol{r}) \cdot \nabla u_o(I^m,\boldsymbol{r}) dA\right) \bar{U}_{dm,L}\right).\end{aligned} \tag{83}$$

Finally, after the spatial discretization of the conductivity change rates in vectorized form, the following optimization problem is solved:

$$F\left(\frac{\partial \boldsymbol{\sigma_L}}{\partial t}\right) = \left\| \boldsymbol{J} \frac{\partial \boldsymbol{\sigma_L}}{\partial t} - \frac{\partial \boldsymbol{U}_L}{\partial t} \right\|_2^2 + \lambda^2 \left\| \frac{\partial \boldsymbol{\sigma_L}}{\partial t} \right\|_2^2 \tag{84}$$

subject to a monotonous conductivity change during each separate breathing state period (inhalation and exhalation). The problem above is also properly modified for the detection of local conductivity changes and inclusion shapes [182].

The monotonicity-based EIT reconstruction method effectively reconstructs convex-shaped conductivity inclusions and demonstrates robustness against noise. However, it requires knowledge of σ_o and may not be as efficient for non-convex shapes. Furthermore, non-linear extensions have been developed for the monotonicity approach [183].

H. GRADIENT-BASED OPTIMIZATION

The gradient-based optimization in EIT tends to minimize the following objective function:

$$F(\boldsymbol{\sigma}) = \sum_{d=1}^{N} \sum_{m=1}^{h} \left(\int_{e_d} \frac{V_{dm} - U_{dm}(\boldsymbol{\sigma})}{z_d} dS - I_{dm} \right)^2. \tag{85}$$

The notations in (85), are the same as mentioned in section II, except from d that refers both to the electrode and the current stimulation pair number. In the binary optimization framework presented in [184], a two-phase conductivity distribution is assumed, with the corresponding values defined as σ_o and σ_1. The conductivity distribution is formed by combining convex 2D shapes. The initial steps include shape parametrization, solution of the forward problem and evaluation of $F(\boldsymbol{\sigma})$. Initialization of the sample basis and reformulation of the minimization scheme by parametrizing $\boldsymbol{\sigma}$ as a function of the sample-based parameters $\mathcal{P} = \{\mathcal{P}_i\}_{i=1}^{N_b}$ and a weight vector $\boldsymbol{\alpha} = [\alpha_i]_{i=1}^{N_b}$, such as $\boldsymbol{\sigma}(\boldsymbol{r}) = \boldsymbol{\sigma}(\mathcal{P},\boldsymbol{\alpha})$ are then performed. The next step is to estimate the adjoint state $\psi(\boldsymbol{r})$ for each current injection I_l via the following problem:

$$\nabla\big(\sigma(\boldsymbol{r})\nabla\psi(\boldsymbol{r})\big) = 0, \quad \boldsymbol{r} \in \Omega \tag{86}$$

$$\frac{\partial \psi(\boldsymbol{r})}{\partial \boldsymbol{n}} = 0, \quad \boldsymbol{r} \in \partial\Omega \backslash \bigcup_{l=1}^{N} e_l \tag{87}$$

$$\psi(\boldsymbol{r}) + z_l \frac{\partial \psi(\boldsymbol{r})}{\partial \boldsymbol{n}} = 2\beta_l \left(\int_{e_l} \frac{V_l - u(\boldsymbol{r})}{z_l} dS + I_l \right), \tag{88}$$

where $\boldsymbol{r} \in e_l, l = 1,\ldots,N$ and $\beta_l > 0$ a constant. In addition, the gradients $F'(\boldsymbol{\sigma})$, $\nabla_{\mathcal{P}} F(\boldsymbol{\sigma})$ and $\nabla_{\boldsymbol{\alpha}} F(\boldsymbol{\sigma})$ are obtained as follows:

$$F'(\boldsymbol{\sigma}) = -\sum_{l=1}^{N} \nabla\psi^l(\boldsymbol{r}) \cdot \nabla u^l(\boldsymbol{r}), \tag{89}$$

$$\nabla_{\mathcal{P}} F(\boldsymbol{\sigma}) = \nabla_{\mathcal{P}} \boldsymbol{\sigma} F'(\boldsymbol{\sigma}), \tag{90}$$

$$\nabla_{\boldsymbol{\alpha}} F(\boldsymbol{\sigma}) = \bar{\boldsymbol{\sigma}} F'(\boldsymbol{\sigma}), \tag{91}$$

where $\bar{\boldsymbol{\sigma}}$ is the vector of conductivity samples. Furthermore, the control set $(\mathcal{P},\boldsymbol{\alpha})$ and the conductivity is updated in each iteration. Finally, coarse-scale binary tuning is performed to reach the final solution [184], [185].

The recently proposed gradient-based approach offers sufficient spatial performance and can be used with parallelization to reduce the computational costs. This provides the space for expansion at multiphase conductivity estimation problems with various convex shapes, making the method suitable for cancer detection applications [184]. Nevertheless,

gradient-based optimization methods require prior knowledge of the number of inclusions and their approximate positions and they still suffer from computational issues.

Additionally to the shape reconstruction approaches briefly described above, it is worth to mention the linear sampling method [186], the non-iterative enclosure-based method [187], the extended Kalman filtering for time-variant multiphase-flow boundary estimation [188], [189], [190], the BEM-based geometrically constrained boundary reconstructor (CGBR) [191]. A comparison summary of the shape EIT reconstruction methods can be found in Table 2. A more detailed summary can be found in [38].

V. POPULATION-BASED APPROACHES

In addition to regularization and shape reconstruction approaches, there exists a distinct category of algorithms in the field of EIT that address the reconstruction problem through the process of a population of individual candidate images. This section presents a concise overview of the utilization of genetic algorithms and particle swarm optimization in EIT.

A. GENETIC ALGORITHM

Genetic algorithm (GA) is a global random search meta-heuristic algorithm that mimics the biological evolution process. The goal is to find the optimal conductivity distribution within the domain that best matches the measured data by transforming the inverse problem to avoid its ill-posed and ill-conditioned nature. In particular, an objective function is formulated based on the summary of absolute boundary voltage differences terms.

$$F(\boldsymbol{\sigma}) = \sum_{i=1}^{Nh} \|U_i(\boldsymbol{\sigma}) - V_i\|\,, \tag{92}$$

where the conductivity values are bounded between a low σ_l and a high σ_h value. A fitness function $h(\boldsymbol{\sigma})$ is then defined as the reciprocal of $F(\boldsymbol{\sigma})$: $h(\boldsymbol{\sigma}) = 1/F(\boldsymbol{\sigma})$ and evaluated for a number (population) of M EIT images (individuals) that are initially randomly generated. For each individual and element the corresponding $\boldsymbol{\sigma}$ values are encoded (digitized) as L_p-bit binary strings:

$$\begin{aligned} x_{ij} = [\alpha_{ij}]_{k=1}^{L_p},\ \ i = \{1, \ldots, M\},\ j = \{1, \ldots, N_e\}, \\ \alpha_{ijk} \in \{0, 1\}, \end{aligned} \tag{93}$$

obtaining a precision of $\Delta x = (\sigma_h - \sigma_l)/(2^{L_p} - 1)$. The set of these strings completes the chromosome space. Then, each x_{ij} is decoded as follows:

$$\tilde{x_{ij}} = \sigma_l + \frac{\sigma_h - \sigma_l}{2^{L_p} - 1} \sum_{k=1}^{L_p} 2^{L_p - k} \alpha_{ijk}. \tag{94}$$

In [40], a three-stage GA for EIT was developed. Each stage involves the generation of an initial population of images, the selection of parent individuals for mating and genetic manipulation through crossover (see Fig. 5 for an example), as well as mutation operations. However, in each stage, different chromosomes are utilized for population generation. The process starts with the use of σ_l and σ_h chromosomes and subsequently continues with the selection of a conductivity distribution that maximizes the fitness function $h(\boldsymbol{\sigma})$. More recently, in [41], a proportional GA was proposed, where $h(\boldsymbol{\sigma})$ is optimized in a ratio form, in an effort to improve the convergence rate and the imaging quality. Until today, the application of GA in EIT is limited to 2D experimental tank cases.

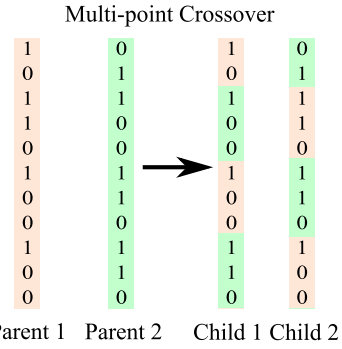

FIGURE 5. Example of a multiple-point crossover process.

B. PARTICLE SWARM OPTIMIZATION

Particle swarm optimization (PSO) [192] is a category of meta-heuristic algorithms that are based on the movement of a number of M particles (EIT images), that, as in the genetic algorithms, they are also randomly initialized. At each iteration κ and image i, PSO updates $\boldsymbol{\sigma}$ according to the following rule [42]:

$$\boldsymbol{\sigma}_i^{\kappa+1} = \boldsymbol{\sigma}_i^{\kappa} + \boldsymbol{v}_i^{\kappa+1}, \tag{95}$$

where $\boldsymbol{v}_i \in \mathbb{R}^{N_e \times 1}$ represents the i-th particle's velocity, estimated as follows:

$$\boldsymbol{v}_i^{\kappa+1} = w\boldsymbol{v}_i^{\kappa} + c_1 r_1(\boldsymbol{\sigma}_{il*}^{\kappa} - \boldsymbol{\sigma}_i^{\kappa}) + c_2 r_2(\boldsymbol{\sigma}_{g*}^{\kappa} - \boldsymbol{\sigma}_i^{\kappa}). \tag{96}$$

In addition, $w \in (0, 1)$ denotes the inertia weighting factor, $c_1 > 0$ and $c_2 > 0$ the cognitive and the social acceleration coefficient respectively, where $c_1 + c_2 \simeq 4$ while r_1 and r_2 are uniformly distributed values in $[0, 1]$. Furthermore, $\boldsymbol{\sigma}_{il*}^{\kappa}$ and $\boldsymbol{\sigma}_{g*}^{\kappa}$ denote the local and global best individuals respectively. In particular, the best local position is obtained within the neighbourhood Ne_i of the i-th particle:

$$\boldsymbol{\sigma}_{il*} = \underset{j \in Ne_i}{\operatorname{argmin}} \Big\{ F(\boldsymbol{\sigma}_j) \Big\}, \tag{97}$$

while the best global position is obtained within all the M candidates:

$$\boldsymbol{\sigma}_{g*} = \underset{j \in [0,M]}{\operatorname{argmin}} \Big\{ F(\boldsymbol{\sigma}_j) \Big\}, \tag{98}$$

where F is a defined minimization scheme. The PSO initialization and update process are briefly shown in Fig. 6.

TABLE 2. Comparison table of the shape EIT reconstruction approaches.

Method	Description	Advantages	Disadvantages	Resources
Parametric Level Set	Thresholding level set functions, dimensionality reduction	Shape flexibility, dimensionality reduction	Non-straightforward process for RBFs weights' ranges determination, smoothing effects	[37], [39], [171]
Moving Morphable Components	Level set function formulated with analytical geometric features	Shape flexibility, dimensionality reduction	Non-robust to level set function selection, smoothing effects	[172]
B-Spline Level Set	Bivariate piecewise polynomials for level set function	Preserves sharp inclusions, dimensionality reduction	A-priori knowledge of inclusions' number	[174]
Boolean Operations	Exploits Boolean operations to shape primitives to form inclusions	Preserves sharp inclusions	Inefficient when curves intersept, inaccurate Jacobian calculation	[173],
Fourier Representations	Applies Fourier series to form inclusions	Wide parametrization choices, dimensionality reduction, no a-priori knowledge needed	Complexity, sensitivity to modeling errors	[38]
Factorization	Non-iterative, expresses $\boldsymbol{\sigma}$ through indicator functions, uses Green functions dipoles and the DN map	Separate treatment of conductivity range bounds	Needs a-priori knowledge of σ_o, non-exact $\boldsymbol{\sigma}$ values acquired	[175]–[179]
Monotonicity	Non-iterative, utilizes the monotonicity property of the EIT data to estimate $\boldsymbol{\sigma}$	Noise robust, effective in convex-shaped inclusions	A-priori knowlegde of σ_o, inefficient for non-convex shapes	[180]–[183]
Gradient-Based Optimization	Iterative, $\boldsymbol{\sigma}$ formed by convex shapes, gradient evaluation of the minimization function	Spatial performance, parallelization can be employed	A-priori knowlegde of the inclusions' number, high computational cost	[184]
Geometrically Constrained Boundary Reconstructor	Local boundary parameterization penalized by BEM defined geometric constraints	Incorporates geometric constraints for regularization	A-priori knowledge of inclusions' number, smoothing effects	[191]

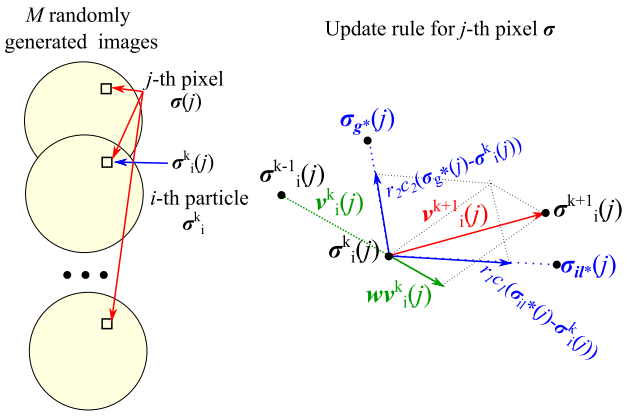

FIGURE 6. A brief demonstration of the PSO process, including the random population initialization and the update of a single-pixel conductivity.

In the case of EIT, PSO has been applied to simulate circular cases [42], where a comparison with Gauss-Newton and GA algorithms has been performed. In addition, fish-egg experimental data has been used in [47], where hybrid PSO was combined with an RBF NN to enhance imaging accuracy (see also section VI).

VI. SPARSE BAYESIAN LEARNING APPROACHES

Bayesian approaches offer an effective means of incorporating prior knowledge into the inverse problem. By estimating the posterior distribution, these methods provide a solution that considers both the observed data and the prior information. The Markov Chain Monte Carlo (MCMC) sampling is a popular general approach in this direction. However, MCMC is computationally expensive, which is undesirable, especially for real-time imaging applications. In the case of EIT, the primary focus is on finding the conductivity map $\boldsymbol{\sigma}_*$ that minimizes (or maximizes) a defined optimization procedure, rather than the full posterior distribution. The conductivity map $\boldsymbol{\sigma}_*$ is obtained through a maximum a-posteriori (MAP) estimation process, which represents the posterior mean. Sparse Bayesian learning (SBL) is an unsupervised learning technique that formulates the inverse problem from a Bayesian perspective [193]. The structure-aware SBL (SA-SBL), introduced and applied in EIT in [43], assumes a clustered sparse conductivity distribution, considering spatial correlation between the clusters. In particular, the minimization is defined as follows:

$$F(\boldsymbol{\sigma}) = \log P(\boldsymbol{V}|\boldsymbol{\sigma}) + \lambda \log P(\boldsymbol{\sigma}; \boldsymbol{\Theta}), \tag{99}$$

where $\boldsymbol{\Theta}$ denotes the hyperparameters' set.

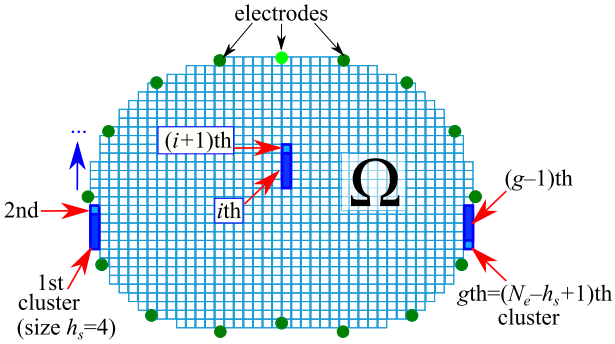

FIGURE 7. Example of a clustering structure in a thoracic shaped domain Ω (for $h_s = 4$).

A number of g overlapping clusters, with an equal size of h_s is considered, laid in a N_e-pixel area Ω. Then the EIT problem can be adapted to the SA-SBL framework by factorizing $\boldsymbol{\sigma}$ in the following way:

$$\boldsymbol{\sigma} = \boldsymbol{\Psi x} = [\boldsymbol{\Psi}_1, \ldots, \boldsymbol{\Psi}_g][\boldsymbol{x}_1{}^T, \ldots, \boldsymbol{x}_g{}^T]^T, \tag{100}$$

where $\boldsymbol{x}_i \in \mathbb{R}^{h_s \times 1}$ denotes the i-th cluster's weight value and $\boldsymbol{\Psi}_i = \left[\mathbf{0}^T_{(i-1)\times h_s}\ \boldsymbol{I}_{h_s \times h_s}\ \mathbf{0}^T_{(N_e-i-h_s+1)\times h_s}\right]^T \in \mathbb{R}^{N_e \times h_s}$. Fig. 7 demonstrates a simple example of a 2D domain's Ω cluster structure. The linear approximation (19) is then rewritten as:

$$\boldsymbol{V} = \boldsymbol{\Phi x} + \boldsymbol{e}, \tag{101}$$

where $\boldsymbol{\Phi} = \boldsymbol{J\Psi}$, $\boldsymbol{\Phi} \in \mathbb{R}^{Nh \times gh_s}$ and $\boldsymbol{e} \in \mathbb{R}^{Nh \times 1}$ denotes a Gaussian measurement noise, with $\boldsymbol{e} \sim \mathcal{N}(\mathbf{0}, \lambda \boldsymbol{I})$. For each cluster i we get the sub-matrix $\boldsymbol{\Phi}_i = \boldsymbol{J\Psi}_i \in \mathbb{R}^{Nh \times h_s}$. It is assumed that the prior of $\boldsymbol{x}$ obeys the following Gaussian distribution:

$$p\left(\boldsymbol{x}; \{\gamma_i, \boldsymbol{B}_i\}_{i=1}^g\right) = \mathcal{N}\left(\mathbf{0}, \boldsymbol{\Sigma}_0\right), \tag{102}$$

that has a zero-mean value and a covariance matrix $\boldsymbol{\Sigma}_0 \in \mathbb{R}^{gh_s \times gh_s}$ which is completed as follows:

$$\boldsymbol{\Sigma}_0 = \begin{bmatrix} \gamma_1 \boldsymbol{B}_1 & \ldots & \mathbf{0}_{\boldsymbol{h_s} \times \boldsymbol{h_s}} \\ \ldots & \ldots & \ldots \\ \mathbf{0}_{\boldsymbol{h_s} \times \boldsymbol{h_s}} & \ldots & \gamma_g \boldsymbol{B}_g \end{bmatrix}. \tag{103}$$

In the expression above, $\boldsymbol{\gamma} = [\gamma_i]_{i=1}^g \in \mathbb{R}^{g \times 1}$ and $\boldsymbol{B}_i \in \mathbb{R}^{h_s \times h_s}$ denote the i-th cluster's hyperparameters that along with λ, form the set $\boldsymbol{\Theta}$ in (99). Each cluster's coefficient γ_i can be initialized to one, while each block matrix $\boldsymbol{B}_i$ is initialized as $\boldsymbol{B}_i = \text{Toeplitz}\left(\left[1, 0.9^1, \ldots, 0.9^{h_s-1}\right]\right)$ and λ as:

$$\lambda = \frac{1}{100}\sqrt{\frac{1}{Nh-1}\sum_{i=1}^{Nh}|V_i - \overline{V}|^2}, \tag{104}$$

where V_i denotes the i-th measurement and $\overline{V}$ the average measurement value. A maximum a-posteriori (MAP) estimation of the $\boldsymbol{x}$ posterior mean $\boldsymbol{\mu_x} \in \mathbb{R}^{gh_s \times 1}$ and covariance matrix $\boldsymbol{\Sigma_x} \in \mathbb{R}^{gh_s \times gh_s}$ is derived through the learning process.

In the SA-SBL approach, the hyperparameters are iteratively updated to minimize:

$$F(\boldsymbol{\Theta}) = \ln|\boldsymbol{\Sigma_v}| + \boldsymbol{V}^T \boldsymbol{\Sigma_v}^{-1} \boldsymbol{V}, \tag{105}$$

where $\boldsymbol{\Sigma_v} = \lambda \boldsymbol{I} + \boldsymbol{\Phi\Sigma}_0\boldsymbol{\Phi}^T$. By using the expectation-maximization (EM) algorithm, the corresponding updates are given by:

$$\boldsymbol{\mu_x} = \boldsymbol{\Sigma}_0 \boldsymbol{\Phi}^T \boldsymbol{\Sigma_v}^{-1} \boldsymbol{V}, \tag{106}$$

$$\boldsymbol{\Sigma_x} = \boldsymbol{\Sigma}_0 - \boldsymbol{\Sigma}_0 \boldsymbol{\Phi}^T \boldsymbol{\Sigma_v}^{-1} \boldsymbol{\Phi\Sigma}_0, \tag{107}$$

$$\lambda = \frac{1}{Nh}\left(\|\boldsymbol{V} - \boldsymbol{\Phi\mu_x}\|_2^2 + \sum_{i=1}^{g} tr\left(\boldsymbol{\Sigma_x}^i \boldsymbol{\Phi}_i^T \boldsymbol{\Phi}_i\right)\right), \tag{108}$$

$$\gamma_i^{\kappa+1} = \gamma_i^{\kappa} \cdot \frac{\left\|\sqrt{\boldsymbol{B}_i}\boldsymbol{\Phi}_i^T \boldsymbol{\Sigma_v}^{-1} \boldsymbol{V}\right\|_2}{\sqrt{tr\left(\boldsymbol{\Phi}_i^T \boldsymbol{\Sigma_v}^{-1} \boldsymbol{\Phi}_i \boldsymbol{B}_i\right)}}. \tag{109}$$

To prevent overfitting, [43], each block matrix $\boldsymbol{B}_i$ is updated using an intermediate one $\tilde{\boldsymbol{B}}_i$, with

$$\tilde{\boldsymbol{B}}_i^{\kappa+1} = \tilde{\boldsymbol{B}}_i^{\kappa} + \frac{1}{\gamma_i}\left(\boldsymbol{\Sigma_x}^i + \boldsymbol{\mu_x}^i \left(\boldsymbol{\mu_x}^i\right)^T\right). \tag{110}$$

Then, by introducing

$$\tilde{r}_i = \frac{\overline{diag\left(\tilde{\boldsymbol{B}}_i, 1\right)}}{\overline{diag\left(\tilde{\boldsymbol{B}}_i\right)}} \tag{111}$$

and

$$r_i = sign(\tilde{r}_i) \cdot \min\{|\tilde{r}_i|,\ 0.99\}, \tag{112}$$

$\boldsymbol{B}_i$ can be updated as follows:

$$\boldsymbol{B}_i = \text{Toeplitz}\left(\left[r_i^0, \ldots, r_i^{h-1}\right]\right). \tag{113}$$

The learning process is continued until no significant change in the $\boldsymbol{\mu_x}$ norm occurs.

The conventional SA-SBL approach offers notable improvements in the spatial resolution of EIT images, while the initial choice of hyperparameters does not have a significant impact on it. However, its high complexity ($\mathcal{O}(Nh \cdot gh_s)$), mainly affected by the $\boldsymbol{\gamma}$ learning rule (109), makes it inefficient and impractical in real-time and 3-dimensional imaging applications. Additionally, the slow convergence rate of the EM algorithm, coupled with the need to update the Jacobian matrix $\boldsymbol{J}$ when substantial conductivity changes occur, further exacerbates this issue. Another important drawback of the SA-SBL method is its reliance on pixelized or voxelized domains, limiting its applicability to complex geometries and accurate electrode schemes where the FEM could be more applicable.

Various improvements and advances in SBL have recently been proposed and applied in EIT to address the issues mentioned earlier. In [43], the spatial correlation between neighboring clusters (pattern coupling) was introduced in the hyperparameter learning rule (109) to improve the algorithm's imaging performance. In [44], approximate

message passing (AMP) [194] was used to approximate the EM algorithm's E-step, improving the problem's complexity and convergence rate and enabling its application in 3-dimensional EIT imaging. AMP passes posterior probability density function (PDF) factors $p(V_i|\sum_{j=1}^{g}\mathbf{\Phi}_{i,j}\boldsymbol{x}_j)$ as messages and multiplies them with each $\boldsymbol{x}_i$ within a single-layer network to estimate a set of reliable beliefs $p(\boldsymbol{x}_j)$ [44], [194]. AMP was also adopted in [45], where a multiple measurement vector (MMV) framework exploited temporal correlation between time-sequence imaging frames to apply SA-SBL in td-EIT. In [46], multiple frequency measurement frames were used as data in a multi-task SA-SBL for fd-EIT, achieving sufficient spatial performance in experimental tank cases. Furthermore, [195] combines SA-SBL with a MoM approach presented in [98], evaluated in lung td-EIT, reducing the non-linear effect by using a system matrix derived from a Green function integral equation framework. In addition, [196] introduces a bound-optimization weighted block SBL (WBO-BSBL) approach. The bound-optimization method accelerates the optimization problem by reformulating it in a convex form. Gamma distribution weighting parameters are imposed to incorporate prior knowledge. Moreover, in [197], a 3-layer hierarchical SBL model employing a weighted Laplace prior is applied in lung respiratory monitoring. The K-nearest neighbor (KNN) clustering algorithm is used to adaptively group each disordered conductivity sparse block (finite element) to a reordered distribution. Additionally, in [198], a multi-frame constrained BSBL (MF-BSBL) method used for flexible tactile sensing examines both the sparsity and the intra-frame and inter-frame correlation of the conductivity distribution. Another recent research is found in [199], where an anatomical statistical shape model for lung and torso is established, incorporating patient-specific predictors as the model's hyperparameters with a Gaussian joint prior. The covariance matrix is decomposed into a generic smoothness matrix and a statistical shape model prior matrix. A MAP estimation for the covariance matrix and the conductivity is obtained through linear approximation, differing from the general SA-SBL framework. Finally, in [200], an ROI-shrinkage adaptive BSBL has been proposed for ECT. Adaptive block encoding is exploited in each iteration by filtering and grouping subunits that present high intra-block correlation, enhancing the images' spatial resolution and reducing the reconstruction process complexity.

A demonstration of the qualitative imaging performance of the conventional SA-SBL approach, based on the EM algorithm and the WBO-BSBL one is shown in Fig. 8. Two experimental circular tank saline solution cases with metallic and plastic objects and an in-vivo thoracic case are included. The experimental tank measurement data is provided from the University of Eastern Finland open-source EIT Dataset [201]. The measurements have been captured using the 16-electrode KIT4 EIT system and the adjacent simulation and measurement pattern. Furthermore, the in-vivo voltage measurement data was captured using the 16-electrode EIT instrument described in [202] and is online available in [110].

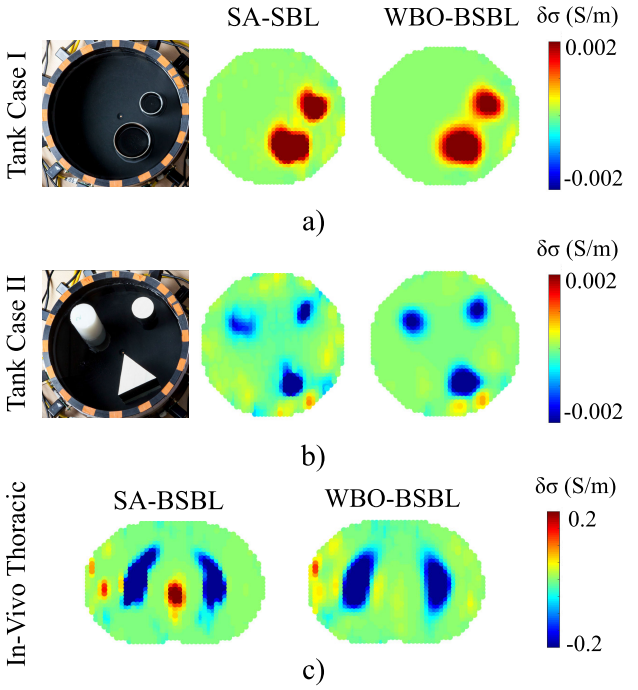

FIGURE 8. Reconstructed EIT images, using EM-based SA-SBL and WBO-BSBL. a) Experimental case with 2 metallic objects in a tank. b) Experimental case with 3 plastic objects in a tank. c) In-vivo thoracic case.

The images capture the lung impedance change due to the breathing process at a healthy human subject. For the image reconstructions that correspond to the experimental cases, a 1225-pixel circular domain is used, while a 1229-pixel thoracic shape domain is used for the in-vivo cases. For all the reconstructions, the clusters' size was uniformly selected as $h_s = 4$, considering the trade-off between complexity and sparsity. The MATLAB code used to reconstruct the images can be found in.[2]

VII. DEEP LEARNING APPROACHES IN EIT

While the concept of neural networks (NNs) has been known for several decades, recent advancements in hardware technology have exponentially enhanced their capabilities in handling complex learning tasks. As a result, NNs have gained widespread adoption in the field of medical imaging to address the challenges associated with inverse image reconstruction problems. In the context of EIT, NNs have emerged as a popular choice for addressing the non-linearity of the inverse problem and effectively incorporating priors to mitigate its ill-conditioned nature. This has contributed to the widespread adoption of NNs in both medical and industrial applications of EIT.

The major drawbacks of EIT imaging performance in traditional and state-of-the-art non-learning schemes are primarily the reduced spatial resolution, sensitivity to signal noise and geometric mismatches and the inability to

[2]https://github.com/chdim100/Weighted-Sparse-Bayesian-Learning-for-Electrical-Impedance-Tomography

accurately reconstruct tissue boundaries. These limitations significantly impact the aforementioned application areas. For example, in lung monitoring, the thoracic and lung shapes may significantly differ between patients and dynamically change over time, eliminating EIT's capability for accurate and reliable image reconstructions [203]. Furthermore, the trade-off between signal noise and imaging frame speed reduces the temporal resolution capability. In geophysical models, on the other hand, there is a lack of a baseline measurement frame that could permit difference-EIT imaging to absorb major modeling errors between the original and the reconstruction models [1]. To address these issues, researchers are attempting to mitigate these challenges with the introduction of more robust DL-based techniques, many of which are focused on specific applications and their unique features [74].

Overall, as in other inverse scattering problems, NN-based learning approaches for EIT can be categorized into three main groups: A) Direct data-based learning, B) post-image reconstruction learning and C) model-based learning [64], [204], [205]. In this section, we provide a concise overview of approaches from the earliest to the most recent, organized based on the mentioned classification. The fundamental learning frameworks are explained. Certain post-image reconstruction and model-based learning approaches have evolved as subsequent stages from fundamental EIT reconstruction methods in the context of deep learning. In such instances, we elucidate the connection between theoretical concepts and contributions.

A. DIRECT DATA BASED LEARNING

This category refers to learning approaches that utilize only the measured voltage data as input information. Most of the earlier NN-based learning schemes applied in EIT actually belong to direct-data based learning ones. The first known work that applied NN for EIT can be found in [48] (Adaline 1994). The Adaline consists of an input layer that includes the normalized differential measurement vector $\boldsymbol{V_n} \in \mathbb{R}^{Nh\times 1}$ and an output layer corresponding to the N_e elements' conductivity values (see also Fig. 9). During the learning process, the Adaline learns a linear relationship between the measurements and the conductivity distribution. In contrast to the perceptron rule, the weights $\boldsymbol{w} \in \mathbb{R}^{Nh\times N_e}$ are updated in an error-proportional manner using the Widrow-Hoff learning rule, without any non-linear activation process. Four years later, in [49], an iterative ANN approach was presented. A number of ANNs equal to the current stimulation patterns has been used. Each one has the corresponding voltage measurement vector as input and a single hidden layer (introducing non-linear activation), while the inputs were iteratively updated with the error between the measured and the computed voltages.

At the same time, two ANN approaches were presented in [50], using a numerically estimated voltage measurement vector and a feed-forward NN based circuit equivalent of

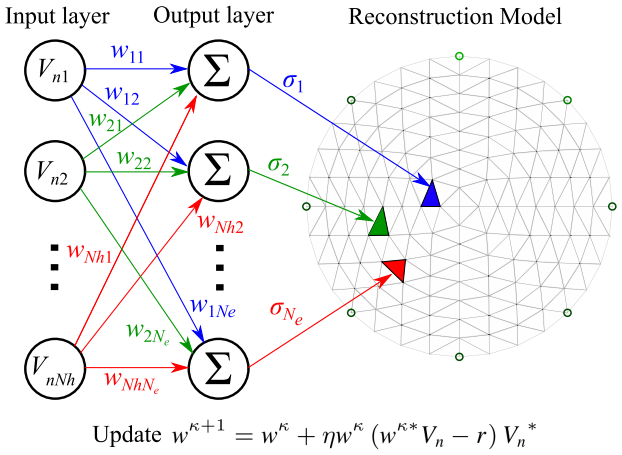

FIGURE 9. Explanatory schematic of the adaline NN for EIT. In the update rule, $\boldsymbol{r} \in \mathbb{R}^{\boldsymbol{N_e}\times 1}$ refers to the label image and η to the learning rate. Each output corresponds to an element.

the FEM mesh, respectively. In [51], the solution of the EIT reconstruction problem was examined through a number of different ANN architectures. Furthermore, in [52], a back-propagation ANN is trained using a modified PSO method (see subsection V-B), in an effort to improve the conventional back-propagation's convergence rate. The utilization of the PSO method to train ANNs with potential vector inputs is also discussed in [47], [53], and [54]. The first study exploits RBF NNs, while the second one involves simulating filtered noisy voltage measurements as inputs and conducts comparisons with iterative Tikhonov and TV regularization using the PD-IPM (see subsection III-E). In [47], a hybrid PSO involving RBF ANNs is proposed, which additionally to the works mentioned, uses simulated annealing to optimize the NN weights. Moreover, in [55], an autoencoder NN approach is proposed for electrical capacitance tomography (ECT), where the encoder and the decoder demonstrate the forward and the inverse problem, respectively. Finally, in [56], a number of 3 single and multiple prediction ANNs were used to reconstruct EIT images from 96 differential voltage measurements. Notably, in the enhanced ANN version, each subsystem was responsible for predicting the conductivity value of a specific element, leading to a simplified training process.

Although the aforementioned direct data-based ANN learning approaches are relatively straightforward to implement, they are associated with significant drawbacks. These include relatively slow convergence speed and limited generalization capabilities across different current injection measurement patterns and setups. Additionally, these approaches often require large measurement datasets, which can be scarce in the context of EIT.

B. POST-IMAGE RECONSTRUCTION LEARNING

As convolutional NNs (CNNs) gained popularity in the medical imaging field, their exceptional feature extraction

capabilities and ability to handle pixel-wise computations have also been recognized in the domain of EIT. Since the late 2010s, there has been a growing number of studies exploring the application of CNNs in EIT, harnessing their potential for image reconstruction and analysis. As a consequence, an individual learning approach has risen in the field of inverse problems and EIT. In particular, an initial estimation of the conductivity distribution is given by a conventional imaging approach. Subsequently, a CNN-based learning process is applied given the roughly reconstructed images and the corresponding ground truth labels to enhance the reconstruction quality, including spatial resolution and the ability to demonstrate sharp organ boundaries.

The first post-image reconstruction learning effort in EIT actually involved RBF ANNs to obtain improved 3D thoracic structures [206] from single-step (linear) Gauss-Newton reconstructed ones. The architecture of the RBF ANNs and the impact of their corresponding hyperparameter selection are described in [207].

One of the earliest applications of CNNs in EIT was the deep D-Bar approach (2018) [58]. In that work, an initial image reconstruction was performed using the D-Bar method, discussed in subsection III-H. Then, a U-Net architecture CNN was trained [208] using a 4096 labeled EIT image dataset for denoising and image segmentation. The deep D-Bar was evaluated on experimental tanks, including plastic and metallic objects forming simple geometry inclusions, as well as inclusions that represent lung injury [58]. Through the reconstructed images, the deep D-Bar approach showcased its potential in EIT image reconstruction and analysis.

The U-Net is a state-of-the-art CNN architecture widely used in medical imaging segmentation. It consists of an encoder and a decoder part, with skip connections exploited to preserve spatial information and alleviate the vanishing gradients issue that occurs in ANNs during the BP process. In Fig. 10, a typical U-Net structure is depicted, processing an image of size $N_e = W \times L$, using N_f features on the first layer, with zero-padded $N_c \times N_c$ convolutional filters, followed by a ReLU activation function and a 2-factor downsampling (max pooling) and upsampling. The number of encoder and decoder layers depends on the image size and the absence of zero-padding would lead to a smaller size output image. The U-Net architecture has been used as a fundamental part in numerous DL EIT inverse solvers, both in post-image processing and model-based learning.

The U-Net-based Beltrami-Net is a modified approach based on the deep D-Bar, presented in [59] for a-EIT. The Beltrami-Net exploits image training data and a Beltrami equation without using any a-priori knowledge of the boundary shape. The method is evaluated on numerous chest-shaped phantoms and is compared to traditional D-Bar and TV regularization. Another early CNN application in EIT is described in [209], where a network consisting of two convolution and pooling stages, followed by two fully-connected (FC) layers, is trained using a large simulated dataset with 10-fold cross-validation. In [210] (2019), a simple cascaded encoder-decoder CNN structure was used to process the reshaped measurement vector as a matrix-image (also called electrical impedance or voltage feature map-VFM), resulting in sufficient quality images. Although [209] and [210] use CNNs, the corresponding learning approaches could also be classified as direct-data learning (see subsection VII-A), as they both actually feed the CNNs with measurement data in an array image form.

In [211], a U-Net CNN driven by a measurement input vector FC layer reconstructs EIT images for cell culture and drug monitoring using a micro-electrode sensor. The FC layer derives a linear naive image reconstruction that is then fed to the U-Net CNN for further processing. In addition, the BE-SOM approach (see subsection III-I) is employed in [60] to derive EIT images using the dominant induced contrast current components. These images serve as inputs to a U-Net CNN structure, effectively learning the non-linear mapping between the inputs and the ground truth images. A comparative study involving the deep D-Bar, a simple LeNet CNN implementation, an FC-Unet implementation, a sparsity regularization method and the conventional D-Bar method under quantitative benchmarks is detailed in [75]. Various numerical examples demonstrate that CNN-based techniques perform better in low measurement noise cases, while sparsity regularization, despite its lower spatial resolution, appears to be more noise-robust. However, it is remarked that the performance of CNN-based techniques is strongly affected by the training data and parameters.

In [212], a 33-layer V Dense Net (VD-Net) architecture is proposed for electrical resistance tomography (ERT), inspired by the U-Net. The reconstruction process involves 5 fully-connected (FC) layers that generate an initial image, which is then used as input for the VD-Net. The VD-Net structure is comprised of 4 dense blocks responsible for feature extraction and deep imaging. Each dense block includes downsampling (encoder part) or upsampling (decoder part) along with 2D convolutional layers. Furthermore, a skip "residual" connection is established from the FC-layer to the VD-Net output. The dense connections in the VD-Net architecture further contribute to the improvement of vanishing gradients, non-linearity and imaging sparsity, compared to the state-of-the-art U-Net.

Finally, in [213], a V^2A-Net (attention-based deep CNN) framework is developed. The first step of the reconstruction process flow includes an initial image estimation according to (30) with a sigmoid function activation, where the hyperparameter and the regularization scheme are trainable. The initial image is fed to a backbone V^2A-Net, comprised of 2 V-shaped similar structure modules: the encoder and the decoder. Squeeze-and-excitation (SE) and coordinate-spatial attention skip connections are established between the 2 modules, resulting in a channel and a position attention tensor, respectively. The SE contributes to obtaining the conductivity distribution, while the coordinate-spatial attention loops enhance the shape information. As a result, the V^2A-Net

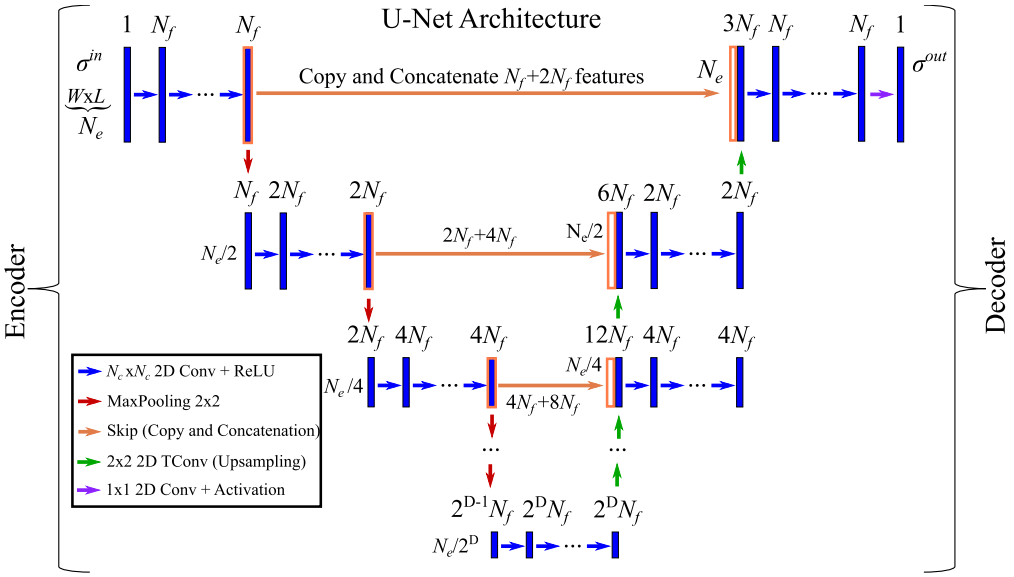

FIGURE 10. Demonstration of a general U-Net CNN architecture, including the encoding, the decoding and the skip functions. Zero-padding for the 2D convolution filters and 2-factor max pooling and upsampling are shown.

presented better inclusion boundary shape preservation in the EIT images, with a more accurate estimation of even low impedance perturbations and significantly reduced complexity, compared to dense CNN and U-Net type architectures. Therefore, the V^{2}A-Net showed improvement both in spatial and temporal imaging performance.

C. MODEL-BASED LEARNING

In this learning category, in addition to measurement data and roughly reconstructed EIT images, the DL structure incorporates physics-related information, such as the forward model [64], [214], [215]. This information may encompass specific geometry or electrode structures, the electric field, or voltage distribution. The described integration ensures that the reconstructed images remain consistent with the measurement data, thereby enhancing the DL approach's generalization capabilities.

One of the first model-based learning applications in EIT was proposed in [61] (2019). This work is an extension of the BE-SOM method and the dominant currents approach [60]. Instead of the U-Net based post-processing of the dominant current-derived images performed in [60] and [61] exploits a cascaded end-to-end CNN, where the dominant currents $\bar{\boldsymbol{J}}_d^{det}$ and the electric fields $\bar{\boldsymbol{E}}_d^t$ (a-priori derived from (47), (49) and (50), details are provided in III-I) are used as inputs. The proposed architecture consists of a number of S stages that regress the currents $\bar{\boldsymbol{J}}_d$ from the corresponding dominant ones $\bar{\boldsymbol{J}}_d^{det}$ in the following way:

$$\bar{\boldsymbol{J}}_d^{ls} = \bar{\bar{\boldsymbol{F}}} \left\{ \bar{\bar{\boldsymbol{M}}}_s \left[\bar{\bar{\boldsymbol{F}}}^* \left(\bar{\boldsymbol{J}}_d - \bar{\boldsymbol{J}}_d^{det} \right) \right] \right\} + \bar{\boldsymbol{J}}_d^{det}, \tag{114}$$

where $\bar{\boldsymbol{J}}_d^{ls} \in \mathbb{R}^{2N_e \times 1}$ is the current label and $\bar{\bar{\boldsymbol{M}}}_s \in \mathbb{R}^{k_s \times k_s}$ is a block-diagonal matrix that denotes the k_s-component

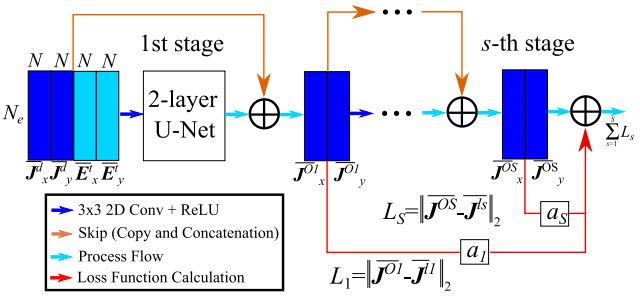

FIGURE 11. Simplified representation of the cascaded end-to-end CNN architecture used in [61].

low-frequency mask (for the rest of notations see III-I). At each stage s, a least square loss function is evaluated for the current labels. Then, a weighted linear combination of them is used as the final loss function. The output estimated currents $\bar{\boldsymbol{J}}_d^o$ are used to compute the conductivity through the polarization tensor $\boldsymbol{\xi}$. The aforementioned induced currents learning scheme has been demonstrated to outperform both the BE-SOM and the dominant current scheme in preserving the shape of inclusions, a crucial aspect for lung imaging applications [61]. A visual demonstration of this process is shown in Fig. 11.

A year later (2020), a Landweber-based DL approach was proposed in [216] for resistive tomography. The Landweber iterative reconstruction network (LIRN) consists of several layers, with the measurements, the Jacobian matrix and a naive EIT reconstruction image as inputs. Each layer consists of A) an FC-Net that "learns" the relaxation vector $\boldsymbol{\alpha} \in \mathbb{R}^{1 \times N_e}$ through the operation $\boldsymbol{\alpha}^\kappa \boldsymbol{J}^T (\boldsymbol{J}\boldsymbol{\sigma}^{\kappa-1} - \boldsymbol{V})$ (κ-th layer, see also (31)) followed by batch normalization and B) a 4-layer CNN, where the first 2 layers perform feature extraction

and the last 2 layers perform image reconstruction. The outputs of the two subnets are subtracted from the previous LIRN layer output to estimate $\boldsymbol{\sigma}^{\kappa}$, which serves as input to the next layer. The LIRN framework was evaluated using a circular phantom tank containing salty water and nylon bars [216]. It exhibited superior performance in cases involving 3 or more inclusions compared to the VD-Net (see the previous subsection). This is attributed to the fact that LIRN reduces its reliance on training data and demonstrates increased robustness to measurement noise.

Another model-based DL approach [217] exploits the VFM concept (see the previous subsection), where a regularization-guided deep imaging framework is developed. In particular, the acquired VFM is fed into a 5-block hierarchical feature extraction structure. Each block integrates a simple l^2-norm regularization network with ReLU activation alongside a CNN (encoder-decoder) that functions as a hybrid regularizer (see also subsection III-F), with their outputs concatenated, followed by a convolutional stage with batch normalization and max pooling. The final block's output is directed to a 2 FC layer network for the reconstruction of the final image. Experimental validation on phantoms showcased that the incorporation of high-level a-priori information aids in extracting spatial information that often remains unattainable through traditional or direct-data learning EIT reconstruction methods.

The FISTA-Net was proposed in [215] as a CNN-based framework for medical imaging inverse problems. Its overall architecture consists of multiple cascaded stages, with each one including a gradient descent and a proximal mapping module. Within each stage, a 2-step update is performed. The FISTA-Net builds upon the FISTA approach (see subsection III-E and [136] for further information), by incorporating the ability to update the gradient matrix during each iteration and to learn non-linear thresholding [215] (see Fig. 12). Evaluation of the FISTA-Net in multi-frequency EIT was conducted in [218] using an in-vitro human breast cancer cell pellet as a case study (24000 training samples). Compared to traditional regularization and the U-Net schemes, the FISTA-Net showed improved quantitative performance metrics in all the test cases.

Another model-based DL approach was developed in [218] and [219], based on the ADMM method (see subsection III-E and [25] for details). In particular, [219] extends [211] to a 3D multifrequency EIT measurement process. The approach uses a U-Net CNN to acquire a group index encoder and ADMM-based group sparsity regularization. This framework is enhanced in [218], where the multiple measurement vector ADMM (MMV-ADMM) network is applied in multifrequency EIT. The MMV-ADMM-Net incorporates a number of cascaded parameter updating blocks, including a gradient descent module, a spatial self-attention module and a convolutional long short-term memory (LSTM) module (see Fig. 13). These modules generalize the shrinkage operator to reveal the correlation between different measurement frequencies. Furthermore, the parameters are shared among

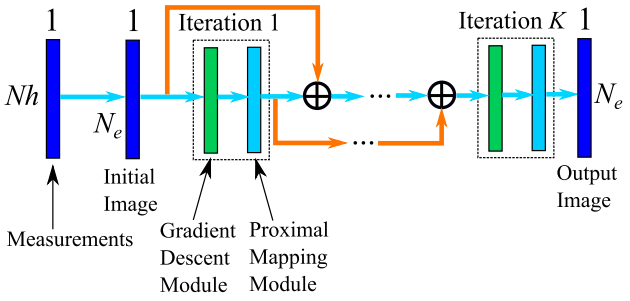

FIGURE 12. Simplified representation of the FISTA-Net architecture [215]. Each iteration step consists of a gradient descent and a proximal mapping module that are implemented using cascaded 2D-convolution filtering and ReLU activation.

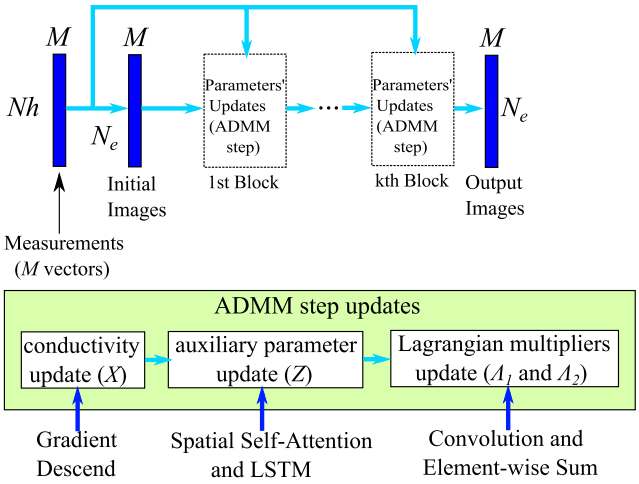

FIGURE 13. Simplified representation of the MMV-ADMM-Net architecture [218]. Each iteration step implements the corresponding ADMM parameter updates.

the update steps and across all the blocks [218]. The MMV-ADMM-Net approach is evaluated on experimental datasets as well as on an in-vitro human chest cancerous cell, resulting in clear images with accurate shapes. Comparison with the traditional ADMM and the FISTA-Net images is also performed, indicating improved quantitative metric values.

In [220], an impedance-optical dual-modal cell imaging approach that utilizes learning-based information fusion is proposed. A microscopic guidance image acquired from an impedance-optical sensor is properly processed to derive a mask image. The mask image and the EIT voltage measurements feed a trained DL model to enhance EIT image reconstruction, called multi-scale feature cross fusion network (MSFCF-Net). The MSFCF-Net includes two backbone networks (BN) [221] that extract latent features from the measurements and the mask image, respectively. Each BN consists of multiple residual blocks that include convolutional filter layers with Leaky ReLU activation [222]. The extracted feature maps from each block are fed to dual-modal feature fusion modules (DMFF) [223] that keep the main spatial information by using efficient convolutional block attention mechanisms [224]. A number of multi-scale

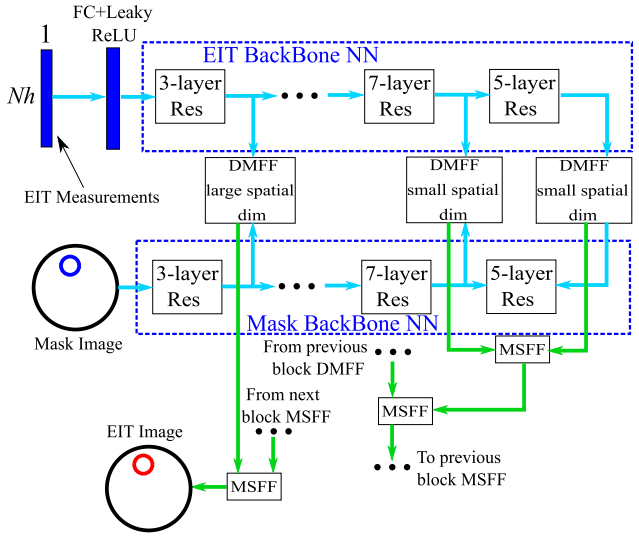

FIGURE 14. Simplified representation of the MSFCF-Net architecture [220].

feature fusion modules (MSFF) integrate the feature maps resulting from the DMFFs to reconstruct the final EIT image. The MSFCF-Net was evaluated on phantoms containing cell spheroids and quantitatively compared with Tikhonov regularization, SA-SBL (see section VI) and FC-Unet. It was shown to outperform them under various inclusion cases and noise levels after 90 epochs of training over approximately 31000 samples. Its high-level architecture is demonstrated in Fig. 14.

Furthermore, in [225], a structure-aware dual-branch (SADB) network for 3D cell imaging was developed. The SADB-Net is comprised of an FC-UNet (see subsection VII-B and [211]) for binary mask generation and two feature extractors that are fed from the voltage measurements and the binary mask, respectively, followed by 2 fully-connected layers to reconstruct the EIT images. Each feature extractor is composed of convolution filter stages followed by batch normalization layers with ReLU activation and a max-pooling layer at their output. As in [220], this approach utilizes two branches to separate the absolute conductivity value and shape estimation, respectively, fusing the feature information to produce high spatial resolution and accurate EIT cell images. However, while [220] is a dual-modal approach exploiting both EIT and microscopy, [225] generates the structural mask using only EIT measurements. Finally, the SADB-Net was compared with Tikhonov and TV regularization, SA-SBL and the FC-Unet scheme, showing improved relative image error and imaging speed [225].

Graph neural networks (GNNs) have recently been introduced in the field of inverse scattering problems, proving to be a valuable tool. In particular, unlike conventional CNNs, GNNs can be tailored to address problems in which the discretization of the reconstruction domain is non-uniform, such as those involving finite element method (FEM) discretization, without the need for interpolation and embeddings. They can be classified into recurrent GNNs, convolutional GNNs, graph autoencoders and spatial-temporal GNNs [226].

GNNs rely on a graph representation of a discretized domain, where $\boldsymbol{\mathcal{A}} \in \mathbb{R}^{N_e \times N_e}$ serves as its adjacency matrix, encapsulating weighted relationships between nodes in the graph. By adding the unit matrix to the adjacency one, the matrix $\tilde{\boldsymbol{\mathcal{A}}} = \boldsymbol{\mathcal{A}} + \boldsymbol{I}$ is derived. The diagonal degree matrix $\tilde{\boldsymbol{D}} \in \mathbb{R}^{N_e \times N_e}$ is also completed as $\tilde{D}_{ii} = \sum_{j=1}^{N_e} \tilde{\mathcal{A}}_{ij}$. According to the Kipf and Welling formula, which is commonly used in convolutional GNNs, each layer can be derived as follows [227]:

$$\boldsymbol{X}^{i+1} = g\left(\tilde{\boldsymbol{D}}^{-\frac{1}{2}}\tilde{\boldsymbol{\mathcal{A}}}\tilde{\boldsymbol{D}}^{-\frac{1}{2}}\boldsymbol{X}^{i}\boldsymbol{W}^{i}\right), \tag{115}$$

where $\boldsymbol{X}^i \in \mathbb{R}^{N_e \times N_{fi}}$ and $\boldsymbol{X}^{i+1} \in \mathbb{R}^{N_e \times N_{f(i+1)}}$ denote the input features of the i-th and $i+1$-th layers respectively, N_{fi} the number of features at the i-th layer, $\boldsymbol{W}^i \in \mathbb{R}^{N_{f(i-1)} \times N_{fi}}$ a matrix that contains the weights of the i-th layer and g a non-linear activation function. The expression $\tilde{\boldsymbol{D}}^{-\frac{1}{2}}\tilde{\boldsymbol{\mathcal{A}}}\tilde{\boldsymbol{D}}^{-\frac{1}{2}}$ represents a graph filter.

GNNs are applied in model-based DL for non-linear inverse problems, including EIT. In the work presented in [64], a convolutional GNN architecture based on a Newton-type method was employed for absolute EIT. This approach utilized a 10 kHz current signal alongside a trigonometric current pattern. The experimental investigations were carried out using phantom tank data acquired via the ACT3 [228] and KIT4 [229] EIT systems. Notably, the results demonstrated significant enhancements in spatial resolution and shape detection in comparison to both the Levenberg-Marquardt and TV methods. Similar improvements were observed in comparison to the residual-based GNN (GResNet) [230]. In Fig. 15, a simplified representation of the architectures of the GNNs, including the GCNM and GResNet, adapted for EIT is presented. Both architectures are fed with a reconstructed EIT image obtained using a naive GN approach. However, in the GCNM, each update is performed through a particularly trained graph convolutional block, considering $\boldsymbol{\mathcal{A}}$ and following the concatenation of the background conductivity $\boldsymbol{\sigma_\kappa}$ and conductivity perturbation $\boldsymbol{\delta\sigma_\kappa}$. On the other hand, within the GResNet architecture, each graph convolutional block takes the previously updated conductivity as input, which is concatenated with the output of the corresponding block. Notably, the graph convolutional block structure is consistent across both architectures, with each layer following the formulation as given by (115).

An application of GNNs in multifrequency cell imaging EIT can be found in [63]. This particular framework employs a combination of a raw EIT image alongside a binary mask as inputs, employed collectively to guide the ultimate reconstruction process. The core architecture of the GNN is composed of several blocks, each of which comprises a graph convolutional component as well as a gated temporal resolution phase. The latter makes use of two parallel dilated convolution layers [231]. This design permits

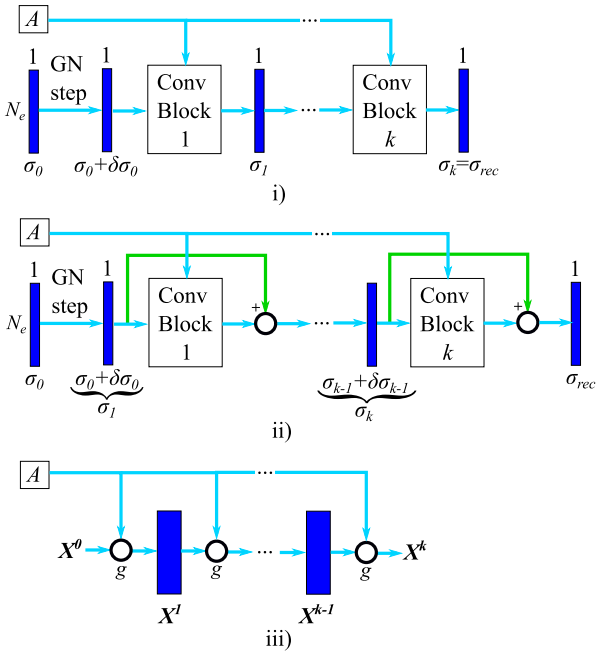

FIGURE 15. Basic convolutional GNN architectures. i) GCNM. ii) GResNet. iii) Convolutional block, same for GCNM, GResNet.

effective learning of both spatial and frequency correlations, thereby enhancing the model's imaging performance. The aforementioned framework was tested on the Edinburgh mfEIT dataset [218] and compared to the MMV-ADMM-Net one, outperforming it under various measurement noise levels. The GNNs were also exploited to extend the U-Net framework, by integrating K-means cluster pooling and clone cluster unpooling instead of the traditional CNN max-pooling process [232]. For a more comprehensive insight into the utilization of GNNs in various biomedical imaging applications, an extensive review is available in [233].

Notwithstanding the considerable strides witnessed in the domain of DL methodologies applied to EIT, the absence of extensive medical EIT datasets gives rise to significant challenges in the implementation of the training process. In response to this issue, the concept of DIP was introduced in [66] to tackle image reconstruction dilemmas. DIP offers a solution to the corresponding inverse problems without the necessity of extensive training data. Rather than training a given NN with measurement data, the optimization of its parameters is achieved through inherent back-propagation mechanisms.

DIP was applied in EIT simulation and experimental data in [65]. A random noise pixelized image input $\boldsymbol{z} \in \mathbb{R}^{W\times L}$ is set, while imposing $\boldsymbol{x} = f_\theta(\boldsymbol{z})$ (f_θ a given NN with weights $\boldsymbol{\theta}$). Then, the denoised pixelized image $\boldsymbol{x} \in \mathbb{R}^{W\times L}$ is mapped to a finite element discretized domain in order to obtain the conductivity: $\boldsymbol{\sigma} = P(\boldsymbol{x}), \boldsymbol{\sigma} \in \mathbb{R}^{N_e\times 1}$. Therefore, the following optimization problem is defined:

$$F(\boldsymbol{\theta}) = \|\boldsymbol{U}(P(f_\theta(\boldsymbol{z}))) - \boldsymbol{V}\|_2^2, \tag{116}$$

$$\boldsymbol{\theta}_* = \underset{\boldsymbol{\theta}\in\mathbb{R}^{N_w}}{\operatorname{argmin}}\Big\{F(\boldsymbol{\theta})\Big\}, \tag{117}$$

where P is the (linear) mapping operator, N_w the total number of the NN's parameters. The process of reconstruction begins with an initial estimation of $\boldsymbol{\sigma}$ and $\boldsymbol{U}$ based on $\boldsymbol{z}$, facilitated through an initially parameterized NN. Subsequently, the cost function F is evaluated and the weights $\boldsymbol{\theta}$ of the NN are iteratively updated using the back-propagation method in conjunction with the Adam optimizer, alongside the updates to $\boldsymbol{\sigma}$. This process is repeated for a predefined number of iterations. In [65], a 5-layer deep U-Net NN architecture was employed, featuring 2 skip connections, LeakyReLU activation in the hidden layers and sigmoid activation at the output layer. A parametric study of the imaging performance with varying the learning rate and the U-Net skip connections was also performed. The preliminary results suggested that DIP can be a promising approach for unsupervised DL EIT image reconstruction; however, it still needs to be evaluated on more experimental and clinical data. The main process flow of the DIP approach is depicted in Fig. 16.

Finally, another untrained NN prior-based approach was developed in [234], where a regularized shallow image prior is proposed for EIT. A 3-layer multi-layer Perceptron (MLP) NN is used along with a TV regularization term for both 2D and 3D EIT on thoracic simulated domains and experimental phantom cases. The results were compared with Laplace regularization scheme combined with untrained MLP, conventional TV and Tikhonov (Laplace prior) regularization, demonstrating major improvements and artifact removal.

Despite significant strides in the integration of EIT and DL, practical applications in real-world scenarios are still hindered by various challenges. A primary challenge lies in the insufficiency of clinical EIT data essential for the training process, a limitation exacerbated by the relatively restricted use of EIT in clinical contexts [65], [74]. Efforts to overcome this challenge have begun, with notable strides made in the research on DIP, as discussed earlier. Another critical concern is the issue of generalization, wherein many approaches are developed and assessed on a constrained set of subject cases, like specific tissue cells or structures, potentially leading to overfitting of network parameters. To address this, it is imperative to leverage properly structured and diverse datasets, employing efficient networks that enhance adaptability to a broader range of scenarios. Additionally, guarding against overfitting through regularization techniques and robust validation on diverse datasets is essential. Furthermore, the potential impact of domain shifts, changes in imaging environments, or equipment variations should be considered to enhance the models' robustness across different medical scenarios. In summary, addressing these challenges will play a pivotal role in the successful transfer of EIT into widespread and effective clinical applications.

VIII. DISCUSSION

EIT has undoubtedly presented significant recent developments in image reconstruction techniques, especially

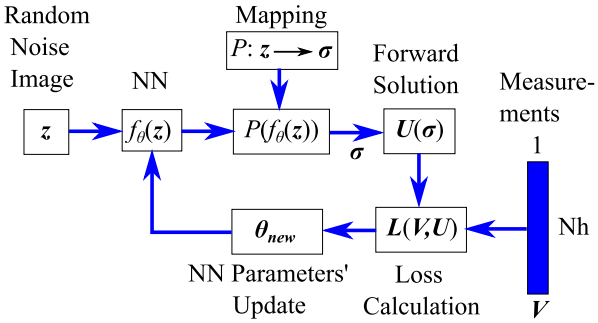

FIGURE 16. Schematic description of the deep image prior for EIT image reconstruction.

since the introduction and incorporation of advanced DL frameworks. However, many considerations have to be made before transferring such developments to the EIT application fields, regarding their feasibility and limitations.

In particular, traditional regularization methods could still be used in simpler anatomical, geophysical, or material structures [127]. Nevertheless, applications that involve more complex-shaped structures or numerous phases of conductivity changes should be treated with frameworks that consider the boundary changes and are robust in preserving the inclusions' shapes under various setup and measurement cases. Although shape-driven non-linear algorithms have demonstrated notable performance in this regard, they could become unstable under different SUT cases, involving many parameters whose initialization might significantly affect the imaging performance [235]. Noise robustness and low speed are also limitations raised by shape-driven approaches, especially in real-time lung and perfusion monitoring. Considering that the real-time lung monitoring trend extends to simultaneously evaluating clinical disorders such as lung recruitment or collapse, derecruitment or overdistention and cardiac function indicators [203], the introduction of deep learning schemes is essential for clinical investigations.

As mentioned in the previous section, the DL frameworks themselves are characterized by a lack of generalization and need a large amount of datasets and computational resources to be properly trained. Therefore, specific DL schemes should be utilized on particular applications, according to their strengths. For example, the fd-EIT based MMV-ADMM-Net [218] and MSFCF-Net [220] frameworks can be applied in ex-vivo cases (biopsies for malignant tissue detection [236]) or material sample investigation. The dense-net (VD-Net and V^2A-Net) and Beltrami-Net frameworks can be transferred to thoracic impedance imaging applications since they demonstrate sufficient performance in boundary shape preservation. The GNNs and DIP, which are still in an early development stage in the context of EIT, are promising frameworks that could be applied in areas with limited open-source measurement data, including geophysical and industrial applications. Finally, further research in the complexity reduction of the reconstruction process is crucial to increase the temporal resolution and the incorporation of 3D schemes in practical aspects of EIT. Both features are proven to provide valuable structural and functional information of the SUT that cannot be detected with common two-dimensional or low frame rate EIT imaging.

IX. CONCLUSION

This paper provides a comprehensive review of both conventional and contemporary approaches to inverse problems in EIT. Each methodology is elucidated with a concise tutorial exposition, covering their fundamental mathematical formulation, algorithmic processes, applicable scenarios and associated strengths and limitations. The categorization of these approaches is based on their mathematical underpinnings, with particular attention directed towards the latest advancements and their significant contributions to the field. In summary, the major challenges posed by the inverse problem in EIT, primarily attributable to the soft field effect and limited data availability, have been effectively addressed through the introduction of advanced image reconstruction methodologies. These approaches are not solely reliant on regression analysis of measurement data; they also capitalize on pertinent information regarding the SUT's structure, the electric fields and the spatial characteristics of the inclusions in terms of their positions and shapes. Consequently, recent advancements in EIT research have yielded significant enhancements in the quality of imaging, encompassing both spatial and temporal dimensions. This progress is paving the way for broader applications of EIT, in both the medical and industrial fields.

REFERENCES

[1] A. Adler and D. Holder, *Electrical Impedance Tomography: Methods, History and Applications*. Boca Raton, FL, USA: CRC Press, 2021.

[2] O. Brabant, B. Crivellari, G. Hosgood, A. Raisis, A. D. Waldmann, U. Auer, A. Adler, L. Smart, M. Laurence, and M. Mosing, "Effects of PEEP on the relationship between tidal volume and total impedance change measured via electrical impedance tomography (EIT)," *J. Clin. Monitor. Comput.*, vol. 36, no. 2, pp. 325–334, Apr. 2022.

[3] M. C. Bachmann, C. Morais, G. Bugedo, A. Bruhn, A. Morales, J. B. Borges, E. Costa, and J. Retamal, "Electrical impedance tomography in acute respiratory distress syndrome," *Crit. Care*, vol. 22, no. 1, pp. 1–11, 2018.

[4] M. Clay and T. C. Ferree, "Weighted regularization in electrical impedance tomography with applications to acute cerebral stroke," *IEEE Trans. Med. Imag.*, vol. 21, no. 6, pp. 629–637, Jun. 2002.

[5] L. Cao, H. Li, D. Fu, X. Liu, H. Ma, C. Xu, X. Dong, B. Yang, and F. Fu, "Real-time imaging of infarction deterioration after ischemic stroke in rats using electrical impedance tomography," *Physiological Meas.*, vol. 41, no. 1, Jan. 2020, Art. no. 015004.

[6] Y. Zou and Z. Guo, "A review of electrical impedance techniques for breast cancer detection," *Med. Eng. Phys.*, vol. 25, no. 2, pp. 79–90, Mar. 2003.

[7] E. K. Murphy, A. Mahara, S. Khan, E. S. Hyams, A. R. Schned, J. Pettus, and R. J. Halter, "Comparative study of separation betweenex vivoprostatic malignant and benign tissue using electrical impedance spectroscopy and electrical impedance tomography," *Physiolog. Meas.*, vol. 38, no. 6, pp. 1242–1261, Jun. 2017.

[8] A. A. Pathiraja, R. A. Weerakkody, A. C. von Roon, P. Ziprin, and R. Bayford, "The clinical application of electrical impedance technology in the detection of malignant neoplasms: A systematic review," *J. Transl. Med.*, vol. 18, no. 1, pp. 1–11, Dec. 2020.

[9] K. Sakai, P. N. Darma, P. A. Sejati, R. Wicaksono, H. Hayashi, and M. Takei, "Gastric functional monitoring by gastric electrical impedance tomography (gEIT) suit with dual-step fuzzy clustering," *Sci. Rep.*, vol. 13, no. 1, p. 514, Jan. 2023.

[10] S. S. Noyori, G. Nakagami, and H. Sanada, "Non-invasive urine volume estimation in the bladder by electrical impedance-based methods: A review," *Med. Eng. Phys.*, vol. 101, Mar. 2022, Art. no. 103748.

[11] T. Rymarczyk, G. Kłosowski, and E. Kozłowski, "A non-destructive system based on electrical tomography and machine learning to analyze the moisture of buildings," *Sensors*, vol. 18, no. 7, p. 2285, Jul. 2018.

[12] R. P. Henderson and J. G. Webster, "An impedance camera for spatially specific measurements of the thorax," *IEEE Trans. Biomed. Eng.*, vol. BME-25, no. 3, pp. 250–254, May 1978.

[13] D. C. Barber and B. H. Brown, "Applied potential tomography," *J. Phys. E, Sci. Instrum.*, vol. 17, no. 9, pp. 723–733, Sep. 1984.

[14] G. H. Golub, P. C. Hansen, and D. P. O'Leary, "Tikhonov regularization and total least squares," *SIAM J. Matrix Anal. Appl.*, vol. 21, no. 1, pp. 185–194, Jan. 1999.

[15] M. Cheney, D. Isaacson, J. C. Newell, S. Simske, and J. Goble, "NOSER: An algorithm for solving the inverse conductivity problem," *Int. J. Imag. Syst. Technol.*, vol. 2, no. 2, pp. 66–75, Jun. 1990.

[16] A. Adler and R. Guardo, "Electrical impedance tomography: Regularized imaging and contrast detection," *IEEE Trans. Med. Imag.*, vol. 15, no. 2, pp. 170–179, Apr. 1996.

[17] M. Vauhkonen, D. Vadasz, P. A. Karjalainen, E. Somersalo, and J. P. Kaipio, "Tikhonov regularization and prior information in electrical impedance tomography," *IEEE Trans. Med. Imag.*, vol. 17, no. 2, pp. 285–293, Apr. 1998.

[18] B. Jin and P. Maass, "An analysis of electrical impedance tomography with applications to Tikhonov regularization," *ESAIM, Control, Optim. Calculus Variat.*, vol. 18, no. 4, pp. 1027–1048, Oct. 2012.

[19] P. Hua, E. J. Woo, J. G. Webster, and W. J. Tompkins, "Iterative reconstruction methods using regularization and optimal current patterns in electrical impedance tomography," *IEEE Trans. Med. Imag.*, vol. 10, no. 4, pp. 621–628, 1991.

[20] N. Polydorides, W. R. B. Lionheart, and H. McCann, "Krylov subspace iterative techniques: On the detection of brain activity with electrical impedance tomography," *IEEE Trans. Med. Imag.*, vol. 21, no. 6, pp. 596–603, Jun. 2002.

[21] J. L. Mueller, D. Isaacson, and J. C. Newell, "A reconstruction algorithm for electrical impedance tomography data collected on rectangular electrode arrays," *IEEE Trans. Biomed. Eng.*, vol. 46, no. 11, pp. 1379–1386, 1999.

[22] P. J. Vauhkonen, M. Vauhkonen, T. Savolainen, and J. P. Kaipio, "Three-dimensional electrical impedance tomography based on the complete electrode model," *IEEE Trans. Biomed. Eng.*, vol. 46, no. 9, pp. 1150–1160, 1999.

[23] A. Borsic, B. M. Graham, A. Adler, and W. R. Lionheart, "Total variation regularization in electrical impedance tomography," Univ. Manchester, Tech. Rep., 2007.

[24] A. Borsic, B. M. Graham, A. Adler, and W. R. B. Lionheart, "In vivo impedance imaging with total variation regularization," *IEEE Trans. Med. Imag.*, vol. 29, no. 1, pp. 44–54, Jan. 2010.

[25] Z. Zhou, G. S. dos Santos, T. Dowrick, J. Avery, Z. Sun, H. Xu, and D. S. Holder, "Comparison of total variation algorithms for electrical impedance tomography," *Physiolog. Meas.*, vol. 36, no. 6, pp. 1193–1209, Jun. 2015.

[26] D. Isaacson, J. L. Mueller, J. C. Newell, and S. Siltanen, "Reconstructions of chest phantoms by the D-bar method for electrical impedance tomography," *IEEE Trans. Med. Imag.*, vol. 23, no. 7, pp. 821–828, Jul. 2004.

[27] K. Knudsen, M. Lassas, J. L. Mueller, and S. Siltanen, "Regularized D-bar method for the inverse conductivity problem," *Inverse Problems Imag.*, vol. 35, no. 4, p. 599, 2009.

[28] J. L. Mueller and S. Siltanen, *Linear and Nonlinear Inverse Problems With Practical Applications*. Philadelphia, PA, USA: SIAM, 2012.

[29] C. N. L. Herrera, M. F. M. Vallejo, J. L. Mueller, and R. G. Lima, "Direct 2-D reconstructions of conductivity and permittivity from EIT data on a human chest," *IEEE Trans. Med. Imag.*, vol. 34, no. 1, pp. 267–274, Jan. 2015.

[30] E. Demidenko, A. Hartov, N. Soni, and K. D. Paulsen, "On optimal current patterns for electrical impedance tomography," *IEEE Trans. Biomed. Eng.*, vol. 52, no. 2, pp. 238–248, Feb. 2005.

[31] A. Adler, J. H. Arnold, R. Bayford, A. Borsic, B. Brown, P. Dixon, T. J. C. Faes, I. Frerichs, H. Gagnon, Y. Gärber, B. Grychtol, G. Hahn, W. R. B. Lionheart, A. Malik, R. P. Patterson, J. Stocks, A. Tizzard, N. Weiler, and G. K. Wolf, "GREIT: A unified approach to 2D linear EIT reconstruction of lung images," *Physiolog. Meas.*, vol. 30, no. 6, p. 35, Jun. 2009.

[32] A. Javaherian, M. Soleimani, K. Moeller, A. Movafeghi, and R. Faghihi, "An accelerated version of alternating direction method of multipliers for TV minimization in EIT," *Appl. Math. Model.*, vol. 40, nos. 21–22, pp. 8985–9000, Nov. 2016.

[33] J. Wang, J. Ma, B. Han, and Q. Li, "Split Bregman iterative algorithm for sparse reconstruction of electrical impedance tomography," *Signal Process.*, vol. 92, no. 12, pp. 2952–2961, Dec. 2012.

[34] F. Li, J. F. P. J. Abascal, M. Desco, and M. Soleimani, "Total variation regularization with split bregman-based method in magnetic induction tomography using experimental data," *IEEE Sensors J.*, vol. 17, no. 4, pp. 976–985, Feb. 2017.

[35] J. Wang, B. Han, and W. Wang, "Elastic-net regularization for nonlinear electrical impedance tomography with a splitting approach," *Applicable Anal.*, vol. 98, no. 12, pp. 2201–2217, Sep. 2019.

[36] S. Osher and J. A. Sethian, "Fronts propagating with curvature-dependent speed: Algorithms based on hamilton-jacobi formulations," *J. Comput. Phys.*, vol. 79, no. 1, pp. 12–49, Nov. 1988.

[37] D. Liu, Y. Zhao, A. K. Khambampati, A. Seppänen, and J. Du, "A parametric level set method for imaging multiphase conductivity using electrical impedance tomography," *IEEE Trans. Comput. Imag.*, vol. 4, no. 4, pp. 552–561, Dec. 2018.

[38] D. Liu, D. Gu, D. Smyl, A. K. Khambampati, J. Deng, and J. Du, "Shape-driven EIT reconstruction using Fourier representations," *IEEE Trans. Med. Imag.*, vol. 40, no. 2, pp. 481–490, Feb. 2021.

[39] D. Liu, A. K. Khambampati, and J. Du, "A parametric level set method for electrical impedance tomography," *IEEE Trans. Med. Imag.*, vol. 37, no. 2, pp. 451–460, Feb. 2018.

[40] R. Olmi, M. Bini, and S. Priori, "A genetic algorithm approach to image reconstruction in electrical impedance tomography," *IEEE Trans. Evol. Comput.*, vol. 4, no. 1, pp. 83–88, Apr. 2000.

[41] Y. Zhang, H. Chen, L. Yang, K. Liu, F. Li, C. Bai, H. Wu, and J. Yao, "A proportional genetic algorithm for image reconstruction of static electrical impedance tomography," *IEEE Sensors J.*, vol. 20, no. 24, pp. 15026–15033, Dec. 2020.

[42] A. R. S. Feitosa, R. R. Ribeiro, V. A. F. Barbosa, R. E. de Souza, and W. P. dos Santos, "Reconstruction of electrical impedance tomography images using particle swarm optimization, genetic algorithms and non-blind search," in *Proc. 5th ISSNIP-IEEE Biosignals Biorobotics Conf., Biosignals Robot. Better Safer Living (BRC)*, May 2014, pp. 1–6.

[43] S. Liu, J. Jia, Y. D. Zhang, and Y. Yang, "Image reconstruction in electrical impedance tomography based on structure-aware sparse Bayesian learning," *IEEE Trans. Med. Imag.*, vol. 37, no. 9, pp. 2090–2102, Sep. 2018.

[44] S. Liu, H. Wu, Y. Huang, Y. Yang, and J. Jia, "Accelerated structure-aware sparse Bayesian learning for three-dimensional electrical impedance tomography," *IEEE Trans. Ind. Informat.*, vol. 15, no. 9, pp. 5033–5041, Sep. 2019.

[45] S. Liu, R. Cao, Y. Huang, T. Ouypornkochagorn, and J. Jia, "Time sequence learning for electrical impedance tomography using Bayesian spatiotemporal priors," *IEEE Trans. Instrum. Meas.*, vol. 69, no. 9, pp. 6045–6057, Sep. 2020.

[46] S. Liu, Y. Huang, H. Wu, C. Tan, and J. Jia, "Efficient multitask structure-aware sparse Bayesian learning for frequency-difference electrical impedance tomography," *IEEE Trans. Ind. Informat.*, vol. 17, no. 1, pp. 463–472, Jan. 2021.

[47] H. Wang, K. Liu, Y. Wu, S. Wang, Z. Zhang, F. Li, and J. Yao, "Image reconstruction for electrical impedance tomography using radial basis function neural network based on hybrid particle swarm optimization algorithm," *IEEE Sensors J.*, vol. 21, no. 2, pp. 1926–1934, Jan. 2021.

[48] A. Adler and R. Guardo, "A neural network image reconstruction technique for electrical impedance tomography," *IEEE Trans. Med. Imag.*, vol. 13, no. 4, pp. 594–600, Dec. 1994.

[49] A. Nejatali and I. R. Ciric, "An iterative algorithm for electrical impedance imaging using neural networks," *IEEE Trans. Magn.*, vol. 34, no. 5, pp. 2940–2943, Sep. 1998.

[50] E. Ratajewicz-Mikolajczak, G. H. Shirkoohi, and J. Sikora, "Two ANN reconstruction methods for electrical impedance tomography," *IEEE Trans. Magn.*, vol. 34, no. 5, pp. 2964–2967, Sep. 1998.

[51] M. GhasemAzar and B. V. Vahdat, "Error study of EIT inverse problem solution using neural networks," in *Proc. IEEE Int. Symp. Signal Process. Inf. Technol.*, Dec. 2007, pp. 894–899.

[52] P. Wang, L.-L. Xie, and Y.-C. Sun, "Electrical impedance tomography based on BP neural network and improved PSO," in *Proc. Int. Conf. Mach. Learn. Cybern.*, vol. 2, Jul. 2009, pp. 1059–1064.

[53] P. Wang, L. Xie, and Y. Sun, "Application of PSO algorithm and RBF neural network in electrical impedance tomography," in *Proc. 9th Int. Conf. Electron. Meas. Instrum.*, Aug. 2009, p. 517.

[54] S. Martin and C. T. M. Choi, "Nonlinear electrical impedance tomography reconstruction using artificial neural networks and particle swarm optimization," *IEEE Trans. Magn.*, vol. 52, no. 3, pp. 1–4, Mar. 2016.

[55] J. Zheng and L. Peng, "An autoencoder-based image reconstruction for electrical capacitance tomography," *IEEE Sensors J.*, vol. 18, no. 13, pp. 5464–5474, Jul. 2018.

[56] T. Rymarczyk, G. Klosowski, E. Kozlowski, and P. Tchórzewski, "Comparison of selected machine learning algorithms for industrial electrical tomography," *Sensors*, vol. 19, no. 7, p. 1521, Mar. 2019.

[57] D. O. Baguer, J. Leuschner, and M. Schmidt, "Computed tomography reconstruction using deep image prior and learned reconstruction methods," *Inverse Problems*, vol. 36, no. 9, Sep. 2020, Art. no. 094004.

[58] S. J. Hamilton and A. Hauptmann, "Deep D-bar: Real-time electrical impedance tomography imaging with deep neural networks," *IEEE Trans. Med. Imag.*, vol. 37, no. 10, pp. 2367–2377, Oct. 2018.

[59] S. J. Hamilton, A. Hänninen, A. Hauptmann, and V. Kolehmainen, "Beltrami-net: Domain-independent deep D-bar learning for absolute imaging with electrical impedance tomography (a-EIT)," *Physiolog. Meas.*, vol. 40, no. 7, Jul. 2019, Art. no. 074002.

[60] Z. Wei, D. Liu, and X. Chen, "Dominant-current deep learning scheme for electrical impedance tomography," *IEEE Trans. Biomed. Eng.*, vol. 66, no. 9, pp. 2546–2555, Sep. 2019.

[61] Z. Wei and X. Chen, "Induced-current learning method for nonlinear reconstructions in electrical impedance tomography," *IEEE Trans. Med. Imag.*, vol. 39, no. 5, pp. 1326–1334, May 2020.

[62] Y. Wu, B. Chen, K. Liu, C. Zhu, H. Pan, J. Jia, H. Wu, and J. Yao, "Shape reconstruction with multiphase conductivity for electrical impedance tomography using improved convolutional neural network method," *IEEE Sensors J.*, vol. 21, no. 7, pp. 9277–9287, Apr. 2021.

[63] Z. Chen, Z. Liu, L. Ai, S. Zhang, and Y. Yang, "Mask-guided spatial–temporal graph neural network for multifrequency electrical impedance tomography," *IEEE Trans. Instrum. Meas.*, vol. 71, pp. 1–10, 2022.

[64] W. Herzberg, D. B. Rowe, A. Hauptmann, and S. J. Hamilton, "Graph convolutional networks for model-based learning in nonlinear inverse problems," *IEEE Trans. Comput. Imag.*, vol. 7, pp. 1341–1353, 2021.

[65] D. Liu, J. Wang, Q. Shan, D. Smyl, J. Deng, and J. Du, "DeepEIT: Deep image prior enabled electrical impedance tomography," *IEEE Trans. Pattern Anal. Mach. Intell.*, vol. 45, no. 8, pp. 9627–9638, Aug. 2023.

[66] V. Lempitsky, A. Vedaldi, and D. Ulyanov, "Deep image prior," in *Proc. IEEE/CVF Conf. Comput. Vis. Pattern Recognit.*, Jun. 2018, pp. 9446–9454.

[67] L. Borcea, "Electrical impedance tomography," *Inverse Problems*, vol. 18, no. 6, p. 99, 2002.

[68] W. R. B. Lionheart, "EIT reconstruction algorithms: Pitfalls, challenges and recent developments," *Physiolog. Meas.*, vol. 25, no. 1, pp. 125–142, Feb. 2004.

[69] A. Adler and A. Boyle, "Electrical impedance tomography: Tissue properties to image measures," *IEEE Trans. Biomed. Eng.*, vol. 64, no. 11, pp. 2494–2504, Nov. 2017.

[70] T. A. Khan and S. H. Ling, "Review on electrical impedance tomography: Artificial intelligence methods and its applications," *Algorithms*, vol. 12, no. 5, p. 88, Apr. 2019.

[71] Y. Fan and L. Ying, "Solving electrical impedance tomography with deep learning," *J. Comput. Phys.*, vol. 404, Mar. 2020, Art. no. 109119.

[72] X. Chen, Z. Wei, M. Li, and P. Rocca, "A review of deep learning approaches for inverse scattering problems (invited review)," *Prog. Electromagn. Res.*, vol. 167, pp. 67–81, 2020.

[73] M. Li, R. Guo, K. Zhang, Z. Lin, F. Yang, S. Xu, X. Chen, A. Massa, and A. Abubakar, "Machine learning in electromagnetics with applications to biomedical imaging: A review," *IEEE Antennas Propag. Mag.*, vol. 63, no. 3, pp. 39–51, Jun. 2021.

[74] T. Zhang, X. Tian, X. Liu, J. Ye, F. Fu, X. Shi, R. Liu, and C. Xu, "Advances of deep learning in electrical impedance tomography image reconstruction," *Frontiers Bioeng. Biotechnol.*, vol. 10, Dec. 2022, Art. no. 1019531.

[75] D. N. Tanyu, J. Ning, A. Hauptmann, B. Jin, and P. Maass, "Electrical impedance tomography: A fair comparative study on deep learning and analytic-based approaches," 2023, *arXiv:2310.18636*.

[76] M. Hanke, B. Harrach, and N. Hyvönen, "Justification of point electrode models in electrical impedance tomography," *Math. Models Methods Appl. Sci.*, vol. 21, no. 6, pp. 1395–1413, Jun. 2011.

[77] K.-S. Cheng, D. Isaacson, J. C. Newell, and D. G. Gisser, "Electrode models for electric current computed tomography," *IEEE Trans. Biomed. Eng.*, vol. 36, no. 9, pp. 918–924, Sep. 1989.

[78] M. M. Ney, "Method of moments as applied to electromagnetic problems," *IEEE Trans. Microw. Theory Techn.*, vol. MTT-33, no. 10, pp. 972–980, Oct. 1985.

[79] W. C. Gibson, *The Method of Moments in Electromagnetics*. Boca Raton, FL, USA: CRC Press, 2021.

[80] F. M. Aliabadi, "Boundary element methods," in *Encyclopedia of Continuum Mechanics*. Berlin, Germany: Springer, 2020, pp. 182–193.

[81] K.-S. Cheng, S. J. Simske, D. Isaacson, J. C. Newell, and D. G. Gisser, "Errors due to measuring voltage on current-carrying electrodes in electric current computed tomography," *IEEE Trans. Biomed. Eng.*, vol. 37, no. 1, pp. 60–65, Jan. 1990.

[82] F. Simini and P. Bertemes-Filho, *Bioimpedance in Biomedical Applications and Research*. Berlin, Germany: Springer, 2018.

[83] J. Xu and Z. Hong, "Low power bio-impedance sensor interfaces: Review and electronics design methodology," *IEEE Rev. Biomed. Eng.*, vol. 15, pp. 23–35, 2022.

[84] V. Alimisis, C. Dimas, G. Pappas, and P. P. Sotiriadis, "Analog realization of fractional-order skin-electrode model for tetrapolar bio-impedance measurements," *Technologies*, vol. 8, no. 4, p. 61, Nov. 2020.

[85] P. Kassanos, "Bioimpedance sensors: A tutorial," *IEEE Sensors J.*, vol. 21, no. 20, pp. 22190–22219, Oct. 2021.

[86] V. Kolehmainen, M. Vauhkonen, P. A. Karjalainen, and J. P. Kaipio, "Assessment of errors in static electrical impedance tomography with adjacent and trigonometric current patterns," *Physiological Meas.*, vol. 18, no. 4, pp. 289–303, Nov. 1997.

[87] D. Isaacson, "Distinguishability of conductivities by electric current computed tomography," *IEEE Trans. Med. Imag.*, vol. MI-5, no. 2, pp. 91–95, Jun. 1986.

[88] D. C. Barber, B. H. Brown, and I. L. Freeston, "Imaging spatial distributions of resistivity using applied potential tomography—APT," in *Information Processing in Medical Imaging*. Berlin, Germany: Springer, 1984, pp. 446–462.

[89] M. Cheney, D. Isaacson, and J. C. Newell, "Electrical impedance tomography," *SIAM Rev.*, vol. 41, no. 1, pp. 85–101, 1999.

[90] T. K. Bera and J. Nagaraju, "Studying the resistivity imaging of chicken tissue phantoms with different current patterns in electrical impedance tomography (EIT)," *Measurement*, vol. 45, no. 4, pp. 663–682, May 2012.

[91] O. L. Silva, R. G. Lima, T. C. Martins, F. S. de Moura, R. S. Tavares, and M. S. G. Tsuzuki, "Influence of current injection pattern and electric potential measurement strategies in electrical impedance tomography," *Control Eng. Pract.*, vol. 58, pp. 276–286, Jan. 2017.

[92] S. C. Jun, J. Kuen, J. Lee, E. J. Woo, D. Holder, and J. K. Seo, "Frequency-difference EIT (fdEIT) using weighted difference and equivalent homogeneous admittivity: Validation by simulation and tank experiment," *Physiolog. Meas.*, vol. 30, no. 10, pp. 1087–1099, Oct. 2009.

[93] J. Jang and J. K. Seo, "Detection of admittivity anomaly on high-contrast heterogeneous backgrounds using frequency difference EIT," *Physiolog. Meas.*, vol. 36, no. 6, pp. 1179–1192, Jun. 2015.

[94] J. K. Seo, J. Lee, S. W. Kim, H. Zribi, and E. J. Woo, "Frequency-difference electrical impedance tomography (fdEIT): Algorithm development and feasibility study," *Physiolog. Meas.*, vol. 29, no. 8, pp. 929–944, Aug. 2008.

[95] C. Wu and M. Soleimani, "Frequency difference EIT with localization: A potential medical imaging tool during cancer treatment," *IEEE Access*, vol. 7, pp. 21870–21878, 2019.

[96] R. Duraiswami, G. L. Chahine, and K. Sarkar, "Boundary element techniques for efficient 2-D and 3-D electrical impedance tomography," *Chem. Eng. Sci.*, vol. 52, no. 13, pp. 2185–2196, Jul. 1997.

[97] Y. Xu, F. Dong, and C. Tan, "Electrical resistance tomography for locating inclusions using analytical boundary element integrals and their partial derivatives," *Eng. Anal. Boundary Elements*, vol. 34, no. 10, pp. 876–883, Oct. 2010.

[98] C. Dimas, N. Uzunoglu, and P. P. Sotiriadis, "An efficient point-matching method-of-moments for 2D and 3D electrical impedance tomography using radial basis functions," *IEEE Trans. Biomed. Eng.*, vol. 69, no. 2, pp. 783–794, Feb. 2022.

[99] K. W. Morton and D. F. Mayers, *Numerical Solution of Partial Differential Equations: An Introduction*. Cambridge, U.K.: Cambridge Univ. Press, 2005.

[100] J.-C. Loiseau and S. L. Brunton, "Constrained sparse Galerkin regression," *J. Fluid Mech.*, vol. 838, pp. 42–67, Mar. 2018.

[101] W. A. Luxemburg, *Riesz Spaces*. Amsterdam, The Netherlands: Elsevier, 2000.

[102] E. J. Woo, P. Hua, J. G. Webster, and W. J. Tompkins, "Finite-element method in electrical impedance tomography," *Med. Biol. Eng. Comput.*, vol. 32, no. 5, pp. 530–536, Sep. 1994.

[103] A. P. Calderón, "On an inverse boundary value problem," *Comput. Appl. Math.*, vol. 25, nos. 2–3, pp. 133–138, 2006.

[104] M. Huska, D. Lazzaro, S. Morigi, A. Samorè, and G. Scrivanti, "Spatially-adaptive variational reconstructions for linear inverse electrical impedance tomography," *J. Sci. Comput.*, vol. 84, no. 3, pp. 1–29, Sep. 2020.

[105] N. Polydorides and W. R. Lionheart, "A MATLAB toolkit for three-dimensional electrical impedance tomography: A contribution to the electrical impedance and diffuse optical reconstruction software project," *Meas. Sci. Technol.*, vol. 13, no. 12, p. 1871, 2002.

[106] M. Hanke, "Iterative regularization techniques in image reconstruction," in *Surveys Solution Methods for Inverse Problems*. New York, NY, USA: Springer, 2000, pp. 35–52.

[107] J. Sylvester and G. Uhlmann, "A global uniqueness theorem for an inverse boundary value problem," *Ann. Math.*, vol. 125, no. 1, pp. 153–169, Jan. 1987.

[108] A. I. Nachman, "Global uniqueness for a two-dimensional inverse boundary value problem," *Ann. Math.*, vol. 143, no. 1, pp. 71–96, 1996.

[109] C. R. Vogel, *Computational Methods for Inverse Problems*. Philadelphia, PA, USA: SIAM, 2002.

[110] A. Adler and W. R. Lionheart, "Uses and abuses of EIDORS: An extensible software base for EIT," *Physiolog. Meas.*, vol. 27, no. 5, p. 25, 2006.

[111] F. Santosa and M. Vogelius, "A backprojection algorithm for electrical impedance imaging," *SIAM J. Appl. Math.*, vol. 50, no. 1, pp. 216–243, Feb. 1990.

[112] S. Wanjun, D. Xiuzhen, F. Feng, Y. Fusheng, L. Xiaodong, and X. Canhua, "Different approaches to the completion of the back-projection algorithm in image monitoring by electrical impedance tomography," in *Proc. IEEE Eng. Med. Biol. 27th Annu. Conf.*, Jan. 2006, pp. 1638–1641.

[113] B. Sun, S. Yue, Z. Cui, and H. Wang, "A new linear back projection algorithm to electrical tomography based on measuring data decomposition," *Meas. Sci. Technol.*, vol. 26, no. 12, 2015, Art. no. 125402.

[114] Z. Wang, S. Yue, and X. Liu, "An iterative linear back-projection algorithm for electrical impedance tomography," in *Proc. 13th World Congr. Intell. Control Autom. (WCICA)*, Jul. 2018, pp. 484–489.

[115] N. Avis and D. Barber, "Image reconstruction using non-adjacent drive configurations (electric impedance tomography)," *Physiolog. Meas.*, vol. 15, no. 2, p. 153, 1994.

[116] P. Xu, "Truncated SVD methods for discrete linear ill-posed problems," *Geophys. J. Int.*, vol. 135, no. 2, pp. 505–514, Nov. 1998.

[117] B. Graham and A. Adler, "Objective selection of hyperparameter for EIT," *Physiolog. Meas.*, vol. 27, no. 5, p. 65, 2006.

[118] N. G. Polson and V. Sokolov, "Bayesian regularization: From Tikhonov to horseshoe," *Wiley Interdiscipl. Rev., Comput. Statist.*, vol. 11, no. 4, p. e1463, 2019.

[119] A. Tarantola, *Inverse Problem Theory and Methods for Model Parameter Estimation*. Philadelphia, PA, USA: SIAM, 2005.

[120] D. W. Marquardt, "An algorithm for least-squares estimation of nonlinear parameters," *J. Soc. Ind. Appl. Math.*, vol. 11, no. 2, pp. 431–441, Jun. 1963.

[121] M. Hanke, A. Neubauer, and O. Scherzer, "A convergence analysis of the Landweber iteration for nonlinear ill-posed problems," *Numerische Math.*, vol. 72, no. 1, pp. 21–37, Nov. 1995.

[122] R. Battiti, "First- and second-order methods for learning: Between steepest descent and Newton's method," *Neural Comput.*, vol. 4, no. 2, pp. 141–166, Mar. 1992.

[123] M. Vauhkonen, P. A. Karjalainen, and J. P. Kaipio, "A Kalman filter approach to track fast impedance changes in electrical impedance tomography," *IEEE Trans. Biomed. Eng.*, vol. 45, no. 4, pp. 486–493, Apr. 1998.

[124] K. Kim, B. Kim, M. Kim, Y. Lee, and M. Vauhkonen, "Image reconstruction in time-varying electrical impedance tomography based on the extended Kalman filter," *Meas. Sci. Technol.*, vol. 12, no. 8, p. 1032, 2001.

[125] F. C. Trigo, R. Gonzalez-Lima, and M. B. P. Amato, "Electrical impedance tomography using the extended Kalman filter," *IEEE Trans. Biomed. Eng.*, vol. 51, no. 1, pp. 72–81, Jan. 2004.

[126] Y. Xu, Y. Pei, and F. Dong, "An adaptive Tikhonov regularization parameter choice method for electrical resistance tomography," *Flow Meas. Instrum.*, vol. 50, pp. 1–12, Aug. 2016.

[127] B. Sun, S. Yue, Z. Hao, Z. Cui, and H. Wang, "An improved Tikhonov regularization method for lung cancer monitoring using electrical impedance tomography," *IEEE Sensors J.*, vol. 19, no. 8, pp. 3049–3057, Apr. 2019.

[128] S. Li, H. Wang, T. Liu, Z. Cui, J. N. Chen, Z. Xia, and Q. Guo, "A fast Tikhonov regularization method based on homotopic mapping for electrical resistance tomography," *Rev. Sci. Instrum.*, vol. 93, no. 4, 2022, Art. no. 043709.

[129] B. S. Kim, A. K. Khambampati, S. Kim, and K. Y. Kim, "Electrical resistance imaging of two-phase flow using direct Landweber method," *Flow Meas. Instrum.*, vol. 41, pp. 41–49, Mar. 2015.

[130] V. Michel, A. Gramfort, G. Varoquaux, E. Eger, and B. Thirion, "Total variation regularization for fMRI-based prediction of behavior," *IEEE Trans. Med. Imag.*, vol. 30, no. 7, pp. 1328–1340, Jul. 2011.

[131] L. Condat, "A direct algorithm for 1-D total variation denoising," *IEEE Signal Process. Lett.*, vol. 20, no. 11, pp. 1054–1057, Nov. 2013.

[132] G. Tong, S. Liu, H. Guo, and H. Chen, "Split Bregman iteration based image reconstruction algorithm for electrical capacitance tomography," *Flow Meas. Instrum.*, vol. 66, pp. 119–127, Apr. 2019.

[133] Q. Wang, F. Li, J. Wang, X. Duan, and X. Li, "Towards a combination of low rank and sparsity in EIT imaging," *IEEE Access*, vol. 7, pp. 156054–156064, 2019.

[134] Q. Wang, J. Wang, X. Li, X. Duan, R. Zhang, H. Zhang, Y. Ma, H. Wang, and J. Jia, "Exploring respiratory motion tracking through electrical impedance tomography," *IEEE Trans. Instrum. Meas.*, vol. 70, pp. 1–12, 2021.

[135] Y. Shi, J. Liao, M. Wang, Y. Li, F. Fu, and M. Soleimani, "Total fractional-order variation regularization based image reconstruction method for capacitively coupled electrical resistance tomography," *Flow Meas. Instrum.*, vol. 82, Dec. 2021, Art. no. 102081.

[136] A. Beck and M. Teboulle, "A fast iterative shrinkage-thresholding algorithm for linear inverse problems," *SIAM J. Imag. Sci.*, vol. 2, no. 1, pp. 183–202, Jan. 2009.

[137] X. Liu, T. Zhang, J. Ye, X. Tian, W. Zhang, B. Yang, M. Dai, C. Xu, and F. Fu, "Fast iterative shrinkage-thresholding algorithm with continuation for brain injury monitoring imaging based on electrical impedance tomography," *Sensors*, vol. 22, no. 24, p. 9934, 2022.

[138] Q. Wang, X. Chen, D. Wang, Z. Wang, X. Zhang, N. Xie, and L. Liu, "Regularization solver guided FISTA for electrical impedance tomography," *Sensors*, vol. 23, no. 4, p. 2233, 2023.

[139] H. Zou and T. Hastie, "Regularization and variable selection via the elastic net," *J. Roy. Stat. Soc. Ser. B, Stat. Methodol.*, vol. 67, no. 2, pp. 301–320, Apr. 2005.

[140] X. Song, Y. Xu, and F. Dong, "A hybrid regularization method combining Tikhonov with total variation for electrical resistance tomography," *Flow Meas. Instrum.*, vol. 46, pp. 268–275, Dec. 2015.

[141] D. Liu, V. Kolehmainen, S. Siltanen, A. M. Laukkanen, and A. Seppanen, "Estimation of conductivity changes in a region of interest with electrical impedance tomography," 2014, *arXiv:1403.6587*.

[142] D. Liu, V. Kolehmainen, S. Siltanen, A.-M. Laukkanen, and A. Seppänen, "Nonlinear difference imaging approach to three-dimensional electrical impedance tomography in the presence of geometric modeling errors," *IEEE Trans. Biomed. Eng.*, vol. 63, no. 9, pp. 1956–1965, Sep. 2016.

[143] X. Liu and Z. Liu, "A novel algorithm based on L_1-L_p norm for inverse problem of electromagnetic tomography," *Flow Meas. Instrum.*, vol. 65, pp. 318–326, 2019.

[144] W. Zhang, C. Tan, Y. Xu, and F. Dong, "Electrical resistance tomography image reconstruction based on modified OMP algorithm," *IEEE Sensors J.*, vol. 19, no. 14, pp. 5723–5731, Jul. 2019.
[145] W. Zhang, C. Tan, and F. Dong, "Non-linear reconstruction for ERT inverse problem based on homotopy algorithm," *IEEE Sensors J.*, vol. 23, no. 10, pp. 10404–10412, May 2023.
[146] A. Adler, M. B. Amato, J. H. Arnold, R. Bayford, M. Bodenstein, S. H. Böhm, B. H. Brown, I. Frerichs, O. Stenqvist, N. Weiler, and G. K. Wolf, "Whither lung EIT: Where are we, where do we want to go and what do we need to get there?" *Physiolog. Meas.*, vol. 33, no. 5, pp. 679–694, May 2012.
[147] B. Grychtol, W. R. B. Lionheart, M. Bodenstein, G. K. Wolf, and A. Adler, "Impact of model shape mismatch on reconstruction quality in electrical impedance tomography," *IEEE Trans. Med. Imag.*, vol. 31, no. 9, pp. 1754–1760, Sep. 2012.
[148] B. Grychtol, B. Müller, and A. Adler, "3D EIT image reconstruction with GREIT," *Physiolog. Meas.*, vol. 37, no. 6, p. 785, 2016.
[149] G. Alessandrini, "Stable determination of conductivity by boundary measurements," *Applicable Anal.*, vol. 27, nos. 1–3, pp. 153–172, 1988.
[150] J. L. Mueller and S. Siltanen, "The D-bar method for electrical impedance tomography—Demystified," *Inverse Problems*, vol. 36, no. 9, Sep. 2020, Art. no. 093001.
[151] E. K. Murphy and J. L. Mueller, "Effect of domain shape modeling and measurement errors on the 2-D D-bar method for EIT," *IEEE Trans. Med. Imag.*, vol. 28, no. 10, pp. 1576–1584, Oct. 2009.
[152] S. J. Hamilton, W. Lionheart, and A. Adler, "Comparing D-bar and common regularization-based methods for electrical impedance tomography," *Physiolog. Meas.*, vol. 40, no. 4, 2019, Art. no. 044004.
[153] J. Rixen, S. Leonhardt, J. Moll, D. H. Nguyen, and C. Ngo, "The D-bar algorithm fusing electrical impedance tomography with a priori radar data: A hands-on analysis," *Algorithms*, vol. 16, no. 1, p. 43, 2023.
[154] G. Uhlmann, "Electrical impedance tomography and Calderón's problem," *Inverse Problems*, vol. 25, no. 12, 2009, Art. no. 123011.
[155] K. Shin and J. L. Mueller, "A second order Calderón's method with a correction term and a priori information," *Inverse Problems*, vol. 36, no. 12, 2020, Art. no. 124005.
[156] S. Cen, B. Jin, K. Shin, and Z. Zhou, "Electrical impedance tomography with deep Calderón method," 2023, *arXiv:2304.09074*.
[157] G. Boverman, T.-J. Kao, D. Isaacson, and G. J. Saulnier, "An implementation of Calderón's method for 3-D limited-view EIT," *IEEE Trans. Med. Imag.*, vol. 28, no. 7, pp. 1073–1082, Jul. 2009.
[158] Z. Cao and L. Xu, "2D image reconstruction of a human chest by using Calderón's method and the adjacent current pattern," *J. Instrum.*, vol. 8, no. 3, 2013, Art. no. P03004.
[159] K. Shin, S. U. Ahmad, and J. L. Mueller, "A three dimensional Calderon-based method for EIT on the cylindrical geometry," *IEEE Trans. Biomed. Eng.*, vol. 68, no. 5, pp. 1487–1495, May 2021.
[160] X. Chen, "Subspace-based optimization method for solving inverse-scattering problems," *IEEE Trans. Geosci. Remote Sens.*, vol. 48, no. 1, pp. 42–49, Jan. 2010.
[161] X.-D. Chen, "Subspace-based optimization method in electric impedance tomography," *J. Electromagn. Waves Appl.*, vol. 23, nos. 11–12, pp. 1397–1406, Jan. 2009.
[162] Y. H. Dai and Y. Yuan, "A nonlinear conjugate gradient method with a strong global convergence property," *SIAM J. Optim.*, vol. 10, no. 1, pp. 177–182, Jan. 1999.
[163] Z. Zong, Y. Wang, S. He, and Z. Wei, "Adaptively regularized bases-expansion subspace optimization methods for electrical impedance tomography," *IEEE Trans. Biomed. Eng.*, vol. 69, no. 10, pp. 3098–3108, Oct. 2022.
[164] P. C. Hansen, "Analysis of discrete ill-posed problems by means of the L-curve," *SIAM Rev.*, vol. 34, no. 4, pp. 561–580, Dec. 1992.
[165] P. C. Hansen, *Rank-Deficient and Discrete Ill-Posed Problems: Numerical Aspects of Linear Inversion*. Philadelphia, PA, USA: SIAM, 1998.
[166] J. B. B. Beckmann, A. Sparks, J. A. Ward-Williams, M. D. Mantle, A. J. Sederman, and L. F. Gladden, "Generalized cross-validation as a method of hyperparameter search for MTGV regularization," 2023, *arXiv:2311.11442*.
[167] E. T. Chung, T. F. Chan, and X.-C. Tai, "Electrical impedance tomography using level set representation and total variational regularization," *J. Comput. Phys.*, vol. 205, no. 1, pp. 357–372, May 2005.
[168] M. Soleimani, W. R. B. Lionheart, and O. Dorn, "Level set reconstruction of conductivity and permittivity from boundary electrical measurements using experimental data," *Inverse Problems Sci. Eng.*, vol. 14, no. 2, pp. 193–210, Mar. 2006.
[169] D. Liu, A. K. Khambampati, S. Kim, and K. Y. Kim, "Multi-phase flow monitoring with electrical impedance tomography using level set based method," *Nucl. Eng. Des.*, vol. 289, pp. 108–116, Aug. 2015.
[170] H.-K. Zhao, T. Chan, B. Merriman, and S. Osher, "A variational level set approach to multiphase motion," *J. Comput. Phys.*, vol. 127, no. 1, pp. 179–195, 1996.
[171] D. Liu, D. Smyl, and J. Du, "A parametric level set-based approach to difference imaging in electrical impedance tomography," *IEEE Trans. Med. Imag.*, vol. 38, no. 1, pp. 145–155, Jan. 2019.
[172] D. Liu and J. Du, "A moving morphable components based shape reconstruction framework for electrical impedance tomography," *IEEE Trans. Med. Imag.*, vol. 38, no. 12, pp. 2937–2948, Dec. 2019.
[173] D. Liu, D. Gu, D. Smyl, J. Deng, and J. Du, "Shape reconstruction using Boolean operations in electrical impedance tomography," *IEEE Trans. Med. Imag.*, vol. 39, no. 9, pp. 2954–2964, Sep. 2020.
[174] D. Liu, D. Gu, D. Smyl, J. Deng, and J. Du, "B-spline level set method for shape reconstruction in electrical impedance tomography," *IEEE Trans. Med. Imag.*, vol. 39, no. 6, pp. 1917–1929, Jun. 2020.
[175] B. Harrach, J. K. Seo, and E. J. Woo, "Factorization method and its physical justification in frequency-difference electrical impedance tomography," *IEEE Trans. Med. Imag.*, vol. 29, no. 11, pp. 1918–1926, Nov. 2010.
[176] N. Chaulet, S. Arridge, T. Betcke, and D. Holder, "The factorization method for three dimensional electrical impedance tomography," *Inverse Problems*, vol. 30, no. 4, 2014, Art. no. 045005.
[177] A. Lechleiter, N. Hyvönen, and H. Hakula, "The factorization method applied to the complete electrode model of impedance tomography," *SIAM J. Appl. Math.*, vol. 68, no. 4, pp. 1097–1121, 2008.
[178] B. Gebauer and N. Hyvönen, "Factorization method and irregular inclusions in electrical impedance tomography," *Inverse Problems*, vol. 23, no. 5, p. 2159, 2007.
[179] B. Harrach, "Recent progress on the factorization method for electrical impedance tomography," *Comput. Math. Methods Med.*, vol. 2013, p. 8, 2013, Art. no. 425184.
[180] B. Harrach and M. Ullrich, "Monotonicity-based shape reconstruction in electrical impedance tomography," *SIAM J. Math. Anal.*, vol. 45, no. 6, pp. 3382–3403, Jan. 2013.
[181] B. Harrach and M. N. Minh, "Monotonicity-based regularization for phantom experiment data in electrical impedance tomography," in *New Trends in Parameter Identification for Mathematical Models*. Cham, Switzerland: Birkhäuser, 2018, pp. 107–120.
[182] L. Zhou, B. Harrach, and J. K. Seo, "Monotonicity-based electrical impedance tomography for lung imaging," *Inverse problems*, vol. 34, no. 4, 2018, Art. no. 045005.
[183] H. Garde, "Comparison of linear and non-linear monotonicity-based shape reconstruction using exact matrix characterizations," *Inverse Problems Sci. Eng.*, vol. 26, no. 1, pp. 33–50, Jan. 2018.
[184] P. R. Arbic II and V. Bukshtynov, "Efficient gradient-based optimization for reconstructing binary images in applications to electrical impedance tomography," 2023, *arXiv:2304.02601*.
[185] P. R. Arbic II and V. Bukshtynov, "Efficient gradient-based optimization for reconstructing binary images in applications to electrical impedance tomography," *Comput. Optim. Appl.*, pp. 1–25, Feb. 2024.
[186] M. Brühl, "Explicit characterization of inclusions in electrical impedance tomography," *SIAM J. Math. Anal.*, vol. 32, no. 6, pp. 1327–1341, 2001.
[187] M. Ikehata, "Enclosing a polygonal cavity in a two-dimensional bounded domain from Cauchy data," *Inverse Problems*, vol. 15, no. 5, p. 1231, 1999.
[188] U. Z. Ijaz, A. K. Khambampati, J. S. Lee, S. Kim, and K. Y. Kim, "Nonstationary phase boundary estimation in electrical impedance tomography using unscented Kalman filter," *J. Comput. Phys.*, vol. 227, no. 15, pp. 7089–7112, 2008.
[189] D. Liu, D. Smyl, and J. Du, "Nonstationary shape estimation in electrical impedance tomography using a parametric level set-based extended Kalman filter approach," *IEEE Trans. Instrum. Meas.*, vol. 69, no. 5, pp. 1894–1907, May 2020.
[190] S. d. P. Pellegrini, F. C. Trigo, and R. Lima, "Adaptive Kalman filter-based information fusion in electrical impedance tomography for a two-phase flow," *Mech. Syst. Signal Process.*, vol. 150, Mar. 2021, Art. no. 107326.
[191] S. Ren, Y. Wang, G. Liang, and F. Dong, "A robust inclusion boundary reconstructor for electrical impedance tomography with geometric constraints," *IEEE Trans. Instrum. Meas.*, vol. 68, no. 3, pp. 762–773, Mar. 2019.

[192] J. Kennedy and R. Eberhart, "Particle swarm optimization," in *Proc. IEEE ICNN*, vol. 4, Nov. 1995, pp. 1942–1948.
[193] Z. Zhang and B. D. Rao, "Extension of SBL algorithms for the recovery of block sparse signals with intra-block correlation," *IEEE Trans. Signal Process.*, vol. 61, no. 8, pp. 2009–2015, Apr. 2013.
[194] M. Bayati and A. Montanari, "The dynamics of message passing on dense graphs, with applications to compressed sensing," *IEEE Trans. Inf. Theory*, vol. 57, no. 2, pp. 764–785, Feb. 2011.
[195] C. Dimas, V. Alimisis, N. Uzunoglu, and P. P. Sotiriadis, "A point-matching method of moment with sparse Bayesian learning applied and evaluated in dynamic lung electrical impedance tomography," *Bioengineering*, vol. 8, no. 12, p. 191, 2021.
[196] C. Dimas, V. Alimisis, and P. P. Sotiriadis, "Electrical impedance tomography using a weighted bound-optimization block sparse Bayesian learning approach," in *Proc. IEEE 22nd Int. Conf. Bioinf. Bioengineering (BIBE)*, Nov. 2022, pp. 243–248.
[197] Y. Wu, B. Chen, K. Liu, S. Huang, Y. Li, J. Jia, and J. Yao, "Bayesian image reconstruction using weighted Laplace prior for lung respiratory monitoring with electrical impedance tomography," *IEEE Trans. Instrum. Meas.*, vol. 72, pp. 1–11, 2023.
[198] G. Ma, H. Chen, P. Wang, and X. Wang, "Multi-frame constrained block sparse Bayesian learning for flexible tactile sensing using electrical impedance tomography," *IEEE Trans. Comput. Imag.*, vol. 8, pp. 438–448, 2022.
[199] M. I. Page, R. Nicholson, M. H. Tawhai, A. R. Clark, and H. Kumar, "Improved electrical impedance tomography reconstruction via a Bayesian approach with an anatomical statistical shape model," *IEEE Trans. Biomed. Eng.*, vol. 70, no. 8, pp. 2486–2495, Aug. 2023.
[200] P. Suo, J. Sun, X. Li, S. Sun, and L. Xu, "Image reconstruction in electrical capacitance tomography using ROI-shrinkage adaptive block sparse Bayesian learning," *IEEE Trans. Instrum. Meas.*, vol. 72, pp. 1–9, 2023.
[201] A. Hauptmann, V. Kolehmainen, N. M. Mach, T. Savolainen, A. Seppänen, and S. Siltanen, "Open 2D electrical impedance tomography data archive," 2017, *arXiv:1704.01178*.
[202] R. Guardo, C. Boulay, G. Savoie, and A. Adier, "A superheterodyne serial data acquisition system for electrical impedance tomography," in *Proc. 15th Annu. Int. Conf. IEEE Eng. Med. Biol. Societ*, Mar. 1993, pp. 86–87.
[203] V. Tomicic and R. Cornejo, "Lung monitoring with electrical impedance tomography: Technical considerations and clinical applications," *J. Thoracic Disease*, vol. 11, no. 7, pp. 3122–3135, Jul. 2019.
[204] S. Arridge, P. Maass, O. Öktem, and C.-B. Schönlieb, "Solving inverse problems using data-driven models," *Acta Numerica*, vol. 28, pp. 1–174, May 2019.
[205] G. Ongie, A. Jalal, C. A. Metzler, R. G. Baraniuk, A. G. Dimakis, and R. Willett, "Deep learning techniques for inverse problems in imaging," *IEEE J. Sel. Areas Inf. Theory*, vol. 1, no. 1, pp. 39–56, May 2020.
[206] S. Martin and C. T. M. Choi, "A post-processing method for three-dimensional electrical impedance tomography," *Sci. Rep.*, vol. 7, no. 1, p. 7212, Aug. 2017.
[207] S. Martin and C. T. M. Choi, "On the influence of spread constant in radial basis networks for electrical impedance tomography," *Physiolog. Meas.*, vol. 37, no. 6, p. 801, 2016.
[208] E. Shelhamer, J. Long, and T. Darrell, "Fully convolutional networks for semantic segmentation," *IEEE Trans. Pattern Anal. Mach. Intell.*, vol. 39, no. 4, pp. 640–651, Apr. 2017.
[209] C. Tan, S. Lv, F. Dong, and M. Takei, "Image reconstruction based on convolutional neural network for electrical resistance tomography," *IEEE Sensors J.*, vol. 19, no. 1, pp. 196–204, Jan. 2019.
[210] D. Hu, K. Lu, and Y. Yang, "Image reconstruction for electrical impedance tomography based on spatial invariant feature maps and convolutional neural network," in *Proc. IEEE Int. Conf. Imag. Syst. Techn. (IST)*, Dec. 2019, pp. 1–6.
[211] Z. Chen, Y. Yang, J. Jia, and P. Bagnaninchi, "Deep learning based cell imaging with electrical impedance tomography," in *Proc. IEEE Int. Instrum. Meas. Technol. Conf. (IMTC)*, May 2020, pp. 1–6.
[212] F. Li, C. Tan, and F. Dong, "Electrical resistance tomography image reconstruction with densely connected convolutional neural network," *IEEE Trans. Instrum. Meas.*, vol. 70, pp. 1–11, 2021.
[213] Z. Wang, X. Zhang, R. Fu, D. Wang, X. Chen, and H. Wang, "Electrical impedance tomography image reconstruction with attention-based deep convolutional neural network," *IEEE Trans. Instrum. Meas.*, vol. 72, pp. 1–18, 2023.
[214] H. K. Aggarwal, M. P. Mani, and M. Jacob, "MoDL: Model-based deep learning architecture for inverse problems," *IEEE Trans. Med. Imag.*, vol. 38, no. 2, pp. 394–405, Feb. 2019.
[215] J. Xiang, Y. Dong, and Y. Yang, "FISTA-net: Learning a fast iterative shrinkage thresholding network for inverse problems in imaging," *IEEE Trans. Med. Imag.*, vol. 40, no. 5, pp. 1329–1339, May 2021.
[216] F. Li, F. Dong, and C. Tan, "Landweber iterative image reconstruction method incorporated deep learning for electrical resistance tomography," *IEEE Trans. Instrum. Meas.*, vol. 70, pp. 1–11, 2021.
[217] R. Fu, Z. Wang, X. Zhang, D. Wang, X. Chen, and H. Wang, "A regularization-guided deep imaging method for electrical impedance tomography," *IEEE Sensors J.*, vol. 22, no. 9, pp. 8760–8771, May 2022.
[218] Z. Chen, J. Xiang, P.-O. Bagnaninchi, and Y. Yang, "MMV-net: A multiple measurement vector network for multifrequency electrical impedance tomography," *IEEE Trans. Neural Netw. Learn. Syst.*, vol. 34, no. 11, pp. 8938–8949, Nov. 2023.
[219] Z. Chen, Y. Yang, and P.-O. Bagnaninchi, "Hybrid learning-based cell aggregate imaging with miniature electrical impedance tomography," *IEEE Trans. Instrum. Meas.*, vol. 70, pp. 1–10, 2020.
[220] Z. Liu, P. Bagnaninchi, and Y. Yang, "Impedance-optical dual-modal cell culture imaging with learning-based information fusion," *IEEE Trans. Med. Imag.*, vol. 41, no. 4, pp. 983–996, Apr. 2022.
[221] J. Redmon and A. Farhadi, "YOLOv3: An incremental improvement," 2018, *arXiv:1804.02767*.
[222] K. He, X. Zhang, S. Ren, and J. Sun, "Deep residual learning for image recognition," in *Proc. IEEE Conf. Comput. Vis. Pattern Recognit.*, Jun. 2016, pp. 770–778.
[223] D. Bahdanau, K. Cho, and Y. Bengio, "Neural machine translation by jointly learning to align and translate," 2014, *arXiv:1409.0473*.
[224] S. Woo, J. Park, J.-Y. Lee, and I. S. Kweon, "CBAM: Convolutional block attention module," in *Proc. Eur. Conf. Comput. Vis. (ECCV)*, 2018, pp. 3–19.
[225] Z. Chen and Y. Yang, "Structure-aware dual-branch network for electrical impedance tomography in cell culture imaging," *IEEE Trans. Instrum. Meas.*, vol. 70, pp. 1–9, 2021.
[226] Z. Wu, S. Pan, F. Chen, G. Long, C. Zhang, and P. S. Yu, "A comprehensive survey on graph neural networks," *IEEE Trans. Neural Netw. Learn. Syst.*, vol. 32, no. 1, pp. 4–24, Jan. 2021.
[227] T. N. Kipf and M. Welling, "Semi-supervised classification with graph convolutional networks," 2016, *arXiv:1609.02907*.
[228] R. D. Cook, G. J. Saulnier, D. G. Gisser, J. C. Goble, J. C. Newell, and D. Isaacson, "ACT3: A high-speed, high-precision electrical impedance tomograph," *IEEE Trans. Biomed. Eng.*, vol. 41, no. 8, pp. 713–722, Aug. 1994.
[229] J. Kourunen, T. Savolainen, A. Lehikoinen, M. Vauhkonen, and L. M. Heikkinen, "Suitability of a PXI platform for an electrical impedance tomography system," *Meas. Sci. Technol.*, vol. 20, no. 1, Jan. 2009, Art. no. 015503.
[230] J. Zhang and L. Meng, "GResNet: Graph residual network for reviving deep GNNs from suspended animation," 2019, *arXiv:1909.05729*.
[231] F. Yu and V. Koltun, "Multi-scale context aggregation by dilated convolutions," 2015, *arXiv:1511.07122*.
[232] W. Herzberg, A. Hauptmann, and S. J. Hamilton, "Domain independent post-processing with graph U-nets: Applications to electrical impedance tomographic imaging," 2023, *arXiv:2305.05020*.
[233] R. Li, X. Yuan, M. Radfar, P. Marendy, W. Ni, T. J. O'Brien, and P. M. Casillas-Espinosa, "Graph signal processing, graph neural network and graph learning on biological data: A systematic review," *IEEE Rev. Biomed. Eng.*, vol. 16, pp. 109–135, 2023.
[234] Z. Liu, Z. Chen, Q. Wang, S. Zhang, and Y. Yang, "Regularized shallow image prior for electrical impedance tomography," 2023, *arXiv:2303.17735*.
[235] D. Liu, D. Smyl, D. Gu, and J. Du, "Shape-driven difference electrical impedance tomography," *IEEE Trans. Med. Imag.*, vol. 39, no. 12, pp. 3801–3812, Dec. 2020.
[236] Y. Xu, L. Yang, S. Lu, S. Qin, R. Tang, Z. Zhao, Y. Deng, and Z. Li, "Emerging trends and hot spots on electrical impedance tomography extrapulmonary applications," *Heliyon*, vol. 8, no. 12, Dec. 2022, Art. no. e12458.

CHRISTOS DIMAS (Member, IEEE) received the Diploma degree in electrical and computer engineering and the Ph.D. degree in electrical engineering and computer science from the National Technical University of Athens (NTUA), in 2016 and 2022, respectively. His Ph.D. thesis topic was ''Image Reconstruction Approaches and Circuit Modeling in Electrical Impedance Tomography,'' financed by the State Scholarships Foundation. He currently works in the industrial area of power electronics and as a research collaborator at NTUA. He has coauthored more than 35 journal and conference papers. His research interests include biomedical engineering, instrumentation, and analog integrated circuit design. He was a recipient of three best IEEE conference paper awards He regularly reviews for many IEEE TRANSACTIONS and conferences and serves on proposal review panels.

VASSILIS ALIMISIS (Student Member, IEEE) received the B.Sc. degree (Hons.) in physics and the M.Sc. degree in electronics and communications from the University of Patras, Greece, in 2017 and 2019, respectively. He is currently pursuing the Ph.D. degree with the National Technical University of Athens (NTUA), Greece, under the supervision of Prof. Paul P. Sotiriadis. His Ph.D. thesis and research are supported and financed by the E.L.K.E. NTUA Scholarships. He is a Teaching Assistant in undergraduate and graduate courses and supervises Diploma Thesis. He has authored and coauthored several conference papers and journal articles. His main research interests include analog microelectronic circuits, low-power electronics, biomedical circuits and systems, analog computing and integrated circuit architectures with applications in artificial intelligence, and machine learning. He was a recipient of the Best Paper Award from the IEEE International Conference on Microelectronics, in 2020, the Best Paper Award from the IEEE International Conference on Microelectronics, in 2021, the Best Paper Award (3rd Place) from the IEEE International Conference on Microelectronics, in 2023, the Best Paper Award from the IEEE Symposium on Integrated Circuits and Systems Design (SBCCI), in 2021, and the Best Paper Award from the 1st International Conference on Frontiers of Artificial Intelligence, Ethics, and Multidisciplinary Applications, in 2023. He regularly reviews for many IEEE TRANSACTIONS and conferences and serves on proposal review panels.

NIKOLAOS UZUNOGLU (Fellow, IEEE) was born in Constantinople, Turkey. He received the B.Sc. degree in electrical engineering from Istanbul Technical University, in 1973, and the M.Sc. and Ph.D. degrees from the University of Essex, U.K., in 1974 and 1976, respectively. He is currently an Emeritus Professor with the School of Electrical and Computer Engineering, National Technical University of Athens. Until 2018, he served as the Head of the Microwave and Fibre Optics Laboratory. His research interests include electromagnetic theory, microwaves, fiber optics, telecommunications, biological process simulations, in silico oncology, and biomedical engineering. He is a member of the Academy of Sciences of Armenia. In 1981, he received the International G. Marconi Award in Telecommunications.

PAUL P. SOTIRIADIS (Fellow, IEEE) received the Diploma degree in electrical and computer engineering from the National Technical University of Athens (NTUA), Greece, in 1994, the M.S. degree in electrical engineering from Stanford University, USA, in 1996, and the Ph.D. degree in electrical engineering and computer science from Massachusetts Institute of Technology, USA, in 2002.

In 2002, he joined as a Faculty Member of the Electrical and Computer Engineering Department, Johns Hopkins University. In 2012, he joined as a Faculty Member of the Electrical and Computer Engineering Department, NTUA, where he is currently a Professor in electrical and computer engineering and the Director of the Electronics Laboratory. He is also a Governing Board Member of the Hellenic (National) Space Center of Greece. He runs a team of 25 researchers. He has authored and coauthored more than 200 research publications, most of them in IEEE journals and conferences, holds one patent, and has contributed several chapters to technical books. His research interests include the design, optimization, and mathematical modeling of analog, mixed-signal and RF integrated and discrete circuits, sensor, and instrumentation architectures with an emphasis on biomedical instrumentation, advanced RF frequency synthesis, the application of machine learning and general AI in the operation, and the design of electronic circuits.

Prof. Sotiriadis received several awards, including the prestigious Guillemin–Cauer Award from the IEEE Circuits and Systems Society, in 2012, the Best Paper Award from the IEEE International Conference on Microelectronics (ICM), in 2021, the Best Paper Award from the IEEE Symposium on Integrated Circuits and Systems Design (SBCCI), in 2021, the Best Paper Award from the IEEE International Conference Microelectronics (ICM), in 2020, the Best Paper Award from the IEEE International Conference on Modern Circuits and Systems Technologies, in 2019, the Best Paper Award from the IEEE International Frequency Control Symposium, in 2012, the Best Paper Award from the IEEE International Symposium on Circuits and Systems, in 2007, and the IEEE Circuits and Systems Society (CASS) Outstanding Technical Committee Recognition, in 2022. He is an Associate Editor of IEEE SENSORS JOURNAL. He has served as an Associate Editor for the IEEE TRANSACTIONS ON CIRCUITS AND SYSTEMS—I: REGULAR PAPERS, from 2016 to 2020, and IEEE TRANSACTIONS ON CIRCUITS AND SYSTEMS—II: EXPRESS BRIEFS, from 2005 to 2010. He has been a member of technical committees of many conferences. He regularly reviews for many IEEE TRANSACTIONS and conferences and serves on proposal review panels.